



**NTNU – Trondheim**  
Norwegian University of  
Science and Technology

# 3D BEM Modelling of Tala Hydroelectric Powerhouse Complex, Bhutan

**Jónas Thor Ingólfsson**

Geology

Submission date: June 2014

Supervisor: Charlie Chunlin Li, IGB

Norwegian University of Science and Technology  
Department of Geology and Mineral Resources Engineering



---

# Summary

The utilization of the vast hydropower potential the Himalayas possess is growing in the Kingdom of Bhutan. Export of electricity to India is now the largest contributor to the economic well being of the country and an ambitious plan of harnessing over 10000 MW of hydropower by the year 2020 is being carried out. The large scale hydropower development in Bhutan started in the 1980s with construction of the Chhukha hydroelectric plant with capacity of 336 MW. The next milestone was the commission of the 1020 MW Tala hydroelectric plant in 2006 and 2007. The two plants are in close proximity to one another, near the Main Central Thrust of the Himalayan fault system. Here the powerhouse excavations of both power plants will be modelled and analysed, regarding stability and accuracy of rock mass quality parameters, with focus on Tala hydroelectric plant.

The powerhouse complex at Tala, which consists of two large caverns, has experienced failure both during construction and while operating. During the excavation of the crown portion of the powerhouse large rockfall occurred in the roof and during the rest of the excavation and after commission rockbolts have been failing. No records are of failure in the Chhukha powerhouse cavern after construction, but during excavation fatal rockfall occurred. The Main Central Thrust provides high horizontal stresses, especially at Tala, in overall poor rock conditions.

The initial modelling is done in Examine<sup>3D</sup>, a 3D BEM elastic modelling software. The model of Tala powerhouse complex is then compared to models from Examine<sup>2D</sup> and Phase<sup>2</sup>, elastic 2D BEM and plastic 2D FEM models respectively. The powerhouse of Chhukha is also modelled in Examine<sup>3D</sup>, and circumstances compared to Tala. Additionally, the model of Tala is matched with actual measured values of convergence, but maximum convergence measured in the powerhouse cavern was 0,374 m. That was done by iterating the Young's modulus in the Phase<sup>2</sup> until a value that represented the actual convergence was found. Elastic models with same Young's modulus value were then created in the other codes and compared.

The challenges of underground excavation in the tectonically active Himalayas is portrayed here, as the high uncertainty in estimates of quality of the rock mass encountered can lead to flawed design. The methodology used here is reviewed and proven to be beneficial as visualization of the problem is far greater in the 3D space.

---

---

---

# Preface

This master thesis titled "3D BEM Modelling of Tala Powerhouse Complex, Bhutan" is my final work on the road to a masters degree in Geology with specialization in Environmental and Geotechnology from the Norwegian University of Science and Technology. It mainly involves 3D modelling of two underground powerhouses in Bhutan, Himalaya, as well as comparison with two types of 2D modelling methods. Theoretical background is provided as well as background of the two hydroelectric projects of Tala and Chhukha. The work utilizes knowledge gathered throughout my studies during the two year masters programme.

The work presented here is my own and the sources used for the background and theory behind the work is duly acknowledged.

The thesis work was done in the winter of 2013 - 2014, from September 15<sup>th</sup> - June 1<sup>st</sup>, under supervision from Professor Charlie C. Li, to which I owe my gratitude for his guidance on the subject. I would also like to extend my thanks to my friends and fellow students, that in any way lent a helping hand in the working process.

---

# Contents

<b>Summary</b>	<b>i</b>
<b>Preface</b>	<b>iii</b>
<b>Table of Contents</b>	<b>v</b>
<b>List of Tables</b>	<b>vii</b>
<b>List of Figures</b>	<b>ix</b>
<b>1 Introduction</b>	<b>1</b>
1.1 In General . . . . .	1
1.2 Background of study . . . . .	2
1.3 Scope and limitations . . . . .	3
<b>2 Theory</b>	<b>5</b>
2.1 Numerical Modelling of Underground Excavations . . . . .	5
2.1.1 Two- and three- dimensional approaches . . . . .	6
2.1.2 Boundary Element Method . . . . .	6
2.1.3 Finite Element method . . . . .	7
2.1.4 Codes Used for Analyses . . . . .	8
2.2 Rock Mass Classification Systems . . . . .	9
2.2.1 Q system . . . . .	9
2.2.2 Rock Mass Rating, RMR . . . . .	12
2.2.3 GSI . . . . .	13
2.3 Rock Mass Quality . . . . .	13
2.3.1 Failure Criteria . . . . .	13
2.3.2 Rock Mass Deformation . . . . .	16

---

<b>3</b>	<b>Problem Description</b>	<b>19</b>
3.1	Geology of the Bhutan Himalaya . . . . .	19
3.1.1	Challenges of tunnelling in the Himalayas . . . . .	20
3.2	The Tala Hydropower Project . . . . .	23
3.2.1	In General . . . . .	23
3.2.2	Local Geology . . . . .	25
3.2.3	The Construction Phase . . . . .	29
3.3	The Chhukha Hydropower Project . . . . .	35
3.3.1	In General . . . . .	35
3.3.2	Geology . . . . .	36
3.3.3	The Construction Phase . . . . .	38
3.4	Comparison between Tala and Chhukha . . . . .	39
<b>4</b>	<b>Numerical Analyses</b>	<b>41</b>
4.1	In General . . . . .	41
4.2	Input parameters . . . . .	41
4.3	Analyses and results . . . . .	43
4.3.1	Examine <sup>3D</sup> , literature values . . . . .	44
4.3.2	Examine <sup>2D</sup> , literature values . . . . .	55
4.3.3	Phase <sup>2</sup> , literature values . . . . .	57
4.4	Back - Calculation . . . . .	60
4.4.1	Examine <sup>3D</sup> , back-calculation . . . . .	61
4.4.2	Examine <sup>2D</sup> , back-calculation . . . . .	64
4.4.3	Phase <sup>2</sup> , back-calculation . . . . .	65
4.5	Examine <sup>3D</sup> , Chhukha . . . . .	66
<b>5</b>	<b>Discussion</b>	<b>79</b>
5.1	Tala powerhouse complex: Literature input parameters . . . . .	79
5.1.1	Examine <sup>3D</sup> . . . . .	79
5.1.2	Examine <sup>2D</sup> . . . . .	80
5.1.3	Phase <sup>2</sup> . . . . .	80
5.2	Tala Powerhouse Complex: Back - Calculation . . . . .	81
5.3	Chhukha Powerhouse cavern . . . . .	82
5.4	Summary of Stability Analyses . . . . .	82
<b>6</b>	<b>Conclusion and Recommendations</b>	<b>85</b>
	<b>Bibliography</b>	<b>87</b>
	References . . . . .	87
	<b>Appendices</b>	<b>91</b>

---



# List of Tables

2.1	The RMR classification system (Bieniawski, 1989) . . . . .	12
3.1	The main features of The Tala Hydroelectric Project . . . . .	25
3.2	Measured joints around the Powerhouse complex (Singh, Chowdhry, Sharma, Goyal, & Khazanchi, 2002) . . . . .	26
3.3	Estimate of rock mass properties along the powerhouse cavern. Macine hall is at RD 39 m - RD 245 m (Chowdhry, 2007) . . . . .	27
3.4	Primary rock mass parameters obtained in pre-construction exploration drift and literature. (Chopra & Gupta, 2003) . . . . .	27
3.5	Average rock mass properties of Phyllitic quartzite (Chopra & Gupta, 2003). LR = Linear Regression, SR, NLR = Simplex Reflection, Non-Linear Regression . . . . .	28
3.6	Rock mass parameters around the powerhouse complex (Chopra & Gupta, 2003) . . . . .	28
3.7	Joint parameters around the powerhouse complex (Chopra & Gupta, 2003)	28
3.8	Rock bolt failure in the machine hall at Tala hydroelectric plant from May 2003 - June 2011. Adapted from (Naik, Sudhakar, Nair, & Nawani, 2011). MH = Machine Hall, US = Upstream, DS = Downstream, GE = Gable End Wall . . . . .	30
3.9	Properties of Dywidag rock bolts used in the support system,as given from the manufacturer (Singh et al., 2002) . . . . .	33
3.10	Results from pull out tests on the Tor steel rock bolts (Singh et al., 2002) .	33
3.11	Results from pull out tests on the Dywidag rock bolts (Singh et al., 2002)	34
3.12	The main features of the Chhukha Hydroelectric Project . . . . .	35
3.13	The recorded joint sets in rock mass surrounding Chhukha machine hall (Char, Menon, & Sood, 1988) . . . . .	36
3.14	Rock mass properties in host rock of Chhukha powerhouse cavern (Char et al., 1988) . . . . .	38
3.15	In situ stress around Chhukha powerhouse cavern (Char et al., 1988) . . .	38

---

4.1	Input parameters for numerical analyses, obtained from literature. The Hoek-Brown constants were calculated using Rocscience's RocData software. . . . .	42
4.2	The input parameters for the in-situ stress field at Tala and Chhukha. The orientation is controlled by direction counted clockwise in degrees from north in the model coordinate system and dip in degrees from horizontal. .	42
4.3	Modelling parameters used in Examine <sup>3D</sup> . . . . .	42
4.4	Modelling parameters used in Phase <sup>2</sup> and Examine <sup>2D</sup> . . . . .	43
5.1	Comparison between different modelling methods. Four points were measured precisely in all three modelling software and values obtained for the principal stresses, depth of failures zone defined by strength factor < 1 (FZ depth) and total displacement. The four points are the mid section of the upstream wall of the powerhouse cavern, the mid section of the transformer hall downstream cavern and the middle of the roofs of both caverns	84
A1	Guidelines for assigning values for the Q parameters. From Hoek, Kaiser, & Bawden, 1995, after Barton, Lien, & Lunde, 1974 . . . . .	92
A2	Guidelines for assigning values for the Q parameters(continued). From Hoek et al., 1995, after Barton et al., 1974 . . . . .	93
A3	Guidelines for assigning values for the Q parameters(continued). From Hoek et al., 1995, after Barton et al., 1974 . . . . .	94
A4	Guidelines for assigning values for the RMR parameters. From Hoek et al., 1995, after Bieniawski, 1989 . . . . .	95
A5	Value of the $m_i$ constant for various rock types (Hoek & Brown, 1997) . .	96
A6	Guidelines for estimation of D factor(Hoek, Carranza-Torres, & Corkum, 2002) . . . . .	97

# List of Figures

1.1	Location of Bhutan on the world map ( <i>Maps of World</i> , 2013) . . . . .	2
1.2	Bhutan's plan for harnessing over 10.000 MW from the 4 river system (e-Kuensel, 28 <sup>th</sup> Jan, 2012, as cited by Dorji, 2012) . . . . .	3
2.1	Numerical methods in rock mechanics (Gnilsen, 1989). . . . .	6
2.2	The Q- system graph (Barton et al., 1974) . . . . .	11
2.3	The GSI chart (Marinos, Marinos, & Hoek, 2005) . . . . .	14
2.4	The Mohr-Coulomb failure envelope represented on a Mohr diagram (Labuz & Zang, 2012) . . . . .	15
2.5	The Hoek-Brown failure envelope showing the relationship between major and minor principal stresses and the shear strength (Hoek & Brown, 1980)	16
2.6	Typical stress versus deformation curve form deformability test on rock mass from the Tala project (Palmström & Singh, 2001) . . . . .	17
2.7	Post failure characteristics of rock based on quality (Hoek & Brown, 1997)	18
3.1	Large scale geological map of Bhutan, showing the main units in the tectonostratigraphy (Grujic, Hollister, & Parrish, 2002) . . . . .	20
3.2	Geological map of the Wang Chhu river basin and the Paro formation window. The location of the two powerplants is just south of the town of Chhukha (Tobgay, Long, McQuarrie, Ducea, & Gehrels, 2010) . . . . .	21
3.3	The pre-construction investigation system recommended by Panthi and Nilsen for work in the Himalayas (Panthi & Nilsen, 2007) . . . . .	22
3.4	The layout of the powerhouse complex of Tala hydroelectric plant (Report on quality control, 2006) . . . . .	23
3.5	The profile of the powerhouse complex of Tala Hydroelectric plant (Report on quality control, 2006) . . . . .	24
3.6	Cross section through the local geology (Goyal & Khazanchi, 2003) . . .	29
3.7	Load vs. displacement comparison between pull out tests of 32mm dia / 12 m long Tor steel rock bolts and Dywidag rock bolts (Singh et al., 2002)	34

---

3.8	Layout of the Chhukha hydroelectric infrastructure (Madhavan, Parasuraman, & Sood, 1987) . . . . .	36
3.9	Cross section of the Chhukha machine hall with the dominant joint sets (Char et al., 1988) . . . . .	37
3.10	The profile of the Chhukha powerhouse cavern, showing layout of rock support and elevation markers (Char et al., 1988) . . . . .	39
4.1	The cutting planes in the model of Tala powerhouse complex. RD 103 m at the middle of the complex lengthwise, RD 44,5 m equal to the height of the machine hall RD 10 m where the end effect can be observed in both caverns. EL 515 m is in the middle of the machine hall height-wise . . . .	43
4.2	RD 103 m at Tala powerhouse complex, depicting contours of equal $\sigma_1$ , using literature input values . . . . .	44
4.3	RD 44,5 m at Tala powerhouse complex, depicting contours of equal $\sigma_1$ , using literature input values . . . . .	44
4.4	RD 10 m at Tala powerhouse complex, depicting contours of equal $\sigma_1$ , using literature input values . . . . .	45
4.5	EL 515 m at Tala powerhouse complex, depicting contours of equal $\sigma_1$ , using literature input values . . . . .	45
4.6	RD 103 m at Tala powerhouse complex, depicting contours of equal $\sigma_3$ , using literature input values . . . . .	46
4.7	RD 44,5 m at Tala powerhouse complex, depicting contours of equal $\sigma_3$ , using literature input values . . . . .	46
4.8	RD 10 m at Tala powerhouse complex, depicting contours of equal $\sigma_3$ , using literature input values . . . . .	47
4.9	EL 515 m at Tala powerhouse complex, depicting contours of equal $\sigma_3$ , using literature input values . . . . .	47
4.10	Perspective of the Tala powerhouse complex, depicting isosurface at $\sigma_3 = 0$ , using literature input values . . . . .	48
4.11	Perspective of the Tala powerhouse complex, depicting isosurface at $\sigma_3 = 0$ , using literature input values . . . . .	48
4.12	RD 103 m at Tala powerhouse complex, depicting contours of equal strength factor, using literature input values . . . . .	49
4.13	RD 44,5 m at Tala powerhouse complex, depicting contours of equal strength factor, using literature input values . . . . .	49
4.14	RD 10 m at Tala powerhouse complex, depicting contours of equal strength factor, using literature input values . . . . .	50
4.15	EL 515 m at Tala powerhouse complex, depicting contours of equal strength factor, using literature input values . . . . .	50
4.16	Perspective of the Tala powerhouse complex, depicting isosurface at strength factor = 1, using literature input values . . . . .	51
4.17	Perspective of the Tala powerhouse complex, depicting isosurface at strength factor = 1, using literature input values . . . . .	51
4.18	RD 103 m at Tala powerhouse complex, depicting contours of equal total displacement, using literature input values . . . . .	52

---

---

4.19	RD 44,5 m at Tala powerhouse complex, depicting contours of equal total displacement, using literature input values . . . . .	52
4.20	RD 10 m at Tala powerhouse complex, depicting contours of equal total displacement, using literature input values . . . . .	53
4.21	EL 515 m at Tala powerhouse complex, depicting contours of equal total displacement, using literature input values . . . . .	53
4.22	Perspective of the Tala powerhouse complex depicting the total displacement as it appears on the surface of excavation, using literature input values	54
4.23	Perspective of the Tala powerhouse complex depicting the total displacement as it appears on the surface of excavation, using literature input values	54
4.24	Examine <sup>2D</sup> model of the Tala powerhouse complex, depicting contours of equal $\sigma_1$ , using literature input values . . . . .	55
4.25	Examine <sup>2D</sup> model of the Tala powerhouse complex, depicting contours of equal $\sigma_3$ , using literature input values . . . . .	55
4.26	Examine <sup>2D</sup> model of the Tala powerhouse complex, depicting contours of equal strength factor, using literature input values . . . . .	56
4.27	Examine <sup>2D</sup> model of the Tala powerhouse complex, depicting contours of equal total displacement, using literature input values . . . . .	56
4.28	Phase <sup>2</sup> model of the Tala powerhouse complex, depicting contours of equal $\sigma_1$ , using literature input values . . . . .	57
4.29	Phase <sup>2</sup> model of the Tala powerhouse complex, depicting contours of equal $\sigma_3$ , using literature input values . . . . .	57
4.30	Phase <sup>2</sup> model of the Tala powerhouse complex, depicting contours of equal strength factor, using literature input values . . . . .	58
4.31	Phase <sup>2</sup> model of the Tala powerhouse complex, depicting contours of equal total displacement, using literature input values . . . . .	58
4.32	Phase <sup>2</sup> model of the Tala powerhouse complex, depicting yielded elements, using literature input values . . . . .	59
4.33	Measured value of convergence in the Phase <sup>2</sup> model at EL 515/RD 103 of the Tala machine hall, plotted against varying values of Young's modulus. The red mark indicates the convergence in the model with the literature value of Young's modulus at 7950 MPa and the black triangle is the measured value of maximum convergence of 0,374 m . . . . .	60
4.34	RD 103 m at Tala powerhouse complex, depicting contours of equal total displacement, using Young's modulus of 4250 MPa . . . . .	61
4.35	RD 44,5 m at Tala powerhouse complex, depicting contours of equal total displacement, using Young's modulus of 4250 MPa . . . . .	61
4.36	RD 10 m at Tala powerhouse complex, depicting contours of equal total displacement, using Young's modulus of 4250 MPa . . . . .	62
4.37	EL 515 m at Tala powerhouse complex, depicting contours of equal total displacement, using Young's modulus of 4250 MPa . . . . .	62
4.38	Perspective of the Tala powerhouse complex depicting the total displacement as it appears on the surface of excavation, using Young's modulus of 4250 MPa . . . . .	63

---

---

4.39	Perspective of the Tala powerhouse complex depicting the total displacement as it appears on the surface of excavation, using Young's modulus of 4250 MPa . . . . .	63
4.40	Examine <sup>2D</sup> model of the Tala powerhouse complex, depicting contours of equal total displacement, using Young's modulus of 4250 MPa . . . . .	64
4.41	Phase <sup>2</sup> model of the Tala powerhouse complex, depicting contours of equal total displacement, using Young's modulus of 4250 MPa . . . . .	65
4.42	Perspective of the cutting planes in the 3D model of Chhukha . . . . .	66
4.43	RD 70,6 m at Chhukha powerhouse cavern, depicting contours of equal $\sigma_1$	67
4.44	RD 37,5 m at Chhukha powerhouse cavern, depicting contours of equal $\sigma_1$	67
4.45	RD 5 m at Chhukha powerhouse cavern, depicting contours of equal $\sigma_1$ .	68
4.46	EL 1385 m at Chhukha powerhouse cavern, depicting contours of equal $\sigma_1$	68
4.47	RD 70,6 m at Chhukha powerhouse cavern, depicting contours of equal $\sigma_3$	69
4.48	RD 37,5 m at Chhukha powerhouse cavern, depicting contours of equal $\sigma_3$	69
4.49	RD 5 m at Chhukha powerhouse cavern, depicting contours of equal $\sigma_3$ .	70
4.50	EL 1385 m at Chhukha powerhouse cavern, depicting contours of equal $\sigma_3$	70
4.51	Perspective of the Tala powerhouse complex, depicting isosurface at $\sigma_3 = 0$	71
4.52	Perspective of the Tala powerhouse complex, depicting isosurface at $\sigma_3 = 0$	71
4.53	RD 70,6 m at Chhukha powerhouse cavern, depicting contours of equal strength factor . . . . .	72
4.54	RD 37,5 m at Chhukha powerhouse cavern, depicting contours of equal strength factor . . . . .	72
4.55	RD 5 m at Chhukha powerhouse cavern, depicting contours of equal strength factor . . . . .	73
4.56	EL 1385 m at Chhukha powerhouse cavern, depicting contours of equal strength factor . . . . .	73
4.57	Perspective of the Chhukha powerhouse cavern, depicting isosurface at strength factor = 1 . . . . .	74
4.58	Perspective of the Chhukha powerhouse cavern, depicting isosurface at strength factor = 1 . . . . .	74
4.59	RD 70,6 m at Chhukha powerhouse cavern, depicting contours of equal total displacement . . . . .	75
4.60	RD 37,5 m at Chhukha powerhouse cavern, depicting contours of equal total displacement . . . . .	75
4.61	RD 5 m at Chhukha powerhouse cavern, depicting contours of equal total displacement . . . . .	76
4.62	EL 1385 m at Chhukha powerhouse cavern, depicting contours of equal total displacement . . . . .	76
4.63	Perspective of the Chhukha powerhouse cavern, depicting the total displacement as it appears on the surface of excavation . . . . .	77
4.64	Perspective of the Chhukha powerhouse cavern, depicting the total displacement as it appears on the surface of excavation . . . . .	77
A1	RD 103 m at Tala powerhouse complex, depicting contours of equal $\sigma_1$ , using Young's modulus of 4250 MPa . . . . .	99

---

---

A2	RD 44,5 m at Tala powerhouse complex, depicting contours of equal $\sigma_1$ , using Young's modulus of 4250 MPa . . . . .	99
A3	RD 10 m at Tala powerhouse complex, depicting contours of equal $\sigma_1$ , using Young's modulus of 4250 MPa . . . . .	100
A4	EL 515 m at Tala powerhouse complex, depicting contours of equal $\sigma_1$ , using Young's modulus of 4250 MPa . . . . .	100
A5	RD 103 m at Tala powerhouse complex, depicting contours of equal $\sigma_3$ , using Young's modulus of 4250 MPa . . . . .	101
A6	RD 44,5 m at Tala powerhouse complex, depicting contours of equal $\sigma_3$ , using Young's modulus of 4250 MPa . . . . .	101
A7	RD 10 m at Tala powerhouse complex, depicting contours of equal $\sigma_3$ , using Young's modulus of 4250 MPa . . . . .	102
A8	EL 515 m at Tala powerhouse complex, depicting contours of equal $\sigma_3$ , using Young's modulus of 4250 MPa . . . . .	102
A9	Perspective of the Tala powerhouse complex, depicting isosurface at $\sigma_3 = 0$ , using Young's modulus of 4250 MPa . . . . .	103
A10	Perspective of the Tala powerhouse complex, depicting isosurface at $\sigma_3 = 0$ , using Young's modulus of 4250 MPa . . . . .	103
A11	RD 103 m at Tala powerhouse complex, depicting contours of equal strength factor, using Young's modulus of 4250 MPa . . . . .	104
A12	RD 44,5 m at Tala powerhouse complex, depicting contours of equal strength factor, using Young's modulus of 4250 MPa . . . . .	104
A13	RD 10 m at Tala powerhouse complex, depicting contours of equal strength factor, using Young's modulus of 4250 MPa . . . . .	105
A14	EL 515 m at Tala powerhouse complex, depicting contours of equal strength factor, using Young's modulus of 4250 MPa . . . . .	105
A15	Perspective of the Tala powerhouse complex, depicting isosurface at strength factor = 1, using Young's modulus of 4250 MPa . . . . .	106
A16	Perspective of the Tala powerhouse complex, depicting isosurface at strength factor = 1, using Young's modulus of 4250 MPa . . . . .	106
A17	Examine <sup>2D</sup> model of the Tala powerhouse complex, depicting contours of equal $\sigma_1$ , using Young's modulus of 4250 MPa . . . . .	107
A18	Examine <sup>2D</sup> model of the Tala powerhouse complex, depicting contours of equal $\sigma_3$ , using Young's modulus of 4250 MPa . . . . .	107
A19	Examine <sup>2D</sup> model of the Tala powerhouse complex, depicting contours of equal strength factor, using Young's modulus of 4250 MPa . . . . .	108
A20	Phase <sup>2</sup> model of the Tala powerhouse complex, depicting contours of equal $\sigma_1$ , using Young's modulus of 4250 MPa . . . . .	108
A21	Phase <sup>2</sup> model of the Tala powerhouse complex, depicting contours of equal $\sigma_3$ , using Young's modulus of 4250 MPa . . . . .	109
A22	Phase <sup>2</sup> model of the Tala powerhouse complex, depicting contours of equal strength factor, using Young's modulus of 4250 MPa . . . . .	109
A23	Phase <sup>2</sup> model of the Tala powerhouse complex, depicting yielded elements, using Young's modulus of 4250 MPa . . . . .	110

---

---



# Introduction

## 1.1 In General

The Kingdom of Bhutan lies in the southern slopes of the eastern Himalayas, landlocked between China in the north and India in the south (figure 1.1). The kingdom covers about 38,398 km<sup>2</sup> and its topography is characterized by steep and high mountains cut through by swift rivers. The northern part of the country is dominated by the Himalayan mountains, with peaks reaching over 7000 m above mean sea level. The land lowers to the south, until it reaches the Indian plains near the south borders. This topography, alongside with glacial meltwater from the northern part and relatively high precipitation especially during the monsoon season, creates large potential for harnessing power from the river systems. There are mainly four river systems, flowing from the north to south in Bhutan; the Drangme Chhu, the Puna Tsang Chhu (Sankosh Chhu), the Amo Chhu (Torsa Chhu) and the Wang Chhu, of which the Wang Chhu system feeds the two hydropower plants focused on here.

Electricity was only first introduced in Bhutan in the year of 1966, in Phuentsholing, a town on the south–west border of India. That was with the installation of a 25 kW diesel generator. One year later, the first hydropower plant, with capacity of 350 kW was commissioned in the capital city of Thimphu. In the following years the electrification of the country continued by import of power from India to the southernmost regions. By that time, the potential of hydropower had been recognized and effort was put into developing plans to harness it. The first milestone in the development was the commission of the 336 MW Chhukha hydroelectric plant in the year 1988, but construction had started 1978. Many smaller hydroelectric plants were commissioned in that time and the following years. The next milestone was the commission of the 1020 MW Tala hydroelectric plant in 2006 -2007.

Now, about 97% of electricity generated in Bhutan is hydroelectric. The total energy production of greatly exceeds its own needs during the summertime when precipitation is

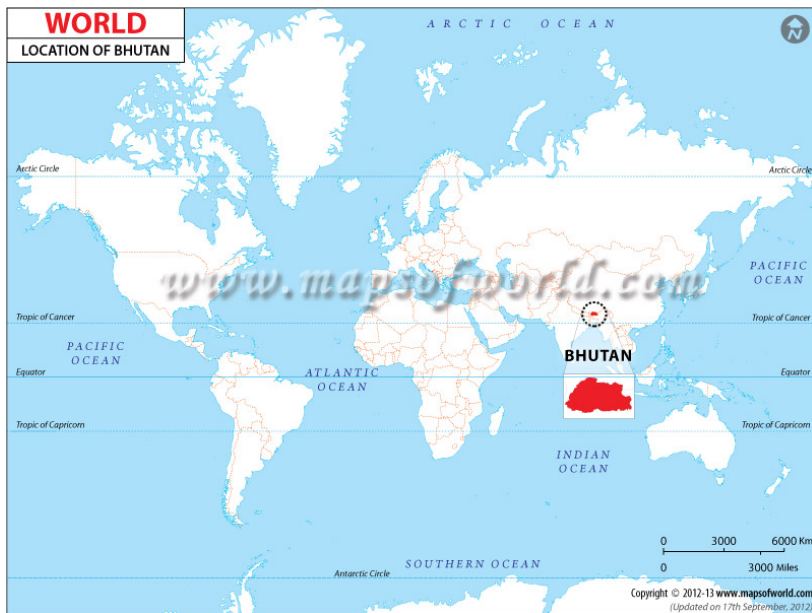


**Figure 1.1:** Location of Bhutan on the world map (*Maps of World*, 2013)

at maximum, and the surplus energy is exported, mainly to India. The energy exported makes up for about 80% of all power generated (ADB, 2008). In the years 2008-2009 the power export was 45% of the total export and over 40% of the total national revenue (ADB, 2010).

Today Bhutan is following its ambitious plans of harnessing over 10000 MW of hydro-electricity for export. That is mainly through 10 projects, ranging from capacity of 180 – up to 3300 MW. The projects are at various stages, all from being studied for feasibility to being under construction. The planned projects can be seen in figure 1.2, as well as the major already-commissioned hydropower plants.

## 1.2 Background of study

As the development of hydropower in Bhutan plays this significant role in the country's economical well-being, the financial part of projects related to it must be considered. The steep topography of the area is limiting the choice of building sites for the infrastructure, so underground excavation becomes a promising choice, along with other benefits like security. It is generally accepted that two of the largest factors in designing an underground excavation are time and cost, which then again go hand in hand; increased time of excavation is costly, as well as it delays the eventual return of the investment of construction. Thorough pre-construction investigation and research of the area as well as continuous measurements during and after construction are beneficial for the project as whole, and

detailed case studies of completed projects can benefit future projects.

Due to the ongoing orogeny of the Himalaya region, where the Indian tectonic plate is colliding with the Eurasian plate, challenges in underground excavations can be substantial. The underground powerhouse complex at Tala Hydroelectric plant has been faced with these challenges, surfacing in crown failure during construction, extensive rock support and failure in rock support to name a few. It is situated in close proximity to one of the main fault in the Himalayan frontal fault system, the Main Central Thrust (MCT). Although not having been active for the last 17 million years, signs have been noticed in Nepal that activity might be on the rise. Analysis of the stability of the excavation, and the factors affecting it might prove beneficial for future projects in the similar conditions, as well as evaluation and comparison between multiple numerical analytical methods provided by the software used in this study.

### 1.3 Scope and limitations

As the excavations this paper refers to are both operational, the main scope of the report is to obtain understanding of the accuracy of 3D elastic BEM modelling. The 3D model serves as good medium to visualize the induced stress field around the caverns and esti-

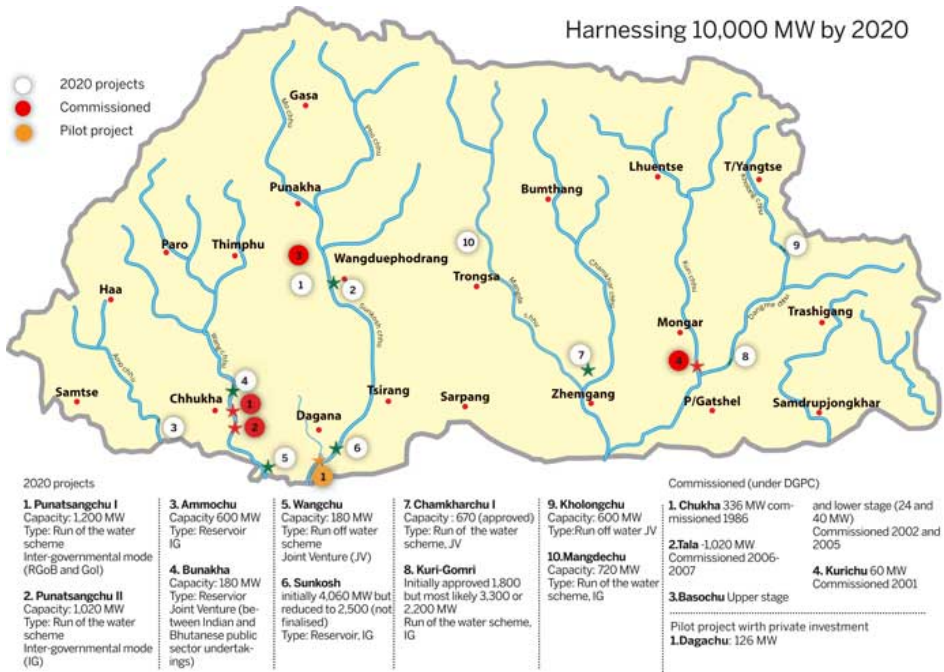


**Figure 1.2:** Bhutan’s plan for harnessing over 10,000 MW from the 4 river system (e-Kuensel, 28<sup>th</sup> Jan, 2012, as cited by Dorji, 2012)

---

mate where issues with stability are likely to form and in which way. Plans have been made in similar conditions for projects of the same or larger degree than the Tala project, and some are under way today. This method of analysis might prove beneficial in the design stage of large scale excavations.

The study is based on literature research and data from the construction phase and post-construction measurements, as well as the modelling work. Data from the literatures is reviewed and a model constructed and analysed based on that data.

The powerhouse caverns of Tala and Chhuhka will be modelled in 3D and comparisons made to 2D plastic FEM model and 2D BEM model versions of the Tala complex.

Back-calculation will be made for the Tala caverns, where a model will be produced that resembles the actual measured values for depth of failure zone and convergence of the machine hall. The input parameters of deformation modulus needed to get the end result that resembles the reality, will be reviewed and compared to originally measured values.

The limitations of the study are listed below:

- Simplifications of natural circumstances. The host material in the BEM models is assumed elastic, homogeneous and isotropic, where as in reality it is more complex.
- No actual field research was done, but information obtained from earlier research, data from construction phase and post construction.
- Progressive failure can not be portrayed using the BEM models used here.
- Data on the Chhukha powerhouse was limited. That goes for instrumentation data during and after excavation, detailed in-situ stress field and some rock mechanical material factors.

# Theory

## 2.1 Numerical Modelling of Underground Excavations

The numerical methods that can be used for analyses of the stress environment and deformation, and the choice of method each time is determined by the objects being viewed. The most common methods can be classified as follows:

- Continuum method, which is the finite difference method, the finite element method and the boundary element method (FDM, FEM and BEM, respectively).
- Discrete methods, which are the discrete element method and the discrete fracture network (DEM and DFN).
- Hybrid method of continuum and discrete methods combined

One method does not have specific advantages over the other, so while making a choice of which method should be used many problem-specific factors need to be considered, as well as the geometry and the rock mass properties. In moderately fractured rock the discrete method serves better than the continuum method, as well as where large-scale deformation can be anticipated. The continuum method is better applicable where the rock mass is more intact, where the fracture system is less complex. The hybrid models, where the discrete and the continuum methods are combined, some weaknesses of both methods can be eliminated (Jing & Hudson, 2002). As the practise of numerical modelling is most often associated with dealing with uncertainties, assumptions and quantifying non-quantifiable objects, the complexity of the model increases as more components of input data containing uncertainties sums up. As Hammah and Curran (2009) stated in their conference paper title, "*It is better to be approximately right than precisely wrong...*". The simple methods often provide more reliable results than the complex ones, as the number of factors contributing to the error has been reduced.

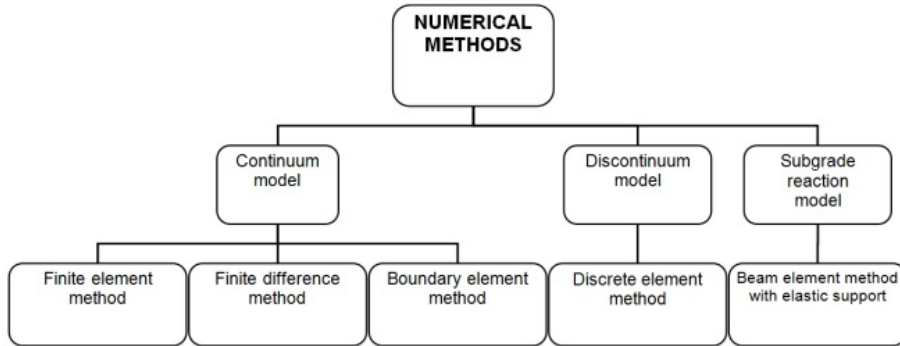


**Figure 2.1:** Numerical methods in rock mechanics (Gnilsen, 1989).

### 2.1.1 Two- and three- dimensional approaches

When analysing the stress and stability of long tunnels or shafts, a two-dimensional approach can be suitable, where the length greatly exceeds the cross-section of the profile. The stress and displacements can be modelled in a plane crossing the excavation, far enough away from the ends of it so they do not affect the stresses in the plane, and necessary observations can be made. Where the dimensions are different and the ends of the observed object have greater effect, for example in shorter cavern or a pillar, a three-dimensional model needs to be employed. Such models give a good estimate of the stress concentrations and the effect of the geometry of the object. Two- and three-dimensional models often go hand in hand, as simpler three-dimensional models are mostly BEM based. In that case, a preliminary three-dimensional model can be constructed and be followed by a two-dimensional finite- or discrete element analysis where further investigation is needed (Hoek et al., 1995). In addition, the visual effect of the 3D approach can often help in understanding the behaviour of the rock mass in more comprehensive way, thereby better indicating elements of the project at hand that might require more attention.

### 2.1.2 Boundary Element Method

By using differential equations and boundary conditions, almost all physical elements can be represented. When structural problems arise, like the behaviour of rock mass when the stress field is altered by excavating opening in the mass, analytical solutions that both fulfil the differential equations demands and the boundary conditions are scarce. That is when approximate solutions need to be applied. It can be done in two ways, by relying on only one of the two components, differential equations or the boundary conditions, in order to minimize the errors in the other. The FEM focuses on the boundary conditions, discretizing the rock mass surrounding the opening into smaller elements. On the other hand, BEM only takes the differential equations into account, thus minimizing the error of the boundary conditions. Here, the rock mass is not discretized, but the boundary elements are divided into finite elements that the values of interest can be interpolated over.

---

This method greatly reduces the number of unknowns, as with focusing on the surface, rather than the volumetric rock mass, we have excluded one dimension from the domain and the unknowns are only in the boundary. That also enables the solving of infinite problems (Beer, Smith, & Dunser, 2008). The BEM is especially suitable where the rock mass can be considered elastic and intact or with continuous planes of weakness. The method is based on estimation of traction and displacement in the surface. The traction and the displacement relationship is based on Betti's reciprocal theorem, where traction and displacement in point P can be expressed in equation 2.1:

$$c(P)u(P) = \int_s t(P, Q)u(Q)ds + \int_s U(P, Q)t(Q)ds \quad (2.1)$$

Here Q is a point on surface S,  $u(Q)$  is the displacement vector at Q and  $t(Q)$  the traction vector.  $T(P, Q)$  is a matrix of fundamental solutions for the tractions and  $U(P, Q)$  for the displacements.  $c(P)$  is a matrix dependant on the tangent to the surface at point P (Beer, 2000). As for shortcomings of BEM, Beer (2000) listed three main disadvantages:

- Modelling of non-linear phenomena like creep, plasticity and swelling is problematic.
- Different stages of construction cannot be represented as easily as when using FEM.
- Rock support cannot be modelled as elements.

On the contrary to the problems of modelling non-linear elements, more recent publications indicate that problems with material with heterogeneous properties can be solved, using special methods and repeated solution of linear problems, almost as easily with BEM as it would be using FEM (Beer et al., 2008).

### 2.1.3 Finite Element method

The FEM is one of the most used methods for underground excavation stress and stability analyses. As mentioned earlier, the finite element method, or FEM, is continuous method that only focuses on satisfying the boundary conditions. In this method the domain boundaries need to be defined, and the size of it needs to be large enough so that the modelled object will not be affected by these outer boundaries. The whole domain is then discretised into finite elements, connected via nodes. The properties of each element can be defined, like deformation characteristics, so the FEM's capability to deal with heterogeneity is better than the BEM's. The effect of the changes in the rock mass is interpreted in the nodes of the elements, and continues through the elements and is again interpreted in the next element. By cumulating all the data from each node, the forces and deformation for the whole domain can be gathered implicitly in complex set of equations. As the discretization is more intensive in FEM than it is in BEM, the computation is more demanding and time consuming, although it is based on the grade of discretization, and thereby accuracy. In the discretization, the element density is increased where the stresses are highest, that is near the excavation boundary, which is as well most often the main place of interest (Myrvang, 2001).

---

## 2.1.4 Codes Used for Analyses

Three software codes were used for the analyses for this work, all of which were developed by RocScience. The codes are Examine<sup>3D</sup>, Examine<sup>2D</sup> and Phase<sup>2</sup>, 3D BEM, 2D BEM and 2D FEM respectively.

### Examine<sup>3D</sup>

The Examine 3D code was used to construct 3D models of the powerhouse complex of Tala and the machine hall of Chhukha. The program utilizes a simple user interface to construct a model, like for this instance of underground powerhouse complex. The code is based on the BEM, thus simplifying the problem quite drastically by considering the rock mass continuous and fully elastic, so that must be recognized in the analytical work. Due to the same reason progressive failure can not be estimated or emulated.

For the larger and more complex work, like the powerhouse complex at Tala presented in this thesis, the program seemed to meet its limits, as the number of elements in the model exceeded 35000, the program came to halt or crashed, regardless of available computational resources. The end product from the stress analysis environment of the program used are:

- Contour plots of any section of the model, showing various stress components and trajectories, strength factor, displacement.
- Isosurface, revealing surfaces in the rock mass where points have the same specified value of the components mentioned above.
- Surface contours, that show the same components as they appear at the surface of the excavation.

### Examine<sup>2D</sup>

The Examine<sup>2D</sup> is an easy running two dimensional BEM modelling software. For simple profiles of excavations like presented in this thesis, computation of the model is instantaneous, whereas in the other program used it takes from several minutes up to about an hour to compute the model, depending on detail. This is due to the simplicity of the 2D BEM approach discussed in chapter 2.1.2. The program only offers elastic representation of the material, so simplification of naturally occurring phenomena is needed. However, this approach can give quick results and can be useful in the preliminary design of underground projects and parameter analysis, such as sensitivity study of input parameters of a given project. The quick computation of the program allows for interactive interpretation of results in various ways.

As for shortcomings of the code, a few can be named. The model will never be exact, as the modelling of the material as completely elastic and the BEM's incompetence in dealing with discontinuities might over-simplify the problem.



---

## Phase<sup>2</sup>

Phase<sup>2</sup> is quite widely used for elasto-plastic 2D modelling, both for underground structures and surface modelling of slides and pit mines for example. The program is in two components, one CAD (Computer Aided Design) based writer or modelling interface, and one interpretation interface where results are handled, and can be presented in various ways for maximum data representation. The program builds its calculations on FEM, which enables more comprehensive problem solutions, such as implementation of rock support, discontinuities and presence and affect of groundwater.

## 2.2 Rock Mass Classification Systems

There are many ways to evaluate what kind and how much rock support is needed and many systems have been developed to help us with those evaluations. Most of those systems are based on experience and depend on the rock mass quality and the purpose of the excavation. Other assessments are based on analytical methods, like numerical and physical modelling of the excavation, or observation methods during excavation.

### 2.2.1 Q system

The original Q-system is based on data from around 200 tunnel excavations. The data showed correlation between the estimated rock mass quality and the amount of permanent rock support with respect to stability. A graphical system was developed from this data based on the Q-value which is a numerical composed of six factors as can be seen in figure 2. Guidelines for assigning values to the factors are listed in Appendix A. The factors are as follows (Barton et al., 1974):

- RQD: Rock quality design. The RQD value shows how intact the rock mass is. It is the ratio of parts of a drilled core that are 10 cm or longer.
- Jn: Joint set number. The number of joint sets in the core shows the complexity of the jointed rock mass.
- Jr: Joint roughness number. The number is a measurement on the roughness of the joint walls and how much friction creates when sheared.
- Ja: Joint alteration number. The number is a measurement on how much alteration has affected the joints. The amount and type of filling can affect the friction regardless to the roughness of the joints.
- Jw: Joint water reduction factor. The factor is a rough measurement on the water inflow in the tunnel.
- SRF: Stress reduction factor. SRF is evaluation of the interaction of stress and strength in the rock mass.

The Q- value can be broken into three main components:  $RQD/Jn$  is the relative block size,  $Jr/Ja$  is the inter-block shear strength and  $Jw/SRF$  is evaluation of the active stresses

---

in the rock mass.

The plot in figure 2.2 shows the intensity of rock support based on the Q value and a ratio of the size and ESR value for the tunnel. ESR stands for excavation support ratio and is categorized evaluation of the need of support depending on the purpose of the excavated area; the higher stability the excavation demands, the lower the ESR value. For example a nuclear powerstation cavern has a ESR value of 0,8 and a temporary mining opening has a value between 5 and 10 (Barton et al., 1974)).

The Q-system is not applicable for all circumstances and in some situations enhancements should be made to the system in order to get the most reliable results. In the extremities of the Q-value the results become less reliable and the optimal Q-value range for the system is between 0,1 and 40 (Broch & Palmstrom, 2006).

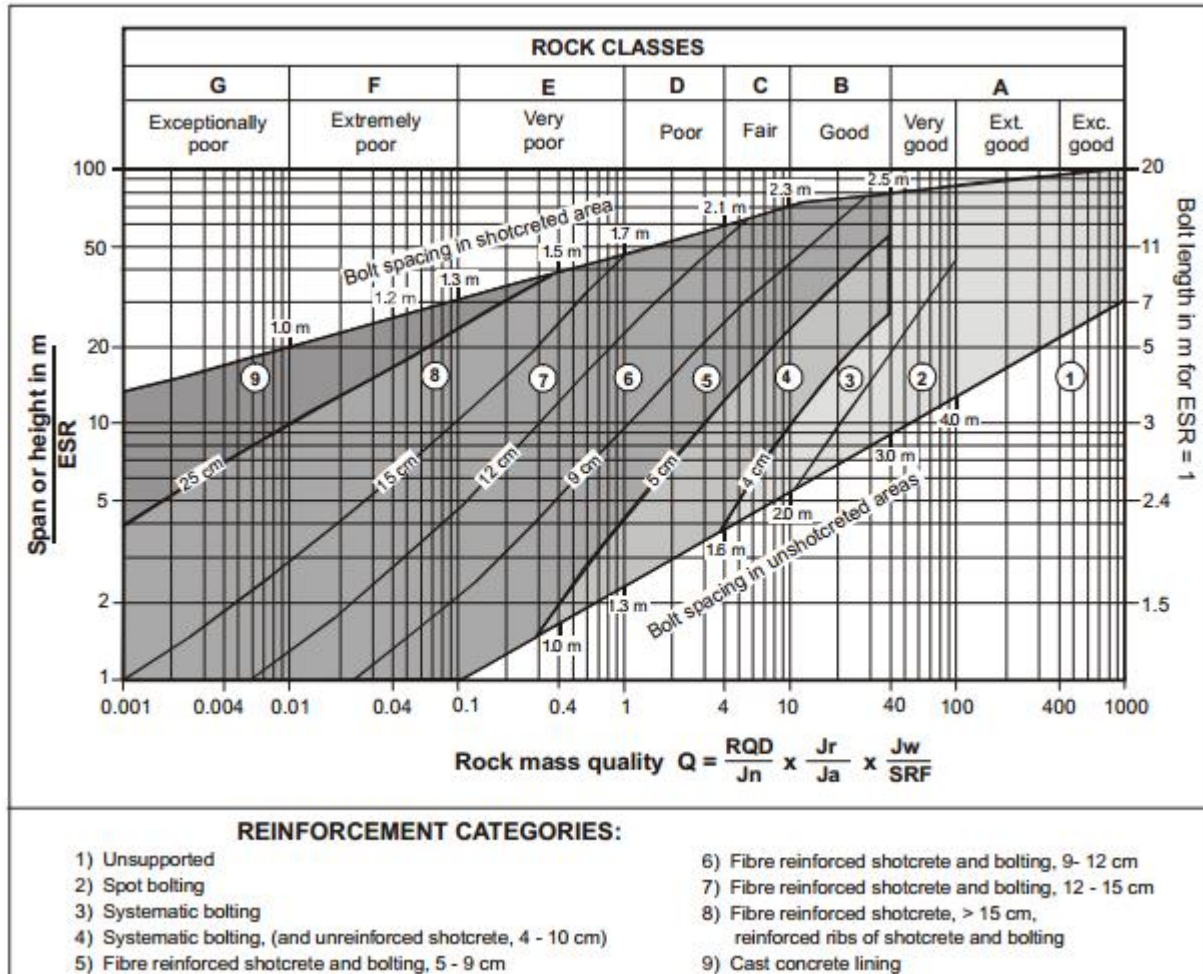


Figure 2.2: The Q- system graph (Barton et al., 1974)

## 2.2.2 Rock Mass Rating, RMR

The RMR system, or the Geomechanics system, is based on 6 parameters of the rock mass and was introduced by Bieniawski in 1976. The parameters are all measurable from borehole data or in the field and are as follows:

- Uniaxial compressive strength of intact rock.
- Rock quality designation, RQD.
- Spacing of discontinuities.
- Condition of discontinuities.
- Groundwater condition.
- Orientation of discontinuities.

The rock mass is assigned numerical value for each of those factors following table where guidelines of values for each parameter are listed. The total sum of the factors then gives the final RMR value. The table can be seen in Appendix A. A large disadvantage of the RMR system is that it does not take the stress field into account (Myrvang, 2001).

The RMR value can be used as guideline in design of rock support in underground openings, according to table 2.1 (Bieniawski, 1976).

**Table 2.1:** The RMR classification system (Bieniawski, 1989)

Rock mass class	Excavation	Rock bolts (20 mm diameter, fully grouted)	Shotcrete	Steel sets
I – Very good rock <i>RMR: 81-100</i>	Full face, 3 m advance	Generally no support required except spot bolting		
II – Good rock <i>RMR: 61-80</i>	Full face, 1-1.5 m advance. Complete support 20 m from face	Locally, bolts in crown 3 m long, spaced 2.5 m with occasional wire mesh	50 mm in crown where required	None
III – Fair rock <i>RMR: 41-60</i>	Top heading and bench 1.5-3 m advance in top heading. Commence support after each blast. Complete support 10 m from face	Systematic bolts 4 m long, spaced 1.5-2 m in crown and walls with wire mesh in crown	50-100 mm in crown and 30 mm in sides	None
IV – Poor rock <i>RMR: 21-40</i>	Top heading and bench 1.0-1.5 m advance in top heading. Install support concurrently with excavation. 10 m from face	Systematic bolts 4-5 m long, spaced 1-1.5 m in crown and walls with wire mesh	100-150 mm in crown and 100 mm in sides	Light to medium ribs spaced 1.5 m where required
V – Very poor rock <i>RMR: &lt; 20</i>	Multiple drifts 0.5-1.5 m advance in top heading. Install support concurrently with excavation. Shotcrete as soon as possible after blasting	Systematic bolts 5-6 m long, spaced 1-1.5 m in crown and walls with wire mesh. Bolt invert	150-200 mm in crown, 150 mm in sides, and 50 mm on face	Medium to heavy ribs spaced 0.75 m with steel lagging and forepoling if required. Close invert

---

### 2.2.3 GSI

Following the development of the Hoek-Brown failure criterion (chapter 2.3.1) it was apparent that some quantifiable means of assessing rock mass qualities were needed for the criterion to function to its full potential. At the time, there were two major classifications systems, the RMR system (chapter 2.2.2) and the Q system (chapter 2.2.1), and the RMR was at first used alongside the Hoek-Brown failure criterion. Experience with RMR had been relatively good, except for low quality rock where it becomes unreliable as it depends on the RQD value that becomes near zero and therefore meaningless in very weak and broken rock. By excluding factors from RMR, accounting for groundwater and stress parameters it became useful. However, the inability of RMR when it came to low quality rock called for a new system for rock classification as development of the failure criterion progressed (Marinos et al., 2005).

This new system was GSI (Geological Strength Index), and based its classification on geological observation in a mostly qualitative way, and referral to a chart (figure 2.3) where observed features of the mass are given rating. It excludes RQD, which is essential function of the RMR and Q systems, in order to be applicable for poor quality rock mass (Marinos et al., 2005). In addition, The system has been enhanced specially for use with very weak rock, during work in Athens Schist Formation (Hoek, Marinos, & Benissi, 1998).

From the estimates GSI value, alongside with the petrographical constant,  $m_i$ , and the intact rock strength,  $\sigma_{ci}$ , the necessary properties for numerical analysis can be calculated through set of equations.

## 2.3 Rock Mass Quality

When assessing how well the rock mass will be able to withstand the changes imposed to the stability by excavation of material in previously stable environment, some characteristics of it have been researched in depth in order to obtain understanding of its behaviour upon such changes. The behavioural characteristics that most affect the outcome of the numerical modelling approach, i.e. how the rock mass fails when overstressed and how it deforms around the opening, are reviewed below.

### 2.3.1 Failure Criteria

Various failure criteria have been made to predict the possible response of material upon changed condition. The two most used in rock mechanics are the Mohr - Coulomb failure criterion and the Hoek - Brown failure criterion, which will be used in the modelling work of this thesis. They will be briefly reviewed in the following chapters.

#### **Mohr - Coulomb Failure Criterion**

The Mohr-Coulomb failure criterion can be imposed on brittle material like rock mass for prediction of the behaviour, and eventually failure, when subjected with shear stress or







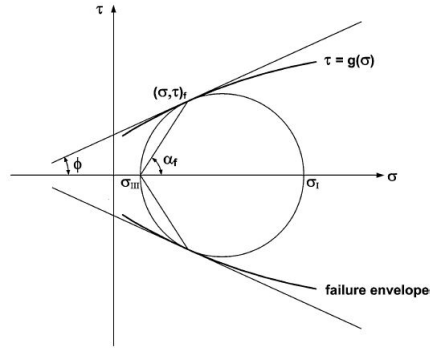
<p><b>GEOLOGICAL STRENGTH INDEX FOR JOINTED ROCKS (Hoek and Marinos, 2000)</b></p> <p>From the lithology, structure and surface conditions of the discontinuities, estimate the average value of GSI. Do not try to be too precise. Quoting a range from 33 to 37 is more realistic than stating that GSI = 35. Note that the table does not apply to structurally controlled failures. Where weak planar structural planes are present in an unfavourable orientation with respect to the excavation face, these will dominate the rock mass behaviour. The shear strength of surfaces in rocks that are prone to deterioration as a result of changes in moisture content will be reduced if water is present. When working with rocks in the fair to very poor categories, a shift to the right may be made for wet conditions. Water pressure is dealt with by effective stress analysis.</p>		<p><b>SURFACE CONDITIONS</b></p> <p><b>VERY GOOD</b> Very rough, fresh unweathered surfaces</p> <p><b>GOOD</b> Rough, slightly weathered, iron stained surfaces</p> <p><b>FAIR</b> Smooth, moderately weathered and altered surfaces</p> <p><b>POOR</b> Slickensided, highly weathered surfaces with compact coatings or fillings or angular fragments</p> <p><b>VERY POOR</b> Slickensided, highly weathered surfaces with soft clay coatings or fillings</p>				
<p><b>STRUCTURE</b></p>		<p><b>DECREASING SURFACE QUALITY</b> →</p>				
 <p><b>INTACT OR MASSIVE</b> - intact rock specimens or massive in situ rock with few widely spaced discontinuities</p>	90			N/A	N/A	
 <p><b>BLOCKY</b> - well interlocked undisturbed rock mass consisting of cubical blocks formed by three intersecting discontinuity sets</p>	80	70				
 <p><b>VERY BLOCKY</b>- interlocked, partially disturbed mass with multi-faceted angular blocks formed by 4 or more joint sets</p>		60				
 <p><b>BLOCKY/DISTURBED/SEAMY</b> - folded with angular blocks formed by many intersecting discontinuity sets. Persistence of bedding planes or schistosity</p>			50			
 <p><b>DISINTEGRATED</b> - poorly interlocked, heavily broken rock mass with mixture of angular and rounded rock pieces</p>				40		
 <p><b>LAMINATED/SHEARED</b> - Lack of blockiness due to close spacing of weak schistosity or shear planes</p>					30	
					20	
					10	
		N/A	N/A			

Figure 2.3: The GSI chart (Marinos et al., 2005)



**Figure 2.4:** The Mohr-Coulomb failure envelope represented on a Mohr diagram (Labuz & Zang, 2012)

normal stress. The criterion utilizes the relationship between the shear strength and the maximum and minimum principal stresses, taking into account two material constants, to represent failure envelope as can be seen in figure 2.4. When the circle through the two principal stresses intersect the failure envelope in the plane of the normal stress induced, failure can be predicted. The two material constants are the cohesion,  $c$ , and the internal friction angle,  $\phi$ , where  $c$  represents the intercept of the failure envelope on the  $\tau$  axis and  $\phi$  is the angle of the line (Labuz & Zang, 2012). The intermediate principal stress is negligible in the calculations, although Myrvang (2001) states it can influence in some cases.

### Hoek - Brown Failure Criterion

The Hoek-Brown failure criterion was first introduced by Hoek and Brown in 1980. The criterion was developed in attempt to improve the input data for analytical methods for design of underground excavations in hard rock. It is based on examination of wide range of data from research on the brittle failure of both intact rock and rock discontinuities, as well as model studies of jointed rock mass behaviour. The data showed the relationship between the major and minor principal stresses and between shear and normal stresses was non-linear, on the contrary to what the aforementioned Mohr-Coulomb criterion assumes. The original version of the empirical relationship between the principal stresses is presented in equation 2.2 (Hoek & Brown, 1980).

$$\frac{\sigma_1}{\sigma_c} = \frac{\sigma_3}{\sigma_c} + \sqrt{m \frac{\sigma_3}{\sigma_{c_i}} + s} \quad (2.2)$$

In equation 2.2  $m$  and  $s$  represent problem specific constants. The strength parameter,  $m$ , is material constant and table showing values for various rock types can be seen in Appendix A. The  $s$  constant indicates the continuity of the rock mass, where  $s = 1, 0$  represents intact rock and lower values represent gradually more jointed rock.

The criterion was improved through the years in pursuit to eliminate major limitations

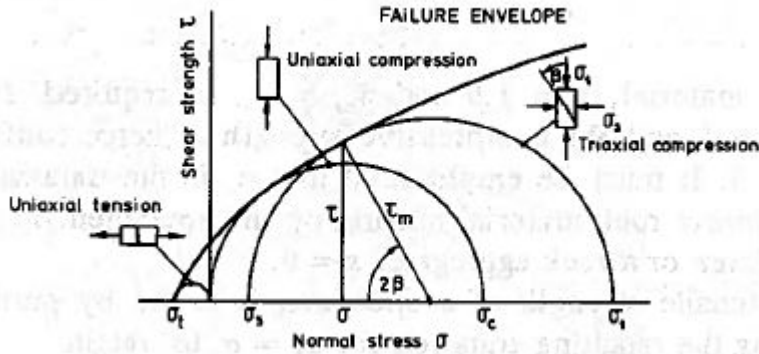


**Figure 2.5:** The Hoek-Brown failure envelope showing the relationship between major and minor principal stresses and the shear strength (Hoek & Brown, 1980)

of it and allowing wider usage. The major input of this new method was its connection to geological observation. One of the main shortcomings of it was the scale of the problem, where test samples might be intact but due to small size not depicting the actual circumstances accurately. Up until introduction of the GSI classification system, the RMR system had been used as described in chapter 2.2.3. A generalized version of the criterion (equation 2.3) was presented in 1997, where the factors  $m_b$ ,  $a$  and  $s$  are derived from GSI classification and the disturbance factor  $D$ , a measurement on how badly the rock nearest the opening has been affected by the excavation. A table showing guidelines for determining the factor  $D$  can be found in Appendix A. (Hoek & Brown, 1997; Hoek et al., 2002).

$$\sigma_1^i = \sigma_3^i + \sigma_{ci} \left( m_b \frac{\sigma_3^i}{\sigma_{ci}} + s \right)^a \quad (2.3)$$

The generalized Hoek-Brown criterion uses the major and minor effective principal stresses and the uniaxial compressive strength of the intact rock. The shear strength,  $\tau$ , can be derived from the criterion, so that a failure envelope can be plotted as in figure 2.5, and the criterion can be used as yield criterion in numerical analyses.

## 2.3.2 Rock Mass Deformation

How the rock mass in question is assumed to behave and respond upon altered condition, as is the case in the numerical analyses carried out in this thesis, is highly dependant on the deformability. Here the main aspect of rock mass deformation will be discussed.

### Elasticity and Plasticity

Deformation modulus indicates the strain if material when subjected with applied load. The nature of deformation has been classified as elastic and plastic (with variations), based on behaviour when the load is relieved. Elastic material returns to its original



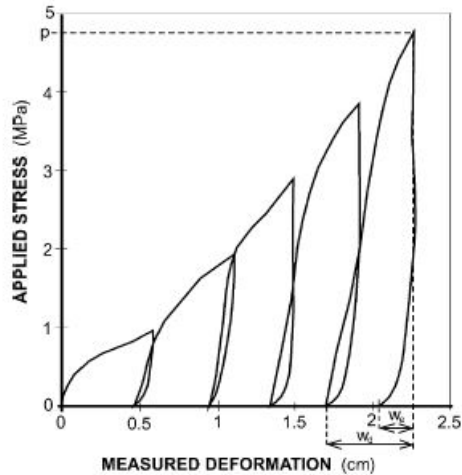


**Figure 2.6:** Typical stress versus deformation curve from deformability test on rock mass from the Tala project (Palmström & Singh, 2001)

shape whereas plastic deformation is non-reversible. The deformation characteristics are material-specific, and defined by three different moduli (ISRM, 1975):

- Modulus of elasticity ( $E$ ): The Young's modulus is the ratio of stress and strain, within the proportionality of the material.
- Modulus of deformation of rock mass ( $E_m$ ): The stress - strain ratio of rock mass under loading, representing both elastic and non-elastic properties of the mass.
- Modulus of elasticity of rock mass ( $E_{em}$ ): The stress - strain ratio of rock mass under loading, representing only the elastic properties.

Estimating or measuring the deformation modulus can often prove problematic and at high cost as Palmström and Singh (2001) describe. It relies on identifying a sample for lab tests or a location for in-situ measurement, that is representative for the rock mass. Indirect methods to obtain value of  $E_m$  have been developed, many of which depending on values that are more easily acquired, like ratings from rock mass quality classification systems. However it is generally recommended to use multiple indirect methods to be able compare results and estimate their reliability. In addition to the deformation moduli, the Poisson's ratio  $\nu$ , the ratio of the radial and axial strain, is used to describe the deformation properties of the material.

When implementing the deformation characteristics as a variable in numerical analysis, the modulus of deformation ( $E_m$ ) cannot be considered absolute value, rather as estimate on the magnitude of it. That is partly due to how much discontinuities affect the deformation characteristics of the rock mass, as Harrison and Hudson (1997, p 176) stated that in-situ measurements can give values of down to only 7 - 10% of values obtained in the

laboratory. Hoek and Brown (1997) stated that the deformation is dependant on the rock mass strength, and included that in the indirect method proposed (equations 2.4 and 2.5), where ( $E_m$ ) is obtained using  $\sigma_{ci}$ , disturbance (D) and GSI value.

$$E_m(GPa) = \left(1 - \frac{D}{2}\right) \sqrt{\frac{\sigma_{ci}}{100}} * 10^{((GSI-10)/40)} \quad (2.4)$$

$$E_m(GPa) = \left(1 - \frac{D}{2}\right) * 10^{((GSI-10)/40)} \quad (2.5)$$

Equation 2.4 applies when the uniaxial compressive strength of intact rock,  $\sigma_{ci}$ , is 100 MPa or less and equation 2.5 when  $\sigma_{ci}$  exceeds 100 MPa. The difference lies in that for stronger rock material the discontinuities control the deformation whereas for weaker material it is the intact rock pieces that account for the deformation.

Hoek and Brown (1997) also proposed post failure characteristics for rock of varying quality as seen in figure 2.7. Good quality rock (figure 2.7 a) is expected to fail in an elastic - brittle way, where upon peak stress a sudden drop in strength is observed.

The failure of rock of average quality (figure 2.7 b) is generally termed as strain softening, where upon failure it is safe to assume that the GSI value drops to represent the broken rock mass. Other characteristics of the mass, that are related to GSI change accordingly and deformation after failure happens at constant stress level and is controlled by the compressive strength of the broken rock mass.

Figure 2.7 c illustrates expected progressive failure of soft rock of poor quality. It is expected to behave perfectly plastically after failure and deform at constant stress level.

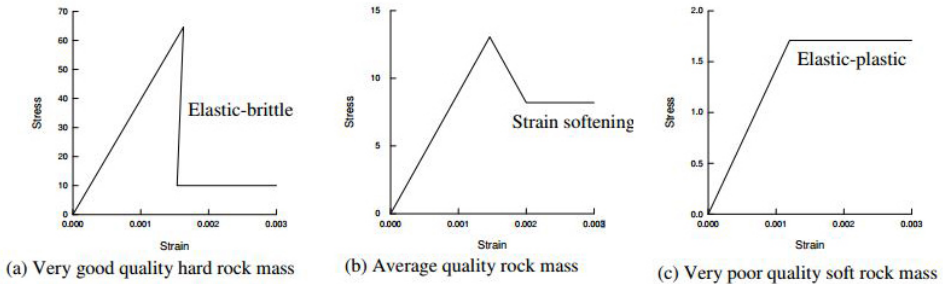


**Figure 2.7:** Post failure characteristics of rock based on quality (Hoek & Brown, 1997)

# Problem Description

## 3.1 Geology of the Bhutan Himalaya

The ongoing orogeny of the Himalayan region was started by the collision of the Indian and the Eurasian plates. Complex fault systems extend throughout the collision area, from Pakistan in the west to Myanmar in the east, bearing with them tectonostratigraphic units and structures. The tectonic frame of Bhutan is characterized by these structures, as some of the major ones are apparent in the region: the Siwalik Group, the Main Boundary fault (MBF), the Lesser Himalayan Sequence (LHS), the Main Central Thrust (MCT), the Greater Himalayan Sequence (GHS) and the South Tibetan Detachment (STD) (figure 3.1). However there are distinctive features in the Bhutan region, where low-grade metasedimentary rocks lie above the GHS as klippen and the Kakhtang thrust that lies out of sequence, structurally above the klippen, doubling the exposed thickness of the GHS (Grujic et al., 2002).

The GHS covers most of Bhutan. There it consists mainly of orthogneiss and metasedimentary rocks (Gansser, 1983), intruded by granite. The GHS is divided in two units around the Kakhtang thrust, the lower one ranging south to the MCT and the higher one reaching north to the STD. South of the MCT is the LHS, ranging south to the MBT. The LHS is characterized by low grade metasedimentary rock like quartzite, phyllite and limestone and can be divided in three groups in western Bhutan (Tobgay et al., 2010; McQuarrie et al., 2008):

*Daling-Shumar group* is a set of two formations, the Daling formation on top of the Shumar formation. The Daling formation is characterized by quartzite interbedded schist and phyllite, and bodies of orthogneiss with feldspar augen. The Shumar formation is fine grained quartzite, medium to thick planar bedded (McQuarrie et al., 2008), with occurrence of cm to m scale thick phyllite or schist interbeds (Tobgay et al., 2010).

*Baxa group* is in western Bhutan divided into the Phuentsholing formation with dark slate

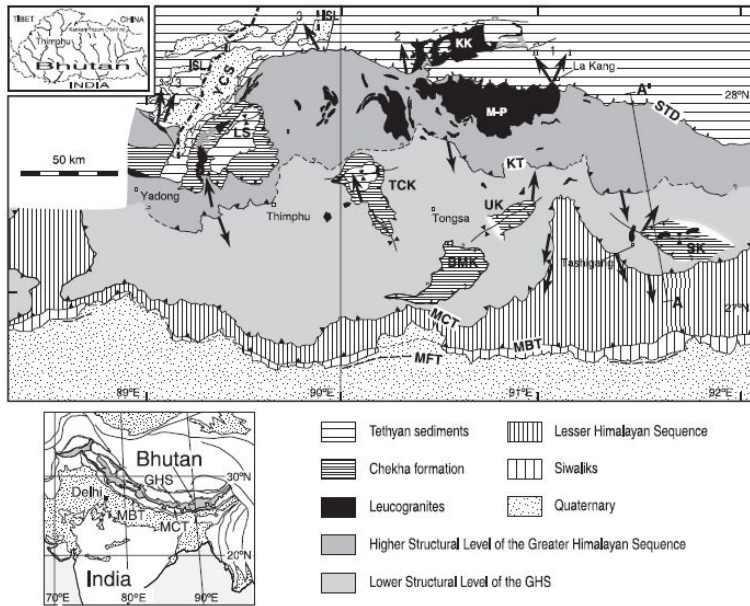


**Figure 3.1:** Large scale geological map of Bhutan, showing the main units in the tectonostratigraphy (Grujic et al., 2002)

and phyllite interbedded with limestone, dolomite and quartzite, and the Pangsari formation with grey/green phyllite interbedded with red to pink marble and greenish quartzite (Tobgay et al., 2010).

*The Jaishidanda formation* is a ~1 km thick formation and in western Bhutan it consists of biotite-rich garnet bearing schist with quartz boudins interbedded with grey quartzite with biotite-rich laminations and interbeds of biotite schist.

The Paro formation can be observed in a window in the GHS north of the town of Chhukha in figure 3.2, as well in the transition zone around the MCT. It consists of high-grade metasedimentary and calcareous rocks including calc-silicate rocks, marble, quartzite, quartz-garnet-staurolite-kyanite schist with subordinate feldspatic schist and bodies of two mica granite-composition orthogneiss (Gansser, 1983; Tobgay et al., 2010). The Paro Formation is overlying the GHS as a out of sequence thrust (Tobgay et al., 2010). The project location of both Chhukha and Tala hydro electric plants is situated in close proximity to the MCT, and thereby the Paro Formation thrust sheet as can be seen in figure 3.2.

### 3.1.1 Challenges of tunnelling in the Himalayas

Time of construction is generally one of the decisive factors in the design. In the early stages of planning, problems that might be encountered during the excavation need to be addressed and countered and that involves prediction of the rock mass occurrence and its

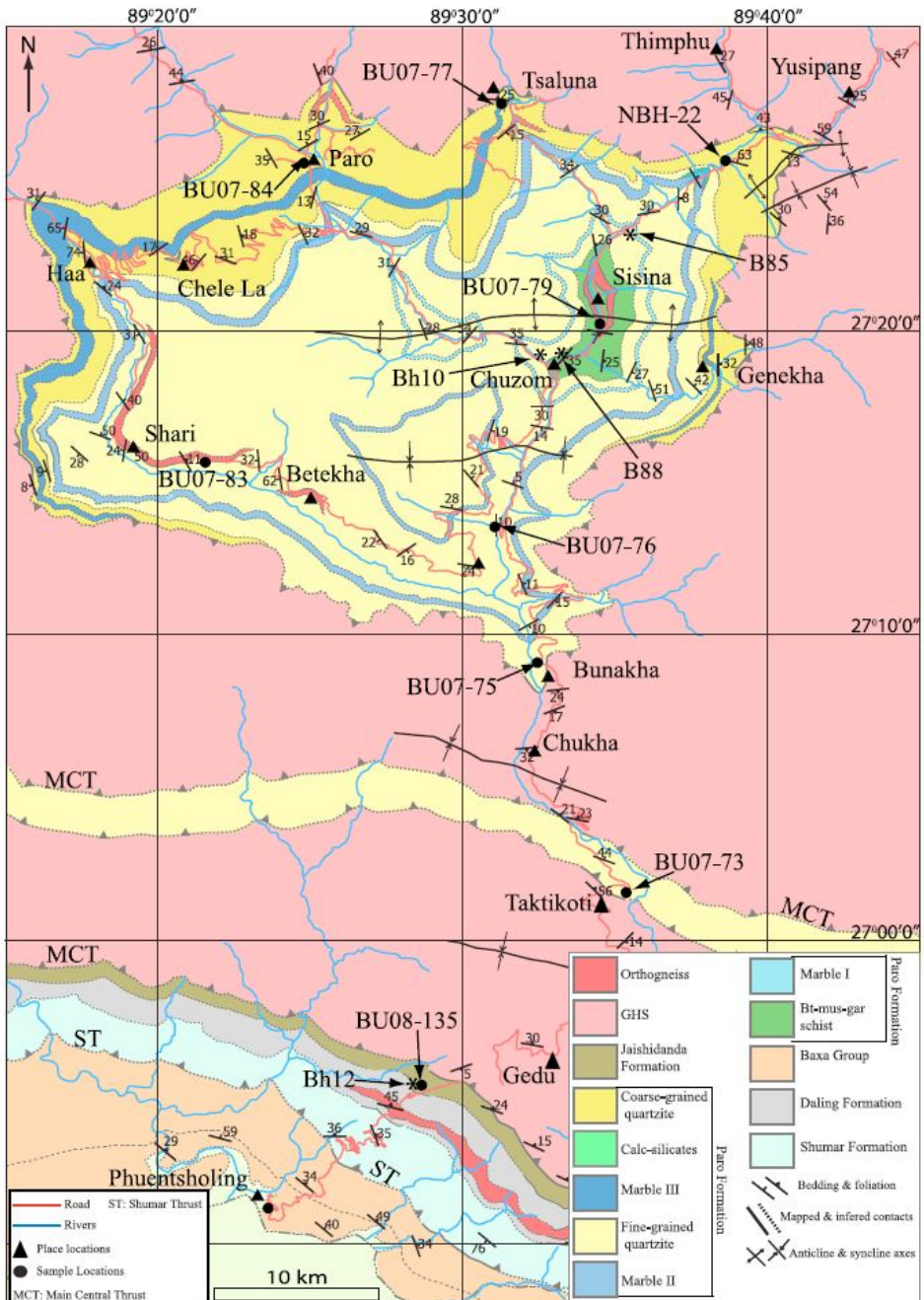


**Figure 3.2:** Geological map of the Wang Chhu river basin and the Paro formation window. The location of the two powerplants is just south of the town of Chhukha (Tobgay et al., 2010)

quality at each location. As a result of the tectonic activity, the Himalayan mountain range is overridden by complex network of faults and diverse conditions where massive deformation, faulting, shearing, fracturing and weathering greatly affect the rock mass. Due to the complexity the rock mass becomes unpredictable, that can lead to increased time of construction, more extensive rock support than designed and, in worst cases, hazardous conditions for work force and equipment. In review of four tunnelling projects in Nepal, Panthi and Nilsen (2007) revealed large error in predicted rock mass quality in all four projects. Although the cause of error can not be singled out as complex geological setting, it is evident that it plays important role. Experience in said condition might have been insufficient and pre-construction investigation as well. To minimize the uncertainty Panthi & Nilsen recommended systematic and detailed pre-construction phase investigation, where comprehensive estimate of most or all aspects of the project and location is reviewed during the feasibility and design phase, in order to optimize the design and estimates in accordance to the case at hand. The process is detailed in figure 3.3.

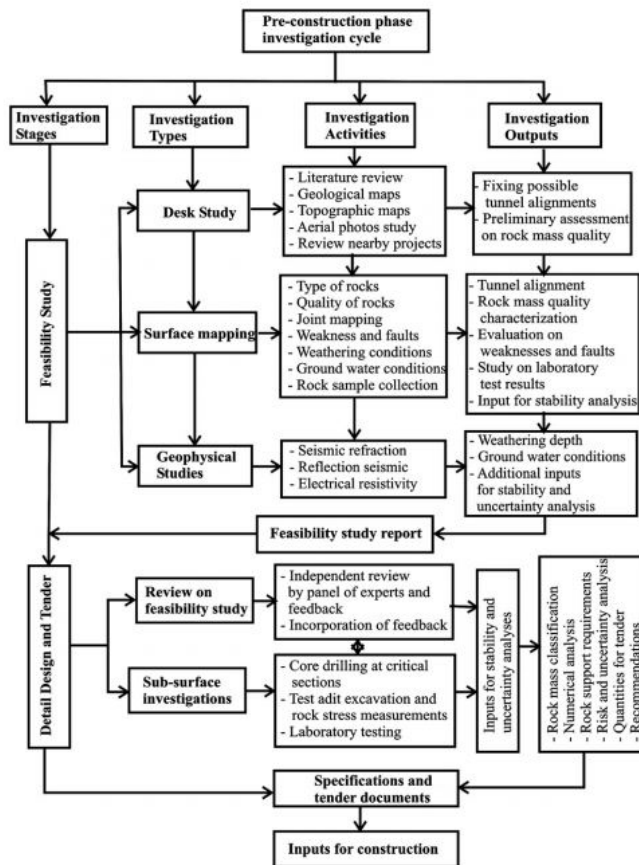


**Figure 3.3:** The pre-construction investigation system recommended by Panthi and Nilsen for work in the Himalayas (Panthi & Nilsen, 2007)

## 3.2 The Tala Hydropower Project

The Tala HE powerplant project in the Wang Chhu river system in The Himalayan Kingdom of Bhutan has been faced with numerous problems during construction and while operating. Instability in the excavated powerhouse and transformer caverns, where rock bolts have failed and collapse during excavation slowed down construction.

### 3.2.1 In General

Following the success of Chhukha hydroelectric powerplant, many smaller plants were constructed and in the late 1980's discussions about mega scale hydropower project commenced. In 1990 a group of experts came down to two feasible locations, Tala being one of them, and field investigation of the site was carried out. In late 1993 the detailed project report (DPR) was finalized. The Tala Hydroelectric Power Project Authority (THPA) was established in order to manage the project and construction started in 1996. The project was designed as a run of the river scheme, 3 km downstream of the Chhukha Hydroelectric Project. The project includes various underground structures; three large desilting chambers, 23 km long headrace tunnel, underground machine hall, transformer hall, 3,2 km long tailrace tunnel and other supplementary structures. The plant utilizes 861,5 m fall and the installed capacity of the powerplant is 1020 MW (6 x 170 MW). The average rock overburden of the two main caverns is about 500 m, but it ranges from 300 – 700 m in the project area. The dimensions of main features are listed in table 3.1.

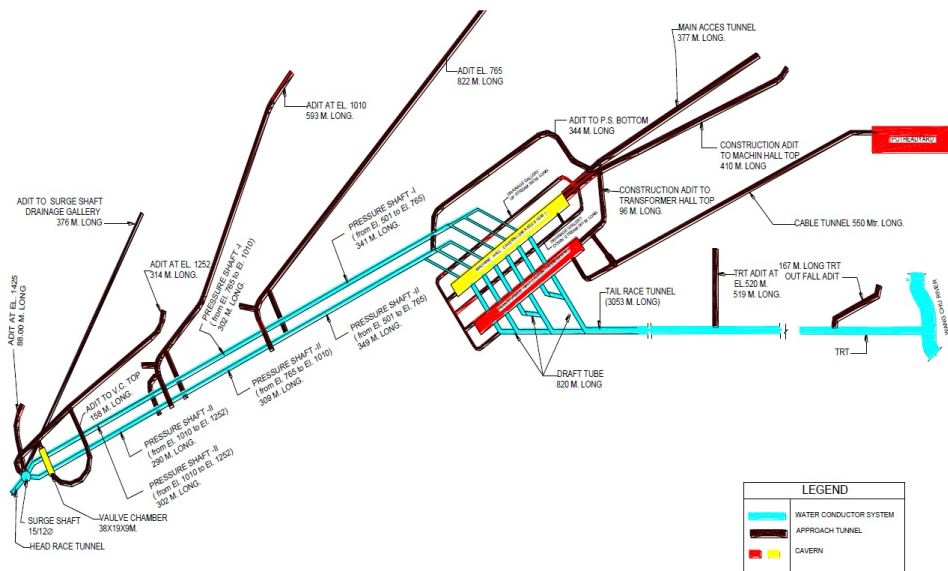


**Figure 3.4:** The layout of the powerhouse complex of Tala hydroelectric plant (Report on quality control, 2006)

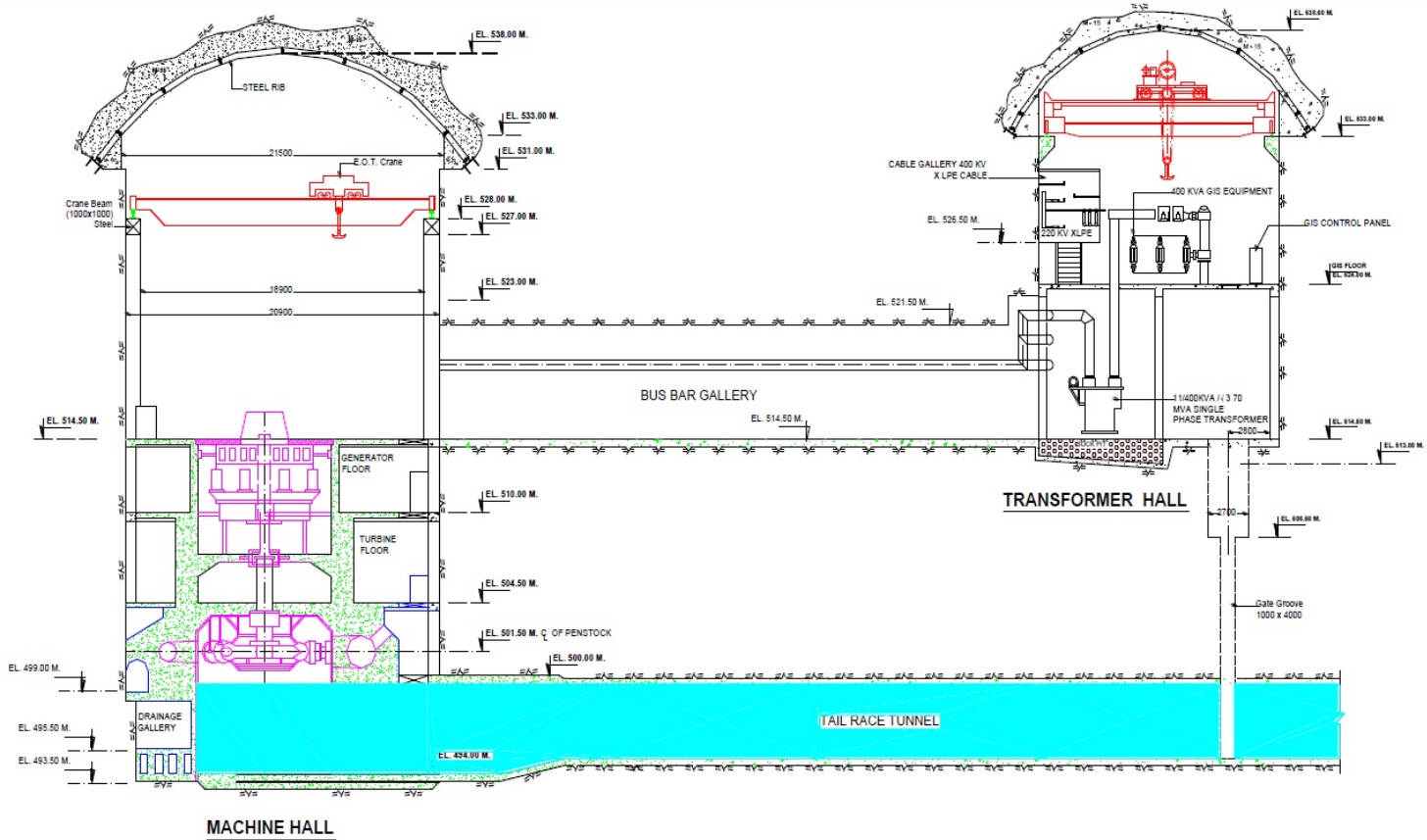


**Figure 3.5:** The profile of the powerhouse complex of Tala Hydroelectric plant (Report on quality control, 2006)



---

**Table 3.1:** The main features of The Tala Hydroelectric Project

### **Tala Hydroelectric Project**

Location	: 26,87°N, 89,58° E
Installed capacity	: 6 x 170 MW
Dam	: 92 m high concrete gravity dam
Intake level	: 1342.5 masl
Desilting Chambers	: 3 x 250 m x 13,965 m x 18,5 m (LxWxH)
Headrace tunnel	: 22970 m
<b>Power House Complex</b>	
Machine hall	: 206 m x 20,4 m x 44,5 m (LxWxH)
Machine hall long axis	: N37°W
Elevation of service bay	: 514,5 masl
Size of service bay	: 42 m x 20,4 m (LxW)
Drainage /cable anchor gallery	: 590 m x 3 m x 4 m (LxWxH)
Transformer hall	: 191 m x 16 m x 26,5 m (LxWxH)
Pillar width	: 39,4 m
Bus ducts	: 3 x 39.4 m x 10 m x 8.5 m (LxWxH)
EOT cranes in machine hall	: 2x 200 T / 40 T / 20 T
Crane span (machine hall)	: 19,5 m
Crane beam support (machine hall)	: Steel column beam arrangement
EOT crane in transformer hall	: 5 T
Crane span (transformer hall)	: 15 m
Crane beam support	: Steel bracket anchored to cavern wall
Main access tunnel	: D-shaped, 377 m x 7,5 m x 8,0 m (LxWxH), 410 m, 7 m from top of machine hall
Construction adits	: D-shaped, 70 m long 7 m from top of trans- former hall
Unit tailrace gates	: 6 x 4,0 m x 4,5 m vertical lift type
<b>Peripheral Drainage Gallery</b>	
Size	: 3 m x 4 m (WxH)
Level	: 1300 masl
Location	: 25 m from C/L of surge shaft

### **3.2.2 Local Geology**

The powerhouse complex of the project lies in folded sequence of phyllites, phyllitic quartzite, quartzite and amphibolite of the Shumar formation. The high-grade metamorphosed rock is very thinly foliated with small spacing and with foliation dip of 30° to 50° towards the heading. The rock is highly folded and aside from the foliation dip, at least 5 sets of random joint sets can be found, with dip varying from 22° to 55° (see table 3.2) and microfractures and joints were observed in the quartzite and the phyllitic quartzite.

**Table 3.2:** Measured joints around the Powerhouse complex (Singh et al., 2002)

No.	Strike		Dip	Spacing [cm]	Continuity [cm]	Nature
Foliation	N65°E–S65°W N70°W–S70°E	to	35°–60° : N25°W to N20°E	10–300	500–1200	Rough Undulating
J1	N20°W–S70°E N15°W–S75°E	to	40°–80° : N70°E to N75°E	100–200	200–500	Rough Undulating
J2	N–S to N30°E–S30°W		25°–80° : W to N60°W	5–200	200–1000	Rough Undulating
J3	N30°E–S30°W to N20°E– S20°W		30°–50° : S60°E to S70°E	6–20	200	Rough Planar
J4	N50°W–S50°E N30°W–S60°E	to	60°–70° : S40°W to S60°W	10–200	200–500	Smooth Planar
J5	N80°E–S80°W N70°W–S20°E	to	40°–70° : S10°E to S20°W	20–200	200–500	Rough Planar

The folding, foliation planes and well-developed joints form wedges in both the roof and the walls of the caverns. The plunge of the folding in a 2 x 2 m exploratory drift in the centre of the machine hall was measured and varied from 10° to 42°, and 10 folds could be recorded. The joints were mapped in this drift as well. Other observations were made in this drift, for example clay gouge filled shear seams and, with dipping varying from 17° – 85°, and places where crushed rock could be found. The orientation of the long axis of the caverns is N37°W – S37°E and crosses the strike of foliation and is at an varying angle to the strike of folding between 50° to 150°.

### Rock Mass Properties

The quality and other essential properties of the rock mass in the project area was initially measured and/or assessed in the 2 x 2 m exploratory drift in the machine hall. The rock quality index, Q value, was assessed and varied from 0,24 - 13,2 and a representative GSI value of 50 assessed (Chowdhry, 2007). More detailed estimate is reviewed in table 3.3 These indices are explained in chapter 2.2, and their meaning elaborated. In this drift, samples were collected and tested in the lab. Hydrofracturing was employed in order to estimate the orientation an magnitude of the principal stresses, and the results from that and the stress field in general will be discussed in chapter 3.2.2.

The samples were tested, although in limited number, and initial values for the necessary rock mass parameters needed for numerical analysis. The results are based on the assessed GSI value of 50, and can be seen in table 3.4. The results were used by the Indian NIRM to construct numerical model with the 3–DEC software, that was used to aid in the design the rock support system in the crown of the Tala machine hall (Chopra & Gupta, 2003).

On another occasion, more samples were collected, cores drilled and the host rock inspected with bore hole cameras. That was after a extensive collapse in the crown during the widening of it. Bore hole camera investigation of around 25 m depth revealed great amounts of quartz and phyllite and places where pieces of quartz from the quartzite and

**Table 3.3:** Estimate of rock mass properties along the powerhouse cavern. Machine hall is at RD 39 m - RD 245 m (Chowdhry, 2007)

RD [m]	Rock Type	RMR	Q	GSI	Rock Mass Quality
0-18	Amphibolite and Quartzite	47	10,5	52	Good
28-36	Quartzite and Amphibolite	19	0,11	27	Very poor
32-60	Phyllitic Quartzite	39	7,5	44	Fair
60-80	Amphibolite and Quartzite and Quartzite	50	10,5	52	Good
80-100	Phyllitic Quartzite	50	14	52	Good
100-120	Quartzitic Phyllitic Quartzite and Amphibolite	44	3,0	36	Poor
120-140	Quartzitic Phyllitic Quartzite and Amphibolite	38	7,5	43	Fair
140-160	Quartzite, Phyllitic Quartzite and Amphibolite	54	12,0	56	Good
160-180	Quartzite	44	14,0	46	Good
180-200	Quartzite	47	9,0	52	Fair
200-220	Quartzite and Amphibolite	50	9,75	52	Fair
200-220	Quartzite with Phyllitic Quartzite and Amphibolite	47	9,75	52	Fair

**Table 3.4:** Primary rock mass parameters obtained in pre-construction exploration drift and literature. (Chopra & Gupta, 2003)

Unconfined compressive strength	: 50 MPa
Poisson's ratio	: 0,2 (based on literature)
Mi	: 15 (based on literature)
Young's modulus	: 14 GPa
Cohesion	: 3.7 MPa
Angle of internal friction	: 35°

quartz boudins had fallen in the bore holes and formed cavities, consequently increasing the hole diameter. Abundance of foliation joints and white rings, up to 10 cm thick, of quartz boudins could be observed as well as numbers of folded quartz veins. Using the bore hole camera open cracks were seen at depths up to 3,5 m above the crown.

150 cores were drilled, but only few of the could be used as representative sample as they did not meet the dimensional requirements as the foliation and jointing of the blocks the samples were taken from led to poor core recovery. Furthermore, none of the usable samples were from the phyllite that accounted for about 28% of the rock mass in the machine hall, but average properties of phyllitic quartzite is shown in table 3.5. The cores were tested in the lab and the following test were done:

- Uniaxial compression test (UCT).
- Triaxial compression test(TCT).

**Table 3.5:** Average rock mass properties of Phyllitic quartzite (Chopra & Gupta, 2003). LR = Linear Regression, SR, NLR = Simplex Reflection, Non-Linear Regression

Parameter	Dry	Saturated
Young's Modulus (GPa)	18,35	12,93
Poisson's Ratio	0,35	0,36
Uniaxial Compressive Strength (MPa)	64,02 (LR) / 63,17 (SR, NLR)	53,67 (LR) / 51,90 (SR, NLR)
Mi	4,18 (LR) / 4,18 (SR, NLR)	3,98 (LR) / 4,49 (SR, NLR)
Cohesion (MPa)	18,56	15,71
Friction Angle (deg.)	28,86	28,33

**Table 3.6:** Rock mass parameters around the powerhouse complex (Chopra & Gupta, 2003)

Properties	Dry sample	Saturated sample
Density (t/m <sup>3</sup> )	2,65	2,56
UCS (GPa)	63,17	51,9
Young's modulus (GPa)	7,95	7,25
Cohesion (MPa)	2,28	1,9
Angle of internal friction (°)	28,3	24,4
GSI	50	50
Mi	4,18	4,49

- Normal and shear stress along joints.

The UCT were done on both dry and saturated samples for Young's modulus and Poisson's ratio, and from the TCT, cohesion and angle of friction parameters for the Mohr - Coulomb failure criterion were obtained. The value of Mi parameter for Hoek - Brown failure criterion calculation was obtained from the RocData software. Joint parameters for normal and shear stiffness were also obtained from samples of 100 mm diameter cores. The rock mass parameters and the joint parameters obtained by NIRM are presented in tables 3.6 and 3.7.

### In-situ Stress Field

In the earlier mentioned exploration drift hydrofracturing tests were performed for assessment of the stress field. The vertical stress was calculated in the conventional way, with overburden value of 410 m, to be 10,865 MPa, and with the hydrofracturing method the orientation of the maximum and minimum horizontal stress was measured to be in N50°W.

**Table 3.7:** Joint parameters around the powerhouse complex (Chopra & Gupta, 2003)

Properties	Value
Shear stiffness (GPa/m)	0,097
Normal stiffness (GPa/m)	10
Cohesion(MPa)	0
Angle of internal friction (°)	25

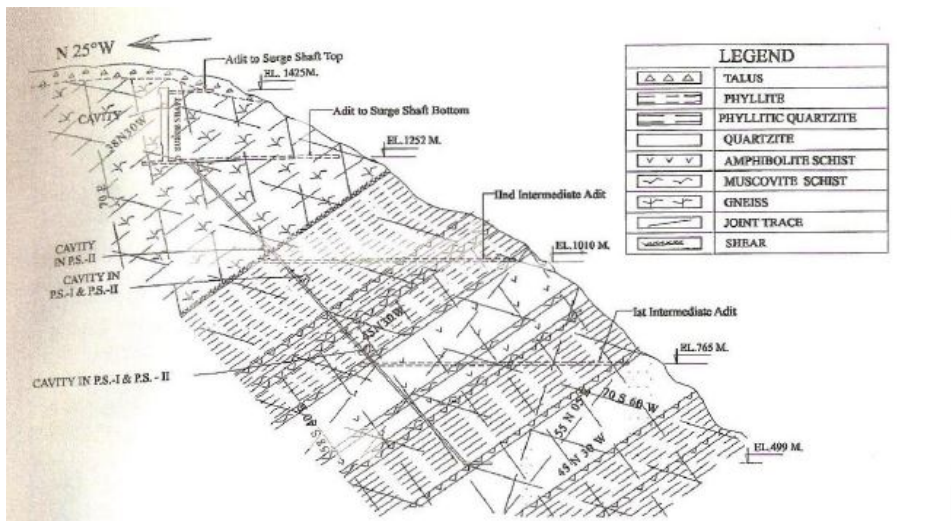


**Figure 3.6:** Cross section through the local geology (Goyal & Khazanchi, 2003)

The ratio between horizontal and vertical stresses was  $K_H = 1,31$  (maximum horizontal stress) and  $K_h = 0,87$  (minimum horizontal stress)(Chopra & Gupta, 2003).

### 3.2.3 The Construction Phase

The excavation of the powerhouse complex started in December 2000, in the central gullet of the machine hall, and in March 2001 excavation started in the transformer hall. Excavation of the two caverns was completed in late 2003, after delays due to failure in the rock mass and more extensive rock support installation than designed.

#### Excavation

11<sup>th</sup> December marked the beginning of the excavation work of the powerhouse complex at Tala hydroelectric plant, with the excavation of 7 m wide central gullet in the crown of the machine hall. The excavation sequence was designed with the crown in three parts and 11 benches, all in three parts, of with staggered formation, so that the whole width was never unsupported at any given time. The excavation method was conventional drill and blast method. The transformer cavern was excavated in the same manner about 40 m downstream of the machine hall. The excavation sequence of the transformer cavern consisted of the crown in three parts and 7 benches in three parts. Excavation work started in March 2001 and was finished in December 2003.

#### Issues during and after excavation

In 29<sup>th</sup> of May 2001, during the widening of the crown near RD 95 m, the roof between RD 120 m and RD 135 m collapsed. The collapse progressed until 2<sup>nd</sup> of June to both

---

**Table 3.8:** Rock bolt failure in the machine hall at Tala hydroelectric plant from May 2003 - June 2011. Adapted from (Naik, Sudhakar, et al., 2011). MH = Machine Hall, US = Upstream, DS = Downstream, GE = Gable End Wall

Location	Total bolts installed	Failed bolts	%
MH US	3619	147	4,06%
MH DS	2896	30	1,04%
MH RD 0 m	188	0	–
MH GE RD 206 m	530	13	2,45%

sides till it reached RD 90 m to RD 160 m. The depth of the overbreak varied from a few meters to 7 m, and was at its most on the upstream side of the cavern at 7 m, but less on the downstream side where it varied 1 - 3 m. At first, between RD 120 m - RD 135 m, the rock bolts, bearing plates and end anchors supporting the roof were intact and the material between them had fallen. In RD 135 m - RD 160 m the bolts had sheared just above the bearing plates and between RD 120 m - RD 90 m the bolts had sheared off about 3 - 4 m from the bottom and with the bearing plates intact. In a few occasions the bolts came down with the anchorage intact and all of the anchor shells had been successfully open (Report on quality control, 2006).

Similar failure happened during the excavation of the crown of the transformer hall. After simultaneous blast of the central gullet at RD 119 m and the side slashing at RD 86 m, a wedge-shaped roof fall occurred, leaving 4-5 m deep gash in the roof between RD 85 m and RD 97 m. In addition to that rock fall, sheared/crushed quartzite got detached at RD 70 m (Report on quality control, 2006).

It is apparent that the conditions in the excavation of the caverns was problematic, as expected. However, the failure of rock support system did not cease after the excavation work. After completion of the caverns rock bolts continued to fail and between late May 2003 and June 2011 total of 190 bolts had failed in the machine hall, 147 in the upstream wall, 30 in the downstream wall and 13 in the gable end wall, and total of 5 bolts in the transformer hall, all in the upstream wall. Of the 190 failed bolts, 54 of them failed after the powerplant had been commissioned in July of 2006 (Naik, Sudhakar, et al., 2011). The bolt failure in this time period is summarized in table 3.8.

Immediately after the rock fall in the machine hall cavern extensive instrumentation was carried out and to this day it is being monitored. In the final report of instrumentation and monitoring, Naik, Sudhakar, et al. (2011) listed the instruments that were still being monitored during the time the plant had been operational: load cells on steel ribs (3 pcs), anchor load cells (21 pcs), piezometers (26 pcs), instrumented bolts (8 pcs), MPBX (Multi Point Borehole eXtensometer), both mechanical (3 pcs) and magnetostrictive (1 pcs), total station targets (20 pcs) and strain gages (2 pcs). The instruments were distributed along the length and height of the machine hall and between the upstream and downstream walls and the invert.

---

The data from the instruments showed significant convergence, or maximum of 374,35 mm at RD 65 m, E 525 m in the machine hall. That was in a time period of 3037 days, and there of 26.52 mm during the operational time period. The trend shows that convergence was still going on at a steady rate, at 0,006 - 0,017 mm/day, in 2011. The total convergence decreases towards the ends of the cavern lengthwise, as well as it is lower at E 520 m at all stations. The change in load on the steel ribs during the operational period varied along the cavern length, being at the most at RD 126 m on the downstream side, where the change in load measured -4,06 tons, and at the upstream side at RD 56,5 m where it reached 3,77 tons. During this time the change shows stabilizing trend. The load change on the anchor load cells peaked at 13,85 tons at the downstream side at RD 110 m E 515 m. The pore pressure did not build up around the cavern above E 500 m, and pressure of only 0,20 - 1,50 kg/cm<sup>2</sup> could be observed below E 500 m. MPBX monitoring at RD 110 E 515 indicated deformation in the rock mass to depth of up to 15,6 m at least, where displacement was measured 10 mm, but at 21,5 m depth no displacement was observed. No measurements are available between these two points, so it is safe to assume that the extent of failure zone lies between depth of 15,6 m and 21,5 m (Naik, Sudhakar, et al., 2011).

The transformer hall cavern has been monitored in a similar way although it is not as heavily instrumented. In April 2011 the following instruments were available during the operational period until June 2011: load cells on ribs (3 pcs), load cells (6 pcs), piezometers (4 pcs) and instrumented bolts (4 pcs). During the operational period the load has changed the most around the middle of the caver, at RD 113 m, where it increased by 7,62 tons on the upstream side and decreased by 12,56 tons on the downstream side. The anchor load shells that were installed did not show significant change, only 1 - 3 tons, except for at RD 81 m E 523 m where the load increased by 6,29 tons. All piezometers show slight decrease in pore pressure (Naik, Sudhakar, et al., 2011).

After completion of benching and work had started in floor of the turbine pits, cracks in the newly laid concrete pads for the turbine foundation were observed. MPBX and measurements with total stations showed heaving of the invert, most likely as a result of the stepped invert with trenches, sumps and rock ledges between turbine pits. In such conditions the stress distribution around the cavern can appear as heaving in the invert, leading to cracking of the floor or other structures. The heaving was dealt with by extensive rock bolting and waiting for stabilization. Monitoring of the heaving showed it had stabilized after 8 - 9 months (Tripathi & Yadava, 2007).

Altogether the analyses show stabilizing trends or steady rate of change in both caverns. The ongoing convergence in the machine hall indicates that the cavern was still in stabilizing phase in year 2011. In 2011 Naik, Nair, et al. predicted that rock bolts would continue to fail, based on numerical back analysis of the powerhouse complex.

### **Rock support system**

The rock support system used in the caverns is described in Report on quality control, 2006, and Singh et al., 2002

---

The support system in the two caverns mainly consisted of rock bolts, plain and steel fibre reinforced shotcrete (SFERS) and steel ribs in the crown. The central gullet of the crown was initially supported with 32 mm diameter (dia) / 6 m long expansion shell anchored rock bolts, with 3,0 m x 1,5 m pattern, and a 100 mm thick layer of SFERS after rock bolt installation. During widening of the crown side slashings were supported with 32 mm dia / 6 m and 8 m long rock bolts at 1,5 m c/c (centre to centre) and a 75 mm - 100 mm thick SFERS layer. Following the aforementioned roof collapse, a conventional ISMB 350 steel rib system with 12 mm thick plates on the flanges at 0,6 m c/c was installed with 32 mm dia / 8 m and 10 m long rock bolts at 3 m c/c staggered pattern. The cavity between the steel ribs and the rock was backfilled with concrete and then grouted to ensure contact with the rock.

Based on site investigations after the roof collapse a support system was designed for the side walls. In the first bench, 3 layers of 50 mm thick plain shotcrete, welded wire mesh, consolidation grouting and 32 mm dia / 12 m long high strength rock bolts. The first layer of shotcrete was applied right after excavation, and 100 mm x 100 mm x 4 mm welded wire mesh installed on the shotcrete surface. Holes were drilled for grouting to the depth of 11 m and grouting began with maximum pressure of 5 kg/cm<sup>2</sup>, and after the grout had set the holes were re-drilled up to 12 m, as well as additional holes were drilled to meet the bolt spacing requirements of 1,5 m c/c. After rock bolts had been installed they were tensioned to 30 tons. The second layer of shotcrete was then applied and the third one after the second one had set. The excavation and supporting of this first bench was very slow, 159 days at the rate of 3000 m<sup>3</sup> per month. When apparent that the rock support was sufficient in the first bench, the dimensions of the niches in subsequent benches were increased, increasing the rate of excavation to 12700 m<sup>3</sup> per month. The rock bolts were the same type and kept at 12 m length but the diameter was decreased from 32 mm to 26,5 mm and the tension decreased from 30 tons to 12 tons.

Thorough testing and research was conducted in order to determine the right material for support. Right from the start of the excavation work bolts were shearing and failing so it was apparent that high strength rock bolts were needed. Mainly two types of bolts were discussed and tested; the Tor steel rock bolt and Dywidag rock bolts. One row of Tor steel rock bolts was installed beneath the rib beam in the machine hall. Pull out tests were conducted on random bolts in that row and most of the bolts tested in the showed high displacement, up to over 40 mm at 32 - 37 tons load. These high displacement values could be explained with various reasons; the 200 mm x 200 mm x 20 mm faceplate not being perpendicular to the rock surface thus bending the bolt at the weaker thread portion, disturbance in rock mass due to blasting and displacement in couplings where two bolts needed to be combined to reach the desired length, to name a few. Similar tests were done on the Dywidag rock bolts. The results showed less displacement of the bolts, or maximum of 17 mm at 39,8 tons load. The results of the pull out tests of Tor steel rock bolts and Dywidag rock bolts can be seen in tables 3.10 and 3.11 respectively and data from the tables is plotted as load versus displacement in figure 3.7.



**Table 3.9:** Properties of Dywidag rock bolts used in the support system, as given from the manufacturer (Singh et al., 2002)

<b>Chemical properties</b>	: C = 0,69%, Sr = 0,23%, Mn = 0,65%, P = 0,013%, S = 0,010%
<b>Physical properties</b>	: Yield strength = 1033 N/mm <sup>2</sup> (571 kN for 26,5 mm dia bolts) Tensile strength = 1122 N/mm <sup>2</sup> (620 kN for 25,6 mm dia bolts) % elongation = 8% % reduction in area of rupture = 19 - 20%

**Table 3.10:** Results from pull out tests on the Tor steel rock bolts (Singh et al., 2002)

Sl. No.	Location	RD m	EL m	Rock Type	Installation Date	Testing Age Days	Applied Load Tons	Displacement mm
1.	U/S Wall	171.75	531.5	III	25-5-02	2	32	19.10
2.	U/S Wall	172.50	530.0	III	25-5-02	2	28	31.80
3.	U/S Wall	57.00	530.0	III	1-6-02	1 Hr.	27 37	16 33, Breakage at thread
4.	U/S Wall	58.50	530	III	1-6-02	1 Hr.	27 34.5	20.00 33, Breakage at thread
5.	U/S Wall	57.00	530	III	1-6-02		34	35
6.	D/S Wall	128.5	528.5	IV	1-6-02	1 Hr.	7	88, Failed
7.	Gabble End	206.4	530	III	19-5-02	5	30	4.40
8.	Gabble End	206.4	530	III	19-5-02	5	32	41.20

As the Dywidag rock bolt showed higher load capacity, partly due to stronger, continuous bar threads giving better anchoring in the resin and the grout along the whole length of the bolt, than the Tor steel rock bolt it was decided to use them in further support systems in the project. Due to shortage of 12 m long Dywidag bolt 8 m and 4 m long bolts were coupled together. Three of them were tested for tensile strength and results from that showed no difference from the whole ones. The properties, according to the manufacturer can be seen in table 3.9. The tensile strength obtained in test of three 32 mm dia bolts showed strength varying from 1116,8 MPa to 1128,3 MPa and average of 1122,6 MPa, which corresponds to load of about 90 tons. The steel strength specification was 835 / 1030 MPa with yield load of 67,1 tons and ultimate load of 82,3 tons.

The bolts in the side walls were resin anchored with length up to 4,2 m and grouted after the 2 200 mm long dry cement capsules had been inserted to act as a barrier between the resin and the grout. Samples resin and cement capsules were tested upon arrival of each new batch. The resin was approved if the compressive strength of the resin exceeded 60 MPa 1 hour after mixing and the cement capsules if they exceeded compressive strength of 16 MPa after 24 hours and 24 MPa after 72 hours (Singh et al., 2002).

**Table 3.11:** Results from pull out tests on the Dywidag rock bolts (Singh et al., 2002)

Sl. No.	Location	RD m	EL m	Rock Type 'Q'	Installation Date	Testing Age Days	Applied Load Tons	Displacement mm
1.	U/S Wall	120	528.75	III	2.7.2002	8	30	3.5
2.	U/S Wall	162.5	528.75	III	14.7.2002	19	39.8	17.0
3.	U/S Wall	187.5	531.75	III	23.7.2003	10	39.8	5.5
4.	U/S Wall	92.25	528.5	III	24.7.2002	9	39.8	6.0
5.	U/S Wall	60.75	528.75	III	4.7.2002	29	39.8	9.0
6.	U/S Wall	43.5	530.25	III	25.7.2002	8	39.8	6.0
7.	D/S Wall	126.6	528.75	IV	25.6.2002	15	30	5.0
8.	D/S Wall	186.75	530.25	III	1.8.2002	1	39.8	8.5
9.	D/S Wall	183	528.75	III	1.8.2002	1	39.8	2.5
10.	D/S Wall	51.75	531.75	III	1.8.2002	28	39.8	8.0
11.	D/S Wall	176.75	530.25	III	12.8.2002	1	38.4	11.8
12.	D/S Wall	145.5	525.75	III	16.9.2002	15	38.4	4.0
13.	D/S Wall	166.5	525.75	III	22.9.2002	9	38.4	10.0
14.	D/S Wall	133.5	525.75	IV	22.9.2002	9	38.4	15.0

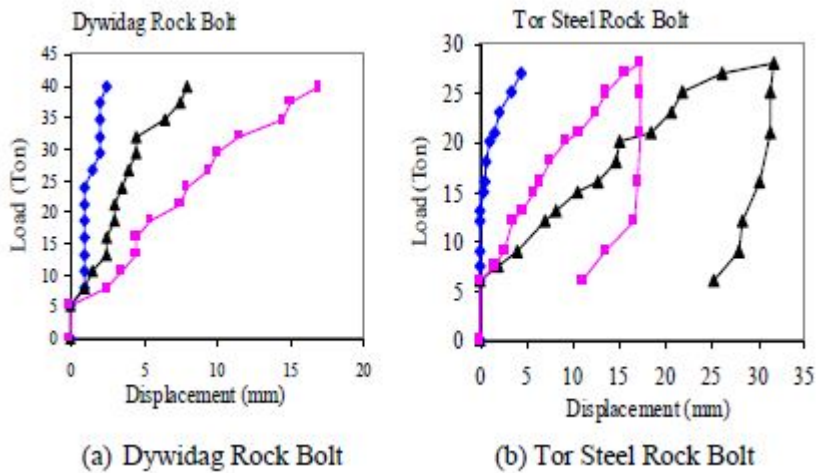


**Figure 3.7:** Load vs. displacement comparison between pull out tests of 32mm dia / 12 m long Tor steel rock bolts and Dywidag rock bolts (Singh et al., 2002)

---

## 3.3 The Chhukha Hydropower Project

In this thesis, another nearby hydropower plant, the Chhukha hydroelectric plant, is used for comparison. 3D BEM model will be presented and the stability of its machine hall cavern analysed in chapter 4.

### 3.3.1 In General

The Chhukha hydroelectric powerplant was the first large scale hydroelectric power project in Bhutan and fully funded by the government of India, 60% as a grant and 40% as loan payable after commission. It is a run-of-the -river scheme in the Wang Chhu river basin with its outrun only 3 km upstream of the Tala dam. Geological exploration for this mainly underground project started in April 1963 and construction on surface infrastructure, roads, buildings in the vicinity, started in the year 1973. Building of the dam and excavation of underground structures commenced in 1978 - 1979. The first unit of 4 was commissioned in September 1986, and the 3 remaining were commissioned in August 1988, combining the total capacity of 336 MW utilizing 4 84 MW turbines units. The powerplant incorporates a 40 m high gravity diversion dam, diverting the Wang Chhu river into a set of desilting chambers before going into the 6513 m long headrace tunnel. The headrace tunnel ends in the pressure shaft complex, which consists of bypass to the surge shaft and two 528 m long pressure shafts. The pressure shafts lead to the underground powerhouse, cumulating gross head of 468 m. The powerhouse is 141,25 m x 24,5 m x 37,5 m (LxWxH), and has overburden of about 230 m. From the powerhouse the water is lead through the 976 m long tailrace tunnel back to the river basin. The main features of the project are summarized in table 3.12 and figure 3.8 shows the layout of the infrastructure.

**Table 3.12:** The main features of the Chhukha Hydroelectric Project

### Chhukha Hydroelectric Project

Location	: 27,08°N, 89,56° E
Installed capacity	: 4 x 84 MW
Dam	: 40 m high concrete gravity dam
Intake level	: 1342.5 masl
Desilting Chambers	: 2 x 347,5 m x 8,5 m x 16,65 - 19,06 m (LxWxH)
Headrace tunnel	: 6513 m
<b>Power House</b>	
Machine hall	: 141,25 m x 24,5 m 37,5 m (LxWxH)
Machine hall long axis	: N40°W - S40 °
Floor level	: 1384,65 masl
Main access tunnel	: D-shaped, 402 m x 8 m x 6 m (LxWxH)
Tailrace tunnel	: 975,94 m x 7 m x 4,5 m (LxWxH)

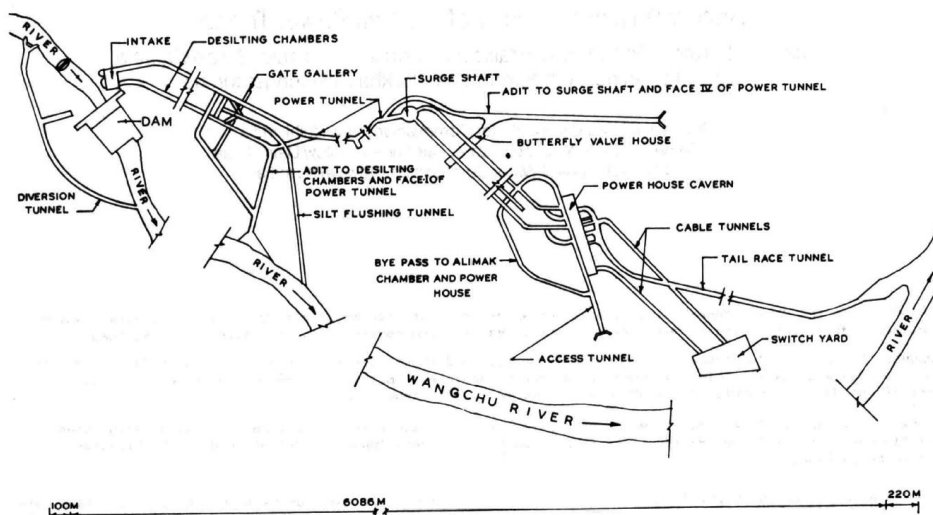


Figure 3.8: Layout of the Chukha hydroelectric infrastructure (Madhavan et al., 1987)

### 3.3.2 Geology

The powerhouse cavern is located about 400 m inside the valley side with overburden of about 240 m. The host rock consists of granitic gneiss with minor bands of profile schist and occasional shear zones of thickness varying from 5 - 50 cm. The strike of foliation in the gneiss surrounding the cavern was measured from N30°W - S30°E to N40°W - S40°E, and the average strike of foliation in the cavern N35°W - S35°E and dipping 20° to N55°E (Char et al., 1988). The dominant joint sets were recorded and can be seen in table 3.13 and figure 3.9.

Table 3.13: The recorded joint sets in rock mass surrounding Chukha machine hall (Char et al., 1988)

No.	Strike	Dip	Comments
1	N40°E - S40°W	80° : N30°W	Mostly clean, occasional 1 - 2 cm gauge. Continuity more than 5m.
2	N30°E - S15°W	60° : N60°W	Mostly clean, occasional 1 - 2 cm gauge. Continuity more than 5m.
3	N15°E - S15°W	75° : S75°E	Mostly clean, occasional 1 - 2 cm gauge. Continuity more than 5m.
3	N15°W - S15°W	75° : N75°W	Mostly clean, occasional 1 - 2 cm gauge. Continuity more than 5m.
4	N10°E - S10°W	60° : S80°E	Mostly clean. Continuity more than 5m.
5	N25°W - S35°E	20° : N55°E	Foliation, 0,5 - 1 m. Apart shearing along these planes varies from 5 - 50 cm.

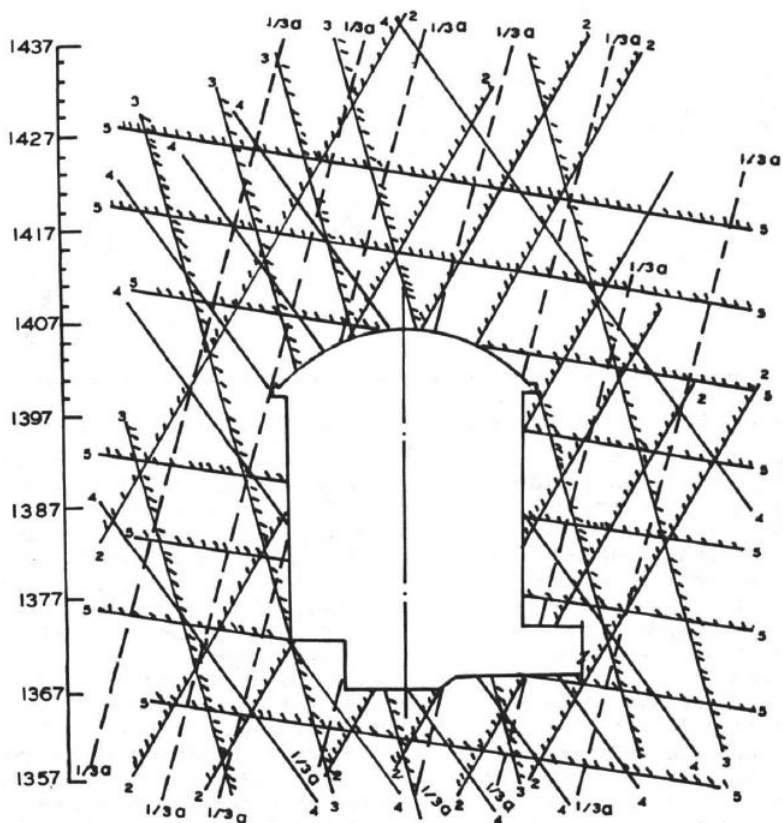


**Figure 3.9:** Cross section of the Chhukha machine hall with the dominant joint sets (Char et al., 1988)

### Rock Mass Properties

The main properties of the rock mass were measured in a exploration drift in the access tunnel near the powerhouse cavern. The Central Soil and Materials Research Station (CSRMS) conducted Goodman jack, flat jack and plate jack tests in drift, both parallel and perpendicular to the cavern orientation. The rock mass was graded as "good" according to the RMR system (*Chukha Hydel Project, Bhutan, 1984*) and mechanical properties of it obtained, and are listed table 3.14 (Char et al., 1988).

### In-situ Stress Field

The magnitude of the vertical stress and primary horizontal stress were obtained in the same drift, and is presented in table 3.15.

---

**Table 3.14:** Rock mass properties in host rock of Chhukha powerhouse cavern (Char et al., 1988)

Properties	Value	S.I. Value
Poisson's ratio	0,18	0,18
Modulus of deformation	$5 \times 10^4 \text{ kg/cm}^2$	4,9 MPa
Young's modulus	$6 \times 10^4 \text{ kg/cm}^2$	5,88 MPa

**Table 3.15:** In situ stress around Chhukha powerhouse cavern (Char et al., 1988)

Stress	Value	S.I. Value
Vertical stress	$17,5 \text{ kg/cm}^2$	1,716 MPa
Horizontal stress	$3,9 \text{ kg/cm}^2$	0,383 MPa

### 3.3.3 The Construction Phase

Excavation work of the project started in the late 70's. Complex geological setting in the Himalayan mountains greatly affected the construction; landslides near the dam, large scale water flow in in the headrace tunnel and rockfalls in the headrace tunnel and the powerhouse cavern delayed completion. The focus here is on the excavation of the powerhouse and measures taken upon complications.

#### Excavation and rock support

The excavation was driven by conventional drill and blast method, and was at the time one of the largest of its kind. The cavern was excavated in stages, starting from 3 tunnels in the cavity area:

- 5 m x 5 m ramping-up tunnel from service bay area at the end of the access tunnel, towards the spring level of the cavity.
- 5 m x 5 m ramping-down tunnel from the service bay area at the end of the access tunnel, towards the base of the cavity.
- Horizontal 4,5 m x 4,5 m tunnel in between the two ramping tunnels at the access tunnel level, towards the end of the cavity.

The cavity was extended from these three tunnels by excavation in generally 4 m deep increments. Rock support was added immediately, in the form of row of 9 m and 4 m long grouted anchored rock bolts, with 4 m and 2 m c/c respectively. Wire mesh reinforced shotcrete was eventually applied. In some places 13 m and 10 m long rock bolts were installed (Char et al., 1988), and the general layout of bolting can be seen in figure 3.10.

#### Issues during excavation

Intersecting joints, shown in figure 3.9, generate unstable wedge formation, especially in the downstream wall, whereas the orientation is more favourable in the upstream wall. Maximum size of potentially unstable block was estimated 2 m x 2 m x 3 m and the largest ones were found in the junction between the roof arch and the downstream wall. Those

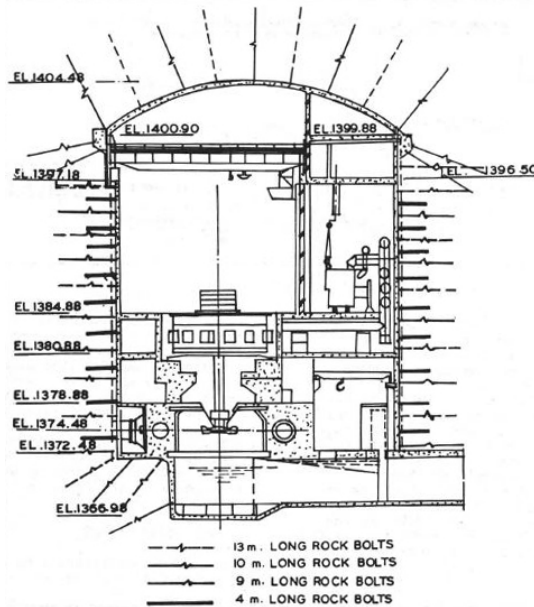


**Figure 3.10:** The profile of the Chhukha powerhouse cavern, showing layout of rock support and elevation markers (Char et al., 1988)

were met by two rows of pre-tensioned 13 m and 9 m long grouted rock bolts.

At RD 90 m to 104 m large rock fall in the crown resulted in 6 fatalities and dome formation. Joint forces of shear zones, 5 cm - 50 cm thick, and high in-situ vertical stress conditions allowed for deep block to become loose and fall. The roof was supported with closely spaced steel ribs and 10 m long rock bolts at 3 m c/c (Char et al., 1988).

### 3.4 Comparison between Tala and Chhukha

Regardless of the close proximity to one another, the two excavations of Tala and Chhukha differ highly in regards to stability. As earlier addressed, the deformation of the Tala powerhouse complex is ongoing, where rock bolts have been failing long after excavation, while no records are of stability problems in Chhukha powerhouse cavern (however data from Chhukha is limited as no instrumentation data is accessible). Both projects experienced complications during construction in form of rock fall in the roof, leading to delays and increased rock support.

The scale of the Chhukha powerhouse excavation is significantly smaller than the Tala one, where the Chhukha project consists of only one large cavern, whereas Tala complex consists of the two large caverns and the bus ducts connecting them. Other cavities in Tala, like tailrace tunnels, headrace tunnels and drainage galleries, are also on whole an-

---

other level than their counterparts at Chhukha, as can be seen in figures 3.4 and 3.8.

Neither Tala nor Chhukha excavations are oriented optimally, with regards to joint orientation in the area as can be seen in tables 3.2 and 3.13. In both instances joints are dipping toward each other, generating potentially unstable wedge formation. However both caverns are well aligned with regards to foliation, where they are both near perpendicular to the strike of the foliation. The joints at Tala seem to be generally more filled with clay gouge, while the joints at Chhukha seem to be mostly clean.

The rock mass hosting the projects is of two different formations. The rock at Tala powerhouse complex are of the Shumar formation of the LHS, phyllite, phyllitic quartzite, quartzite and amphibolite. The medium the Chhukha powerhouse cavern lies in is made up of granitic gneiss, with bands of schist of the Paro formation. It is apparent from the lithology and the rock mass properties reviewed in chapters 3.2.2 and 3.3.2 that the rock mass is more favourable in the Chhukha project.

The Tala powerhouse complex lies closer to the MCT, leading to higher horizontal stresses than at Chhukha. The maximum horizontal principal stress at Tala was measured to be 1,31 times the vertical stress, or 14,205 MPa, based on average overburden of 410 m. That is nearly along the cavern's long axis. Near-perpendicular to the long axis the K value was measured 0,87, which results in 9,43 MPa when using same overburden. When compared to the in-situ stress field at Chhukha it is apparent that the Tala powerhouse complex lies in much less favourable stress environment. The average overburden at Chhukha is at 240 m and the vertical stress was measured to be 1,72 MPa, but only one value value has been obtained for the horizontal stress, so the assumption that the two horizontal principal stresses are equal at 0,38 MPa.

All in all it is evident that the overall circumstances are more favourable for excavation at Chhukha. However it is necessary to mention that the data on the Chhukha is lacking compared to Tala. On the other hand, the excavation of powerhouse complex at Tala took place around 25 years later than the one at Chhukha, making it possible to utilize more recent techniques and more developed methods, for instance greater computational power and technology.



# Numerical Analyses

## 4.1 In General

The powerhouse complex at Tala and the powerhouse cavern at Chukha were modelled in the modelling software described in chapter 2.1.4. First, models of both projects are constructed using the input parameters obtained from the literature and described in chapters 3.2 and 3.3, both in 2D and 3D. The models are compared as they both are based on the same modelling method, as well as their stability is reviewed. The Tala powerhouse complex is modelled in Phase<sup>2</sup> with literature parameters and comparison made between the plastic FEM model and the elastic 3D BEM model. At last the Tala powerhouse complex is modelled in Examine<sup>3D</sup>, where input parameters were iterated in Phase<sup>2</sup> to resemble the actual occurrence, in regards to convergence that was measured at maximum of 374 mm in the machine hall.

## 4.2 Input parameters

The geometry used in the models are the ones listed in chapters 3.2 and 3.3 and in figures 3.5 and 3.9, although simplified as minor irregularities in the profiles are not likely to affect the overall outcome of the analyses. In the first part of the analyses the literature parameters reviewed in chapters 3.2 and 3.3 were used and are summarized in table 4.1. The failure criterion constants are gathered from Rocscience's RocData software and disturbance factor D estimated as 0,5 as the excavation method was drill and blast, so damage in the rock surrounding the opening is expected.

The field stress is modelled as constant, with the values reviewed in chapter 3.2.2. The input on the format required for Examine<sup>3D</sup> is summarized in table 4.2.

**Table 4.1:** Input parameters for numerical analyses, obtained from literature. The Hoek-Brown constants were calculated using Rocscience's RocData software.

Parameter	Tala	Chhukha
Young's Modulus [MPa]	7950	5880
Poisson's Ratio	0,355	0,18
UCS [MPa]	55	75
GSI	50	65
D	0,5	0,5
$m_b$	0,416	5,289
s	0,0013	0,0094
a	0,506	0,502

**Table 4.2:** The input parameters for the in-situ stress field at Tala and Chhukha. The orientation is controlled by direction counted clockwise in degrees from north in the model coordinate system and dip in degrees form horizontal.

<b>Tala</b>		
Stress component	Magnitude [MPa]	Dir./Dip [°]
$\sigma_1$	14,205	0/0
$\sigma_2$	10,850	0/90
$\sigma_3$	9,427	90/0
<b>Chhukha</b>		
$\sigma_1$	1,716	0/90
$\sigma_2$	0,383	0/0
$\sigma_3$	0,383	90/0

**Table 4.3:** Modelling parameters used in Examine<sup>3D</sup>

Parameter	Tala	Chhukha
Elements	33788	8734
Nodes	16892	4369
Element type	Linear	Linear
Solver type	GMRES	GMRES
Surface area	$6,17 \times 10^4 \text{ m}^2$	$1,82 \times 10^4 \text{ m}^2$
Volume	$2,94 \times 10^5 \text{ m}^3$	$1,18 \times 10^5 \text{ m}^3$
Average element size	$1,83 \text{ m}^2$	$2,08 \text{ m}^2$
External boundaries	50 m outside extreme points of excavation	50 m outside extreme points of excavation

---

**Table 4.4:** Modelling parameters used in Phase<sup>2</sup> and Examine<sup>2D</sup>

Parameter	Phase <sup>2</sup>	Examine <sup>2d</sup>
Analysis type	Plane strain	Plane Strain
Solver type	Gaussian Elimination	Gaussian Elimination
Elements	3196	493
Nodes	1758	na
Element type	3 noded triangles	Constant

### 4.3 Analyses and results

The plots produced by the modelling software are presented in the following sections. The plots are taken from cross sections at four places in the geometry, as shown in figure 4.1. Each version of the model will be analysed based on  $\sigma_1$ ,  $\sigma_3$ , strength factor (SF) and displacement. Additionally, plots showing yielded elements are presented from the Phase<sup>2</sup> models. More plots can be seen in Appendix B and the complete set will be available in digital format in full resolution.

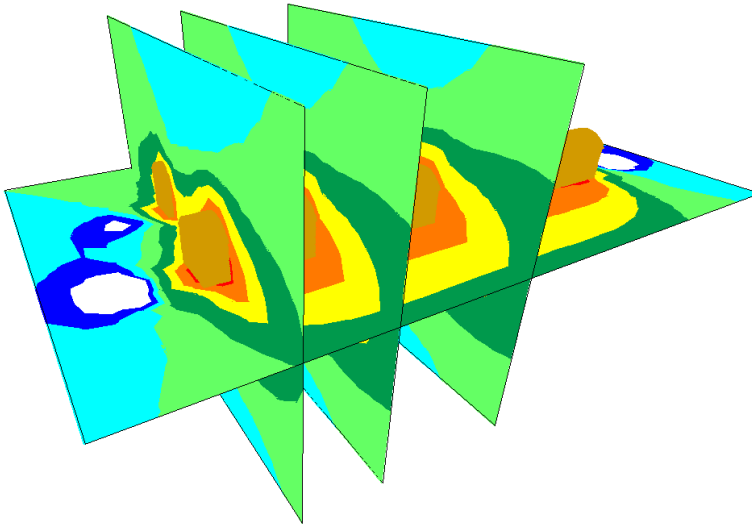


**Figure 4.1:** The cutting planes in the model of Tala powerhouse complex. RD 103 m at the middle of the complex lengthwise, RD 44,5 m equal to the height of the machine hall RD 10 m where the end effect can be observed in both caverns. EL 515 m is in the middle of the machine hall height-wise

---

### 4.3.1 Examine<sup>3D</sup>, literature values

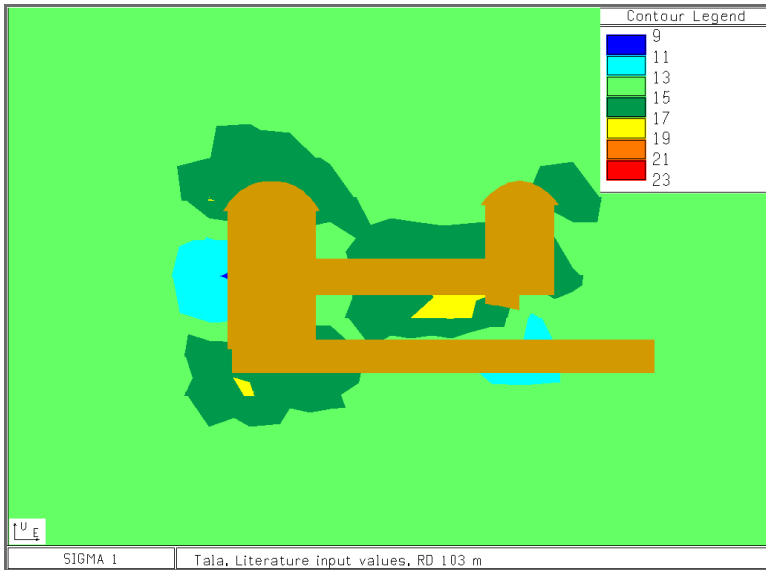


**Figure 4.2:** RD 103 m at Tala powerhouse complex, depicting contours of equal  $\sigma_1$ , using literature input values

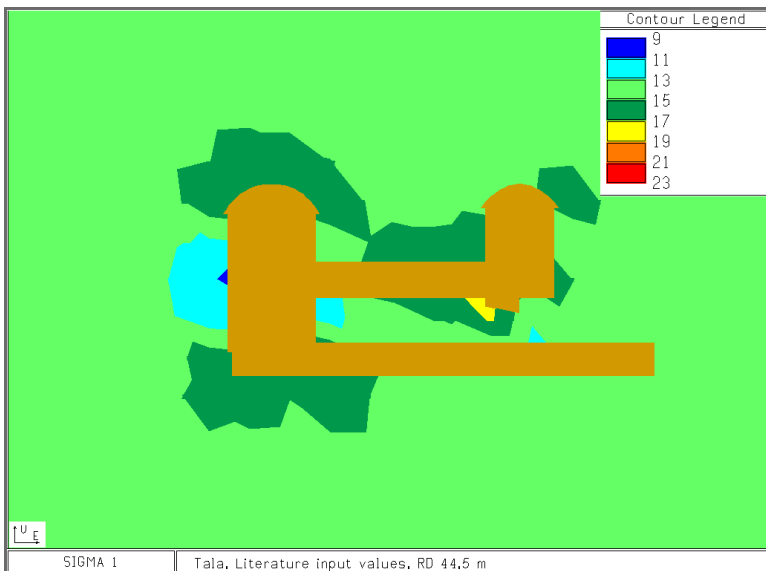


**Figure 4.3:** RD 44,5 m at Tala powerhouse complex, depicting contours of equal  $\sigma_1$ , using literature input values

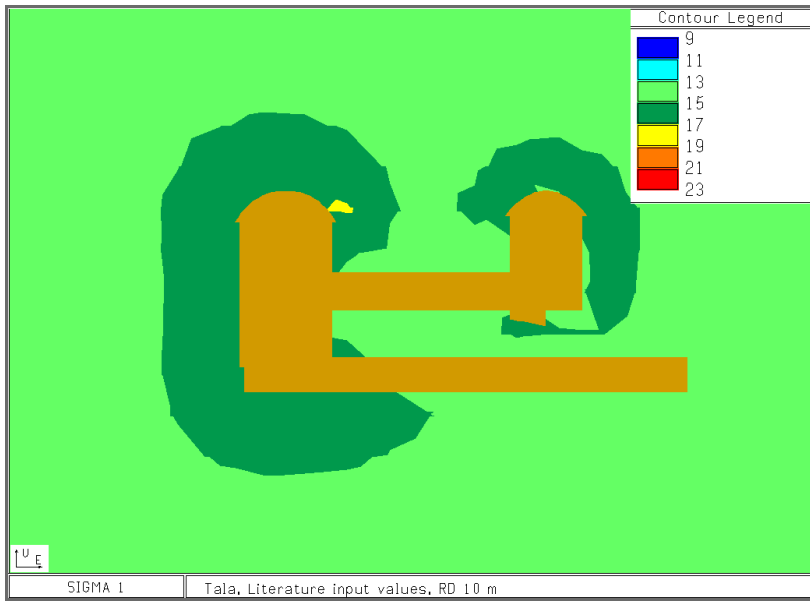


**Figure 4.4:** RD 10 m at Tala powerhouse complex, depicting contours of equal  $\sigma_1$ , using literature input values

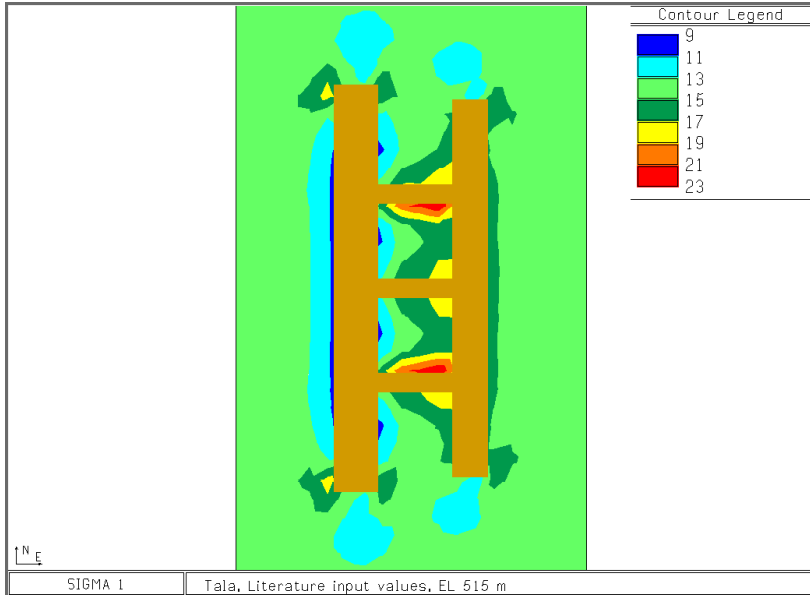


**Figure 4.5:** EL 515 m at Tala powerhouse complex, depicting contours of equal  $\sigma_1$ , using literature input values

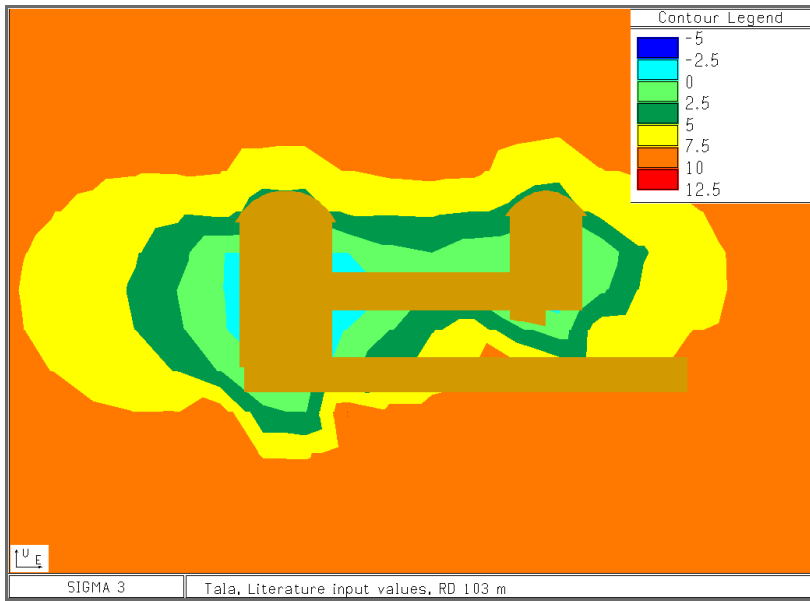


**Figure 4.6:** RD 103 m at Tala powerhouse complex, depicting contours of equal  $\sigma_3$ , using literature input values

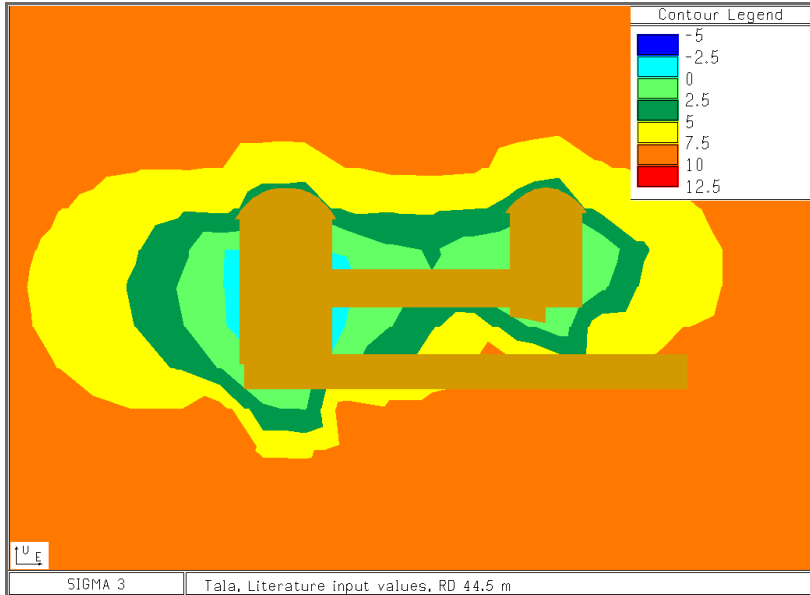


**Figure 4.7:** RD 44,5 m at Tala powerhouse complex, depicting contours of equal  $\sigma_3$ , using literature input values

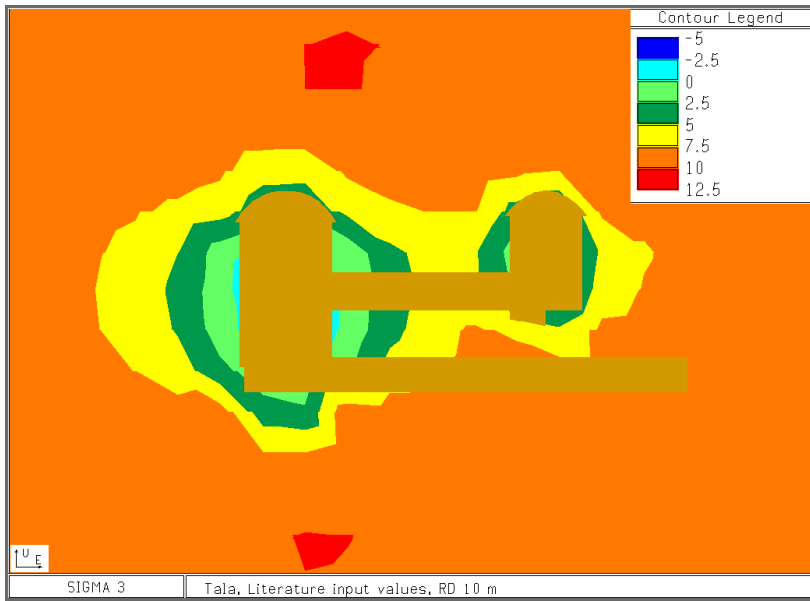


**Figure 4.8:** RD 10 m at Tala powerhouse complex, depicting contours of equal  $\sigma_3$ , using literature input values

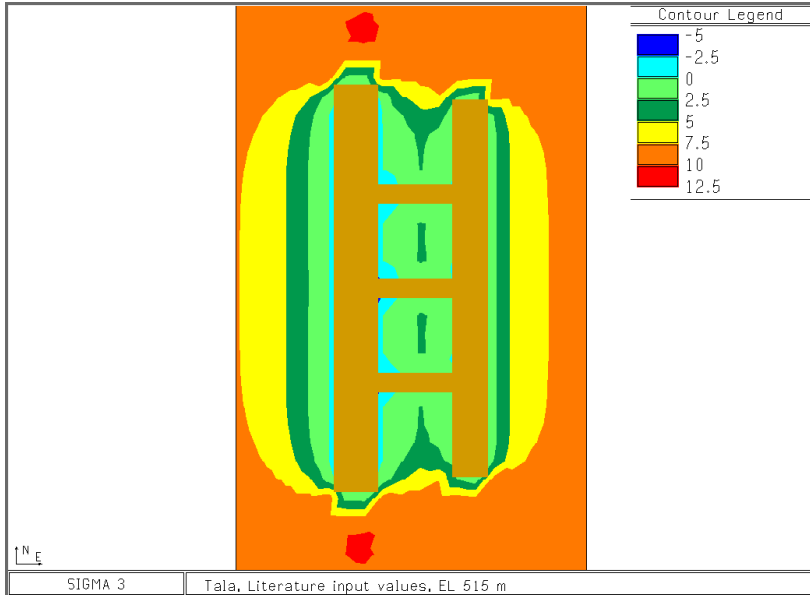


**Figure 4.9:** EL 515 m at Tala powerhouse complex, depicting contours of equal  $\sigma_3$ , using literature input values

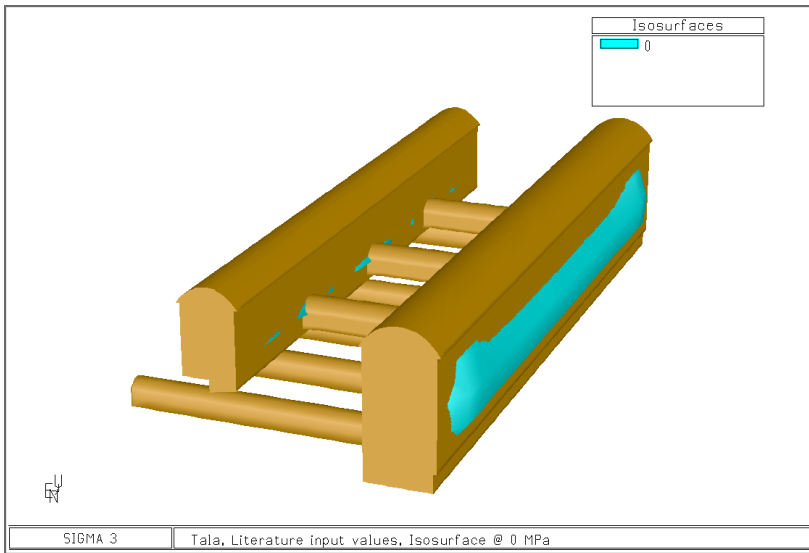


**Figure 4.10:** Perspective of the Tala powerhouse complex, depicting isosurface at  $\sigma_3 = 0$ , using literature input values

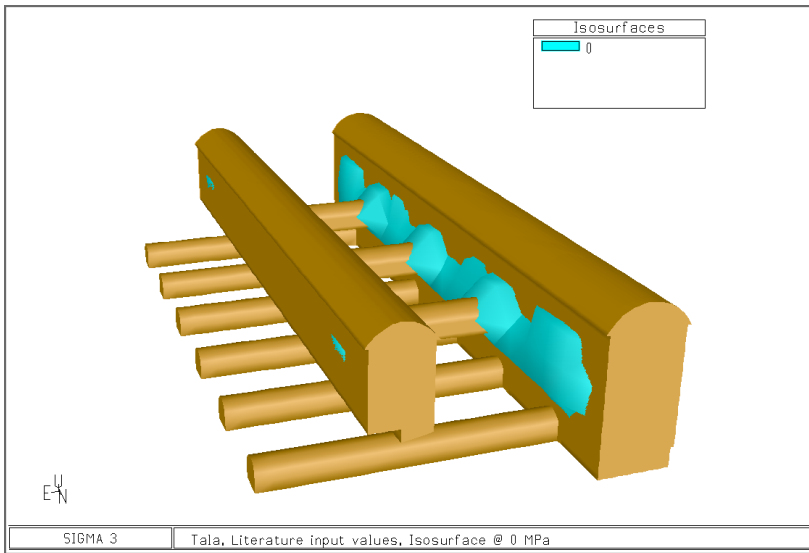


**Figure 4.11:** Perspective of the Tala powerhouse complex, depicting isosurface at  $\sigma_3 = 0$ , using literature input values



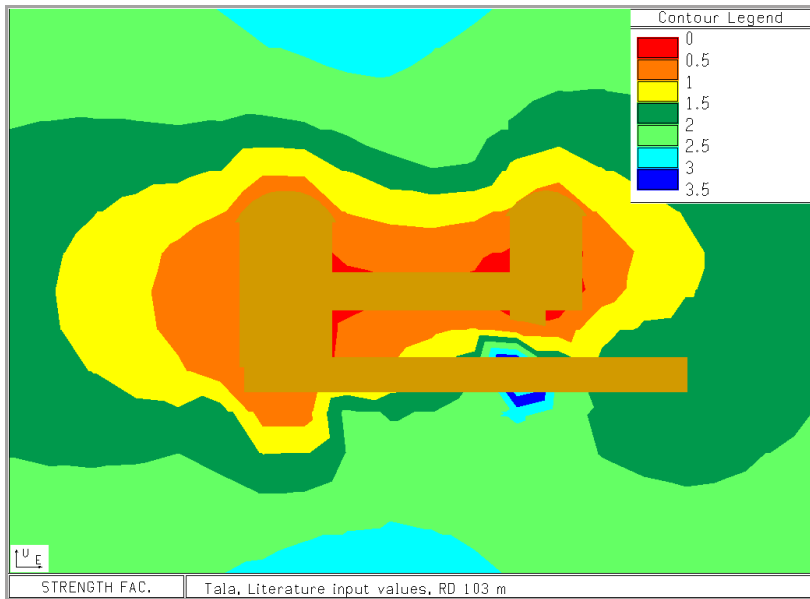


**Figure 4.12:** RD 103 m at Tala powerhouse complex, depicting contours of equal strength factor, using literature input values

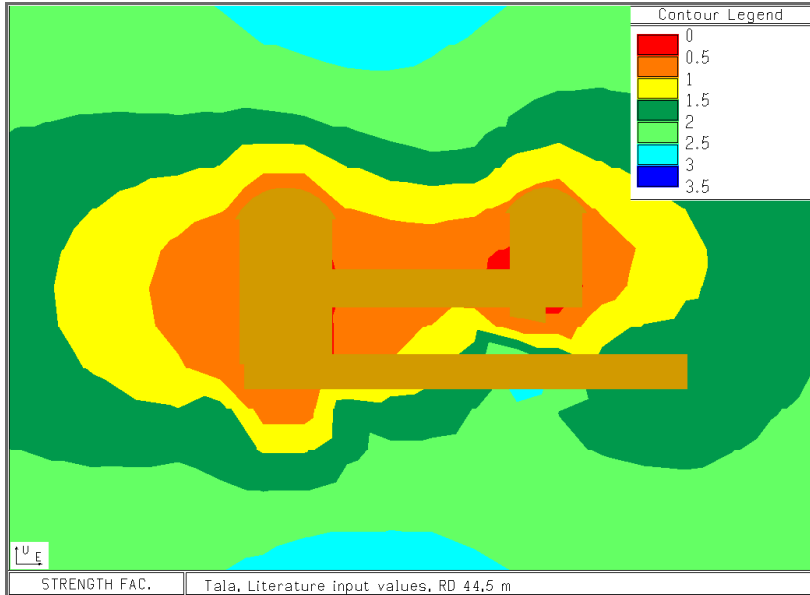


**Figure 4.13:** RD 44,5 m at Tala powerhouse complex, depicting contours of equal strength factor, using literature input values

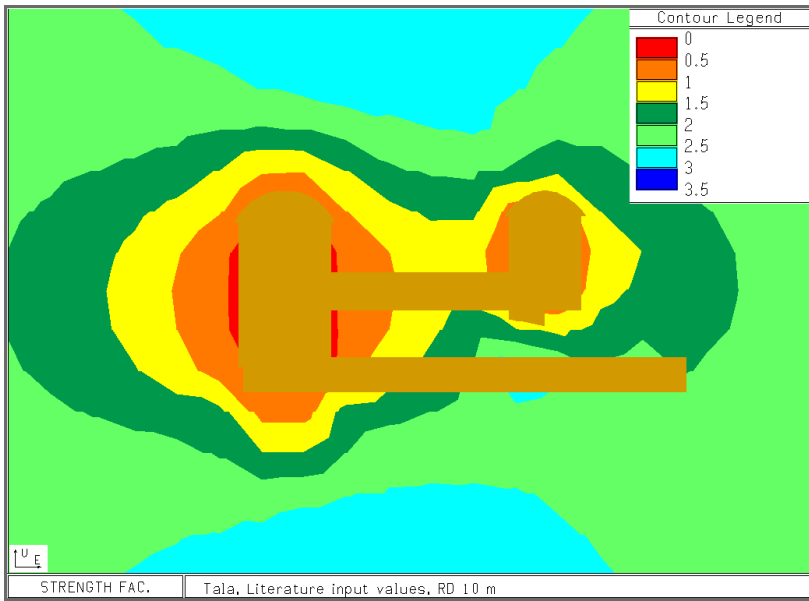


**Figure 4.14:** RD 10 m at Tala powerhouse complex, depicting contours of equal strength factor, using literature input values

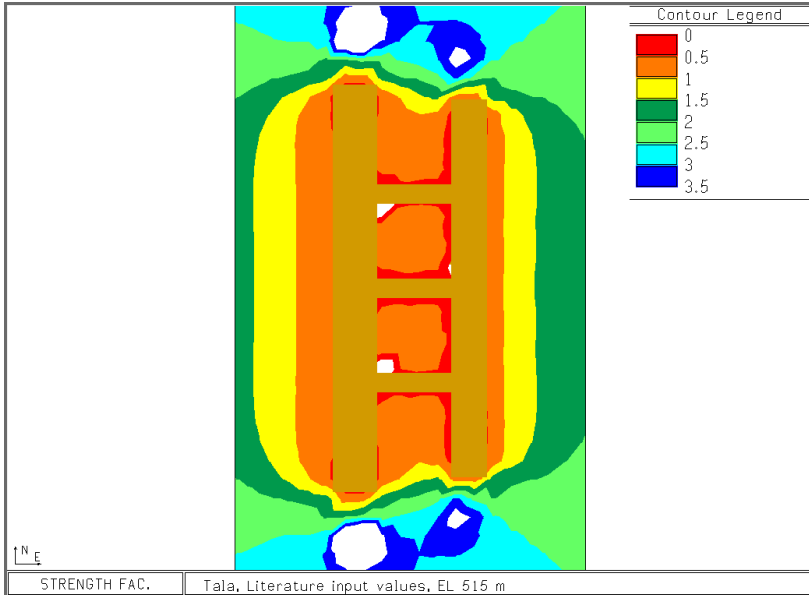


**Figure 4.15:** EL 515 m at Tala powerhouse complex, depicting contours of equal strength factor, using literature input values

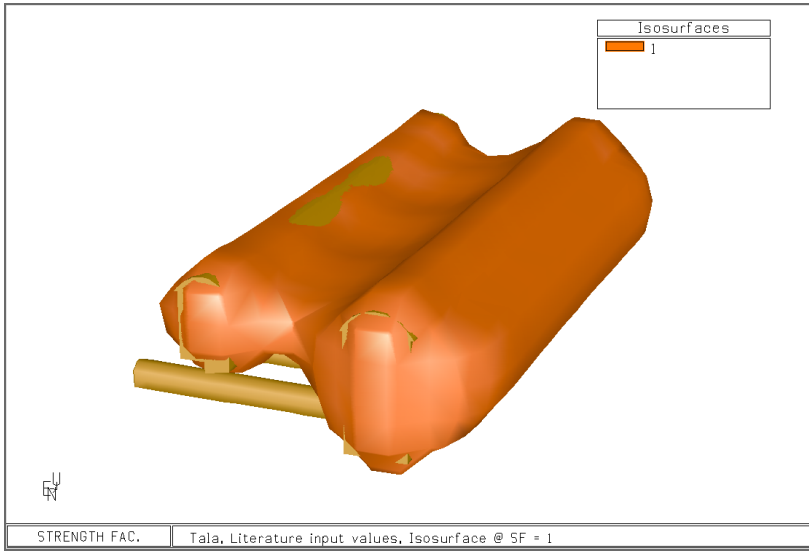


**Figure 4.16:** Perspective of the Tala powerhouse complex, depicting isosurface at strength factor = 1, using literature input values

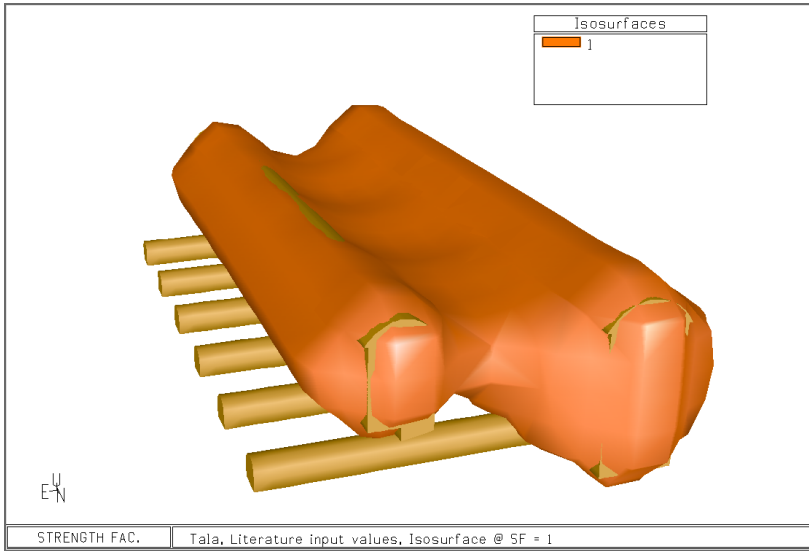


**Figure 4.17:** Perspective of the Tala powerhouse complex, depicting isosurface at strength factor = 1, using literature input values

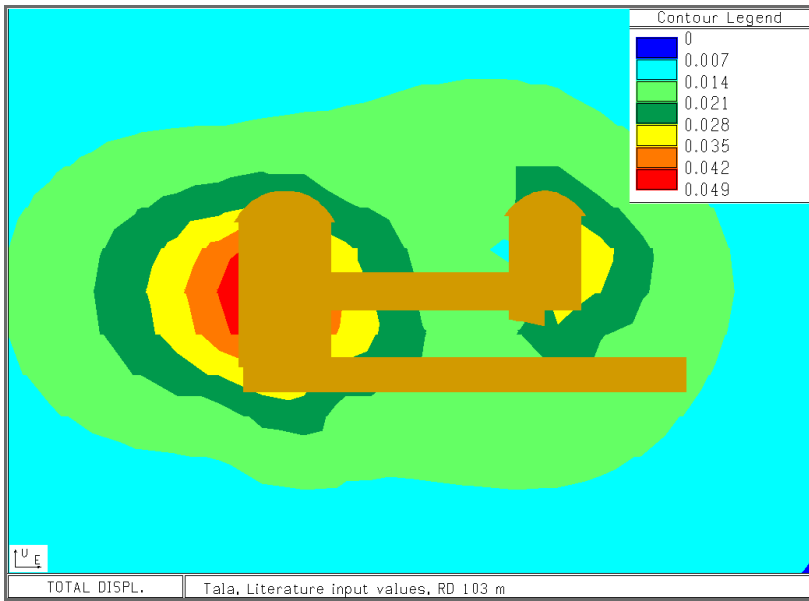


**Figure 4.18:** RD 103 m at Tala powerhouse complex, depicting contours of equal total displacement, using literature input values

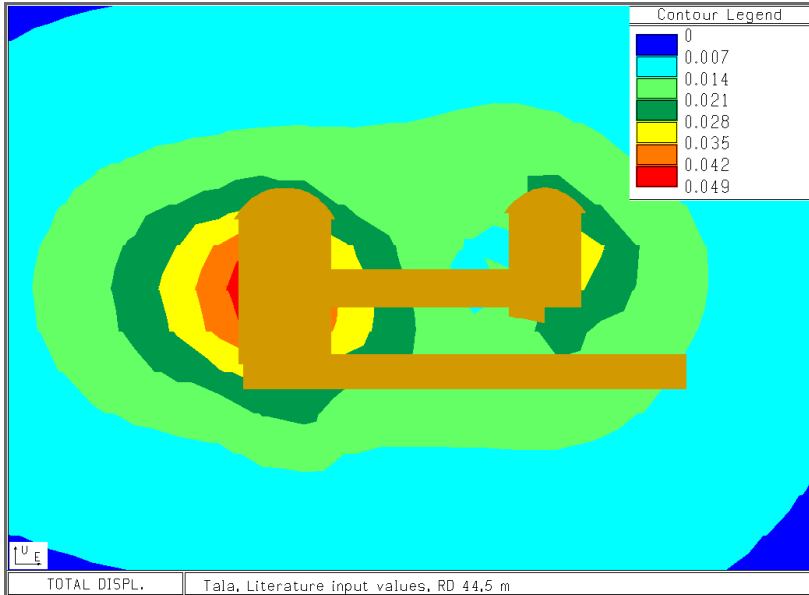


**Figure 4.19:** RD 44,5 m at Tala powerhouse complex, depicting contours of equal total displacement, using literature input values

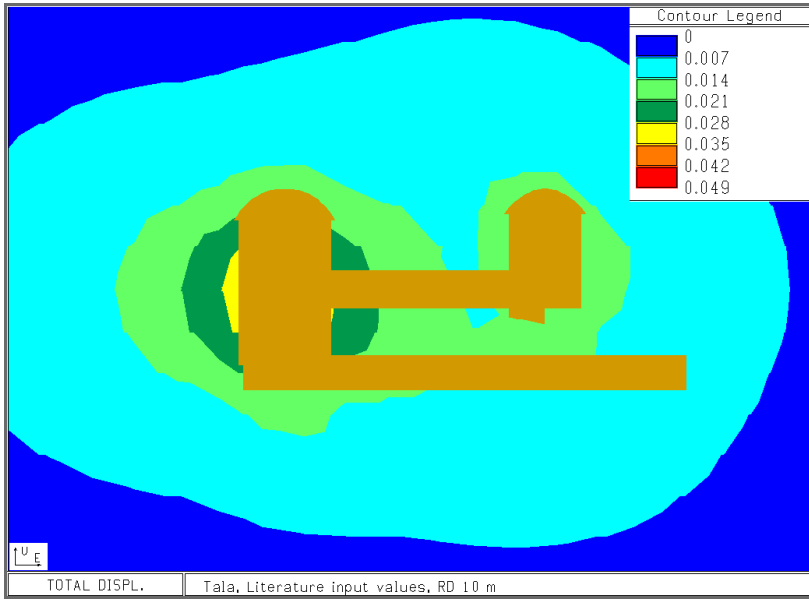


**Figure 4.20:** RD 10 m at Tala powerhouse complex, depicting contours of equal total displacement, using literature input values

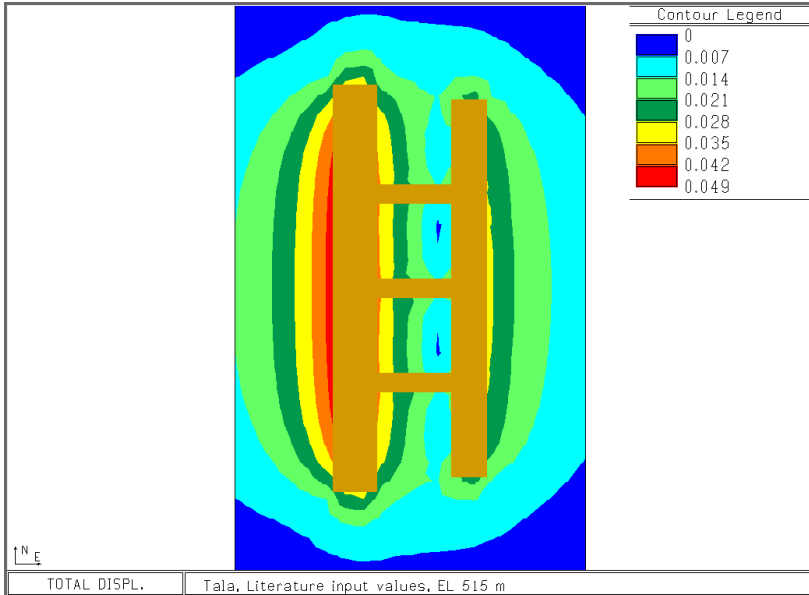


**Figure 4.21:** EL 515 m at Tala powerhouse complex, depicting contours of equal total displacement, using literature input values

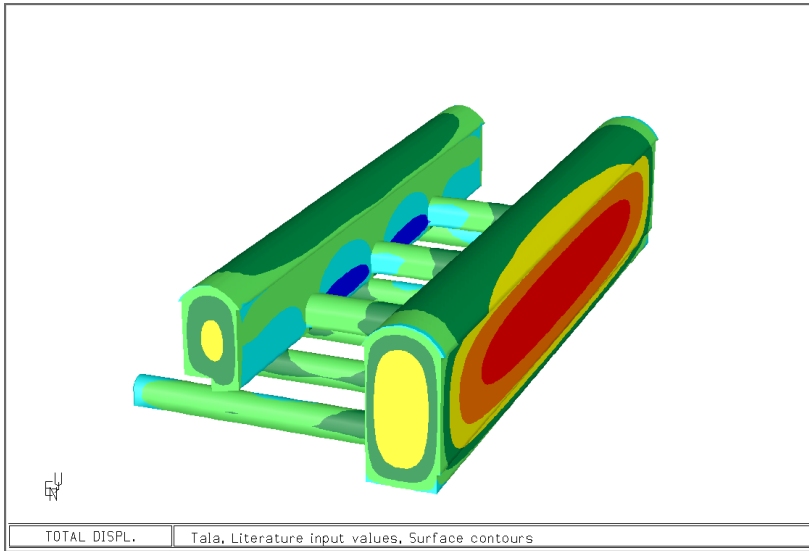


**Figure 4.22:** Perspective of the Tala powerhouse complex depicting the total displacement as it appears on the surface of excavation, using literature input values

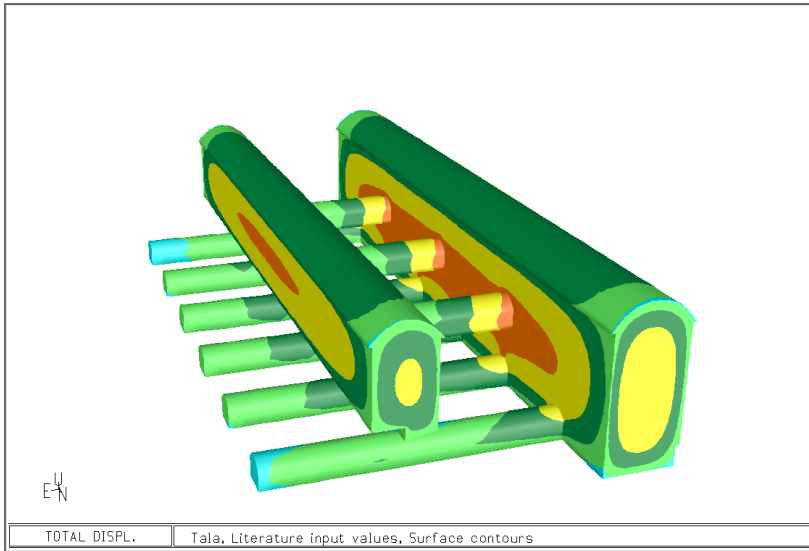


**Figure 4.23:** Perspective of the Tala powerhouse complex depicting the total displacement as it appears on the surface of excavation, using literature input values

### 4.3.2 Examine<sup>2D</sup>, literature values

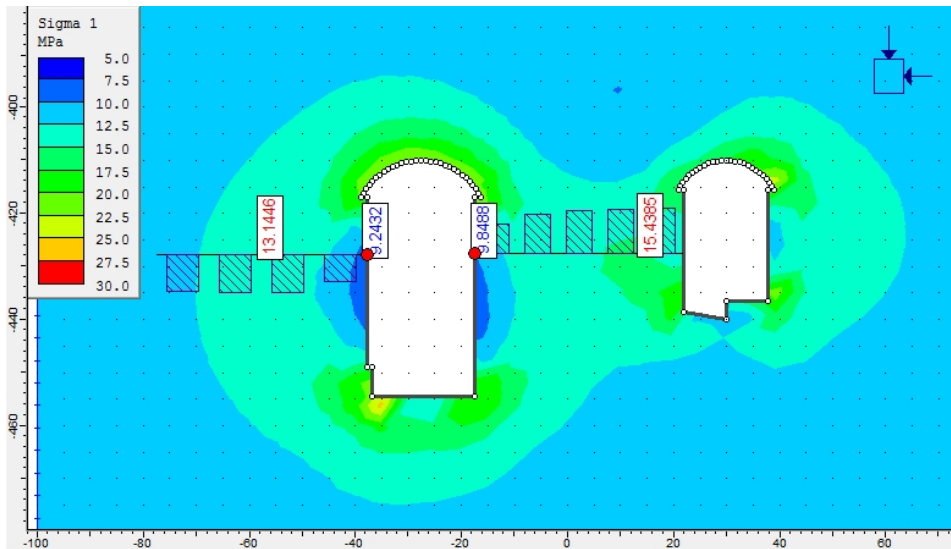


**Figure 4.24:** Examine<sup>2D</sup> model of the Tala powerhouse complex, depicting contours of equal  $\sigma_1$ , using literature input values

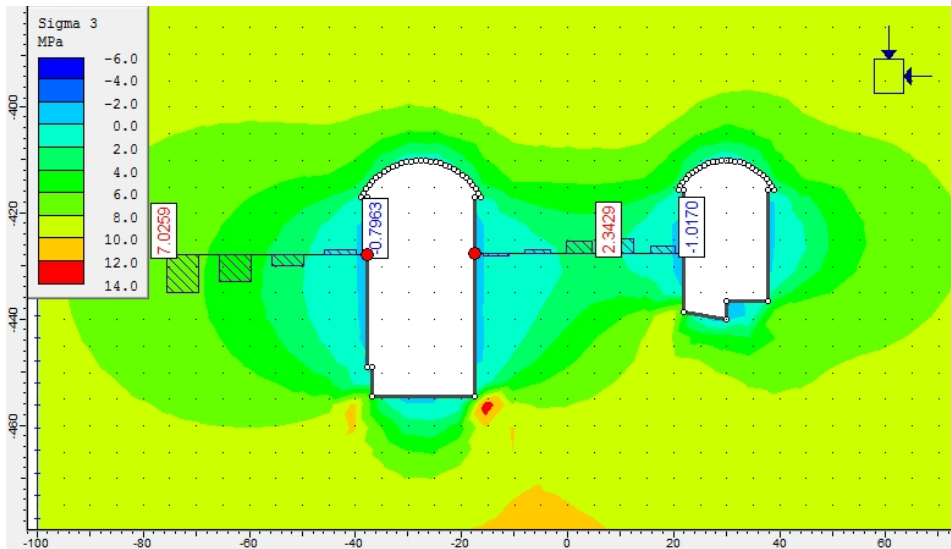


**Figure 4.25:** Examine<sup>2D</sup> model of the Tala powerhouse complex, depicting contours of equal  $\sigma_3$ , using literature input values

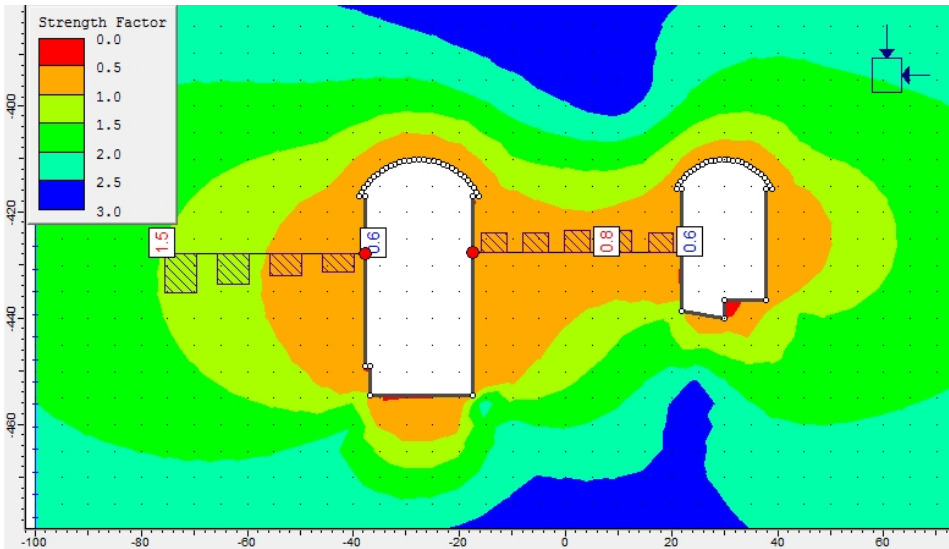


**Figure 4.26:** Examine<sup>2D</sup> model of the Tala powerhouse complex, depicting contours of equal strength factor, using literature input values

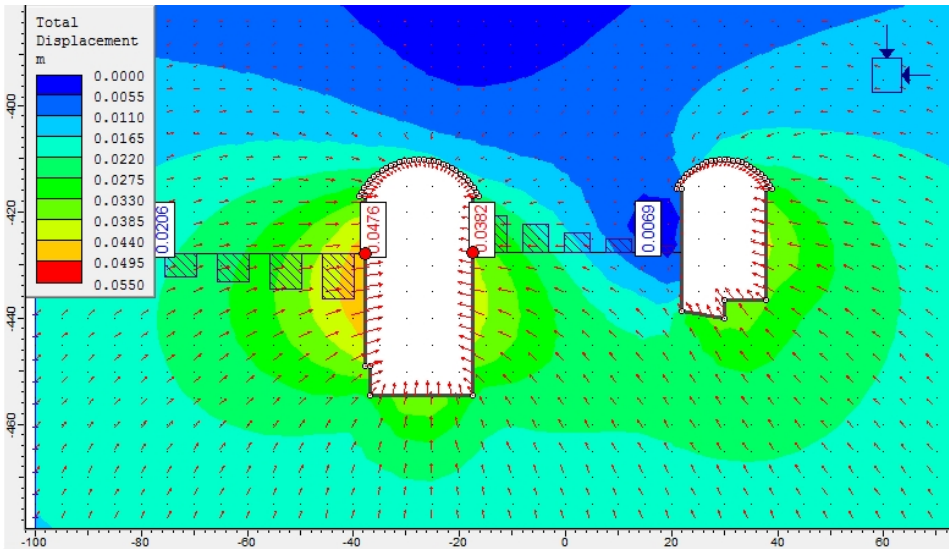


**Figure 4.27:** Examine<sup>2D</sup> model of the Tala powerhouse complex, depicting contours of equal total displacement, using literature input values



### 4.3.3 Phase<sup>2</sup>, literature values

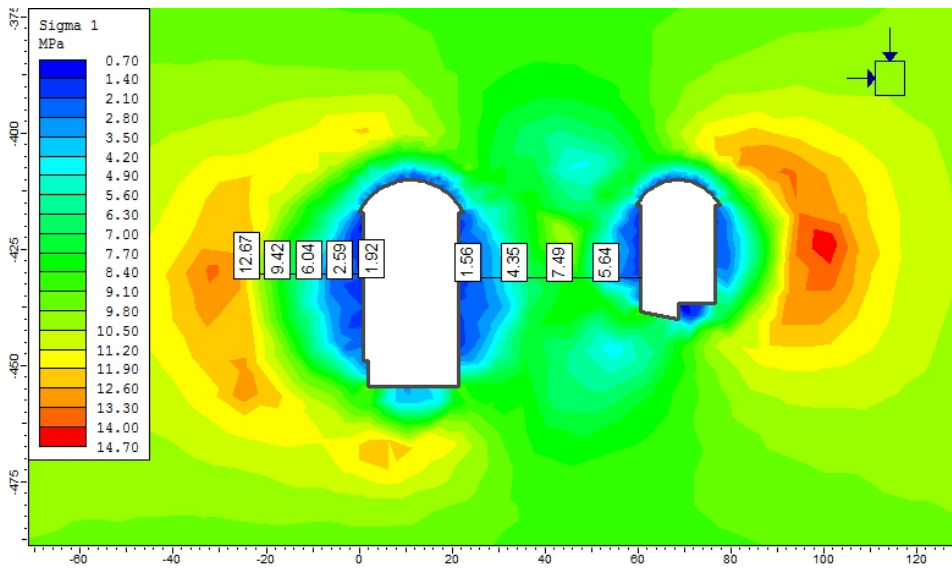


**Figure 4.28:** Phase<sup>2</sup> model of the Tala powerhouse complex, depicting contours of equal  $\sigma_1$ , using literature input values

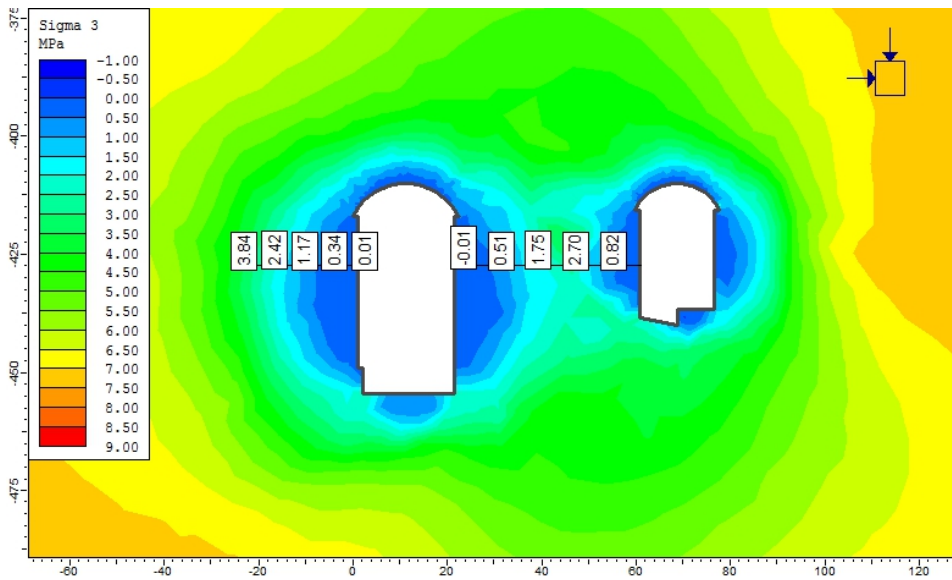


**Figure 4.29:** Phase<sup>2</sup> model of the Tala powerhouse complex, depicting contours of equal  $\sigma_3$ , using literature input values

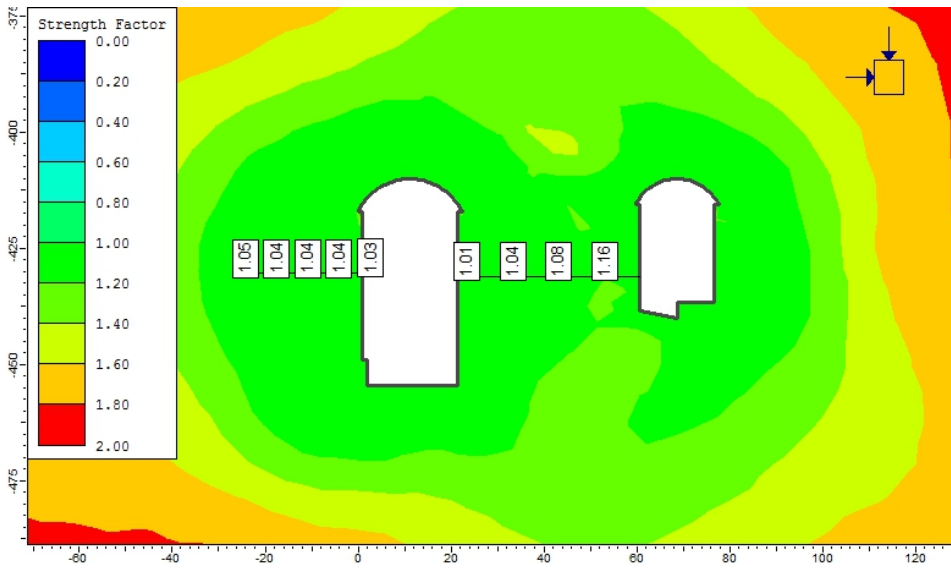


**Figure 4.30:** Phase<sup>2</sup> model of the Tala powerhouse complex, depicting contours of equal strength factor, using literature input values

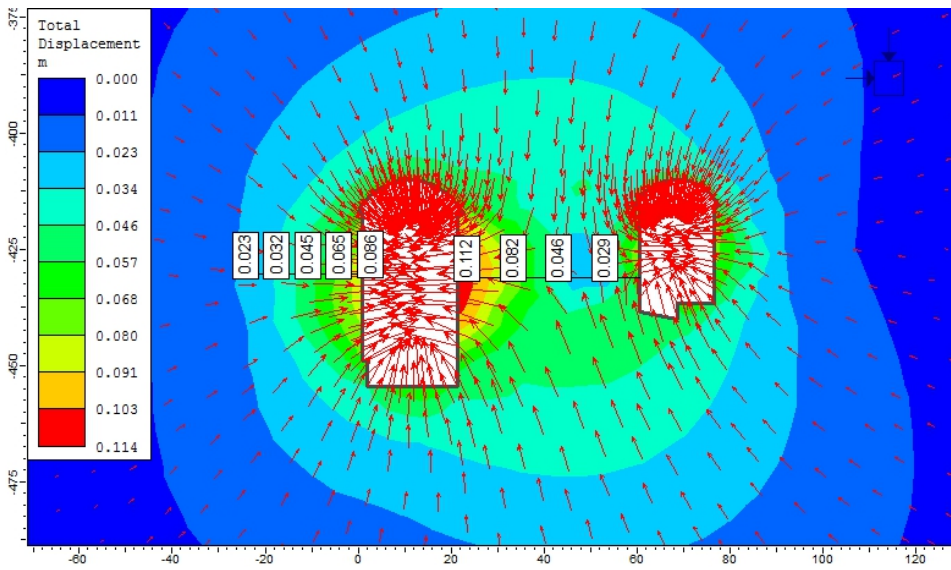


**Figure 4.31:** Phase<sup>2</sup> model of the Tala powerhouse complex, depicting contours of equal total displacement, using literature input values

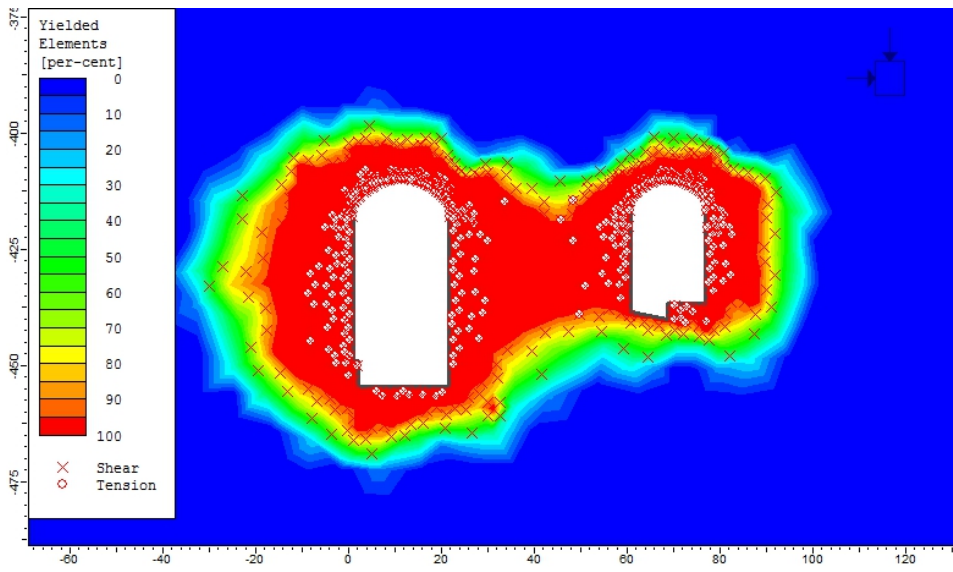


**Figure 4.32:** Phase<sup>2</sup> model of the Tala powerhouse complex, depicting yielded elements, using literature input values

---

## 4.4 Back - Calculation

In attempt to match the model to the actual measured convergence in the powerhouse of Tala, multiple versions with varying values of Young's modulus were computed. The results of that iteration is presented in figure 4.33. A value of 4250 MPa was chosen and a model constructed in Examine<sup>3D</sup> and Examine<sup>3D</sup> as well. With 4250 MPa Young's modulus the convergence in the mid wall section in the plastic model was 0,372 m, while the actual measured value was 0,374 m. The measured value of maximum displacement was from EL 525 m at RD 65 m, but in the model the displacement is uniform along the length of the cavern, except for the area closest to the end. Therefore the location of the convergence measurement comparison in the models was chosen in the middle of the cavern at RD 103 m and in the middle of the wall where the largest displacement was observed in the model. The strength parameters and the stress field were left untouched as the extent of the failure zone was deemed reasonable with the literature values. The MPBX observation in the powerhouse cavern showed rock failure to a depth between 15,6 m and 21,5 m, and the models showed failure zone defined by strength factor < 1 to depth of 18,4 m in Examine<sup>3D</sup> and 19,3 m in Examine<sup>2D</sup>. In the Phase<sup>2</sup> model, tensile failure (yielded elements) was observed to depth of 11 m.

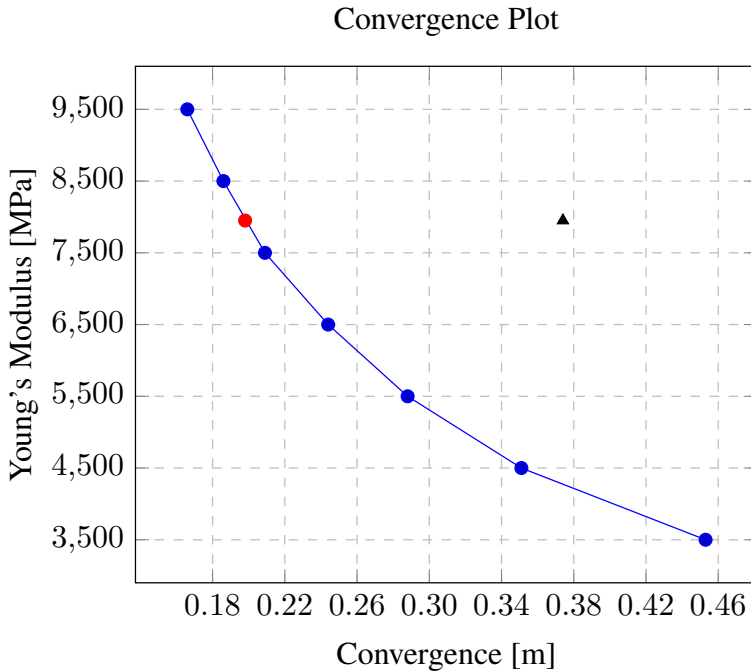


**Figure 4.33:** Measured value of convergence in the Phase<sup>2</sup> model at EL 515/RD 103 of the Tala machine hall, plotted against varying values of Young's modulus. The red mark indicates the convergence in the model with the literature value of Young's modulus at 7950 MPa and the black triangle is the measured value of maximum convergence of 0,374 m

---

#### 4.4.1 Examine<sup>3D</sup>, back-calculation

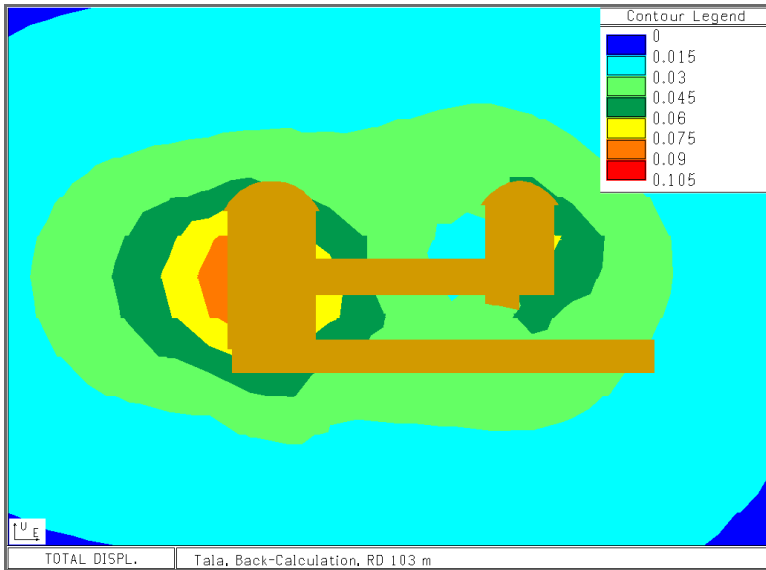


**Figure 4.34:** RD 103 m at Tala powerhouse complex, depicting contours of equal total displacement, using Young's modulus of 4250 MPa

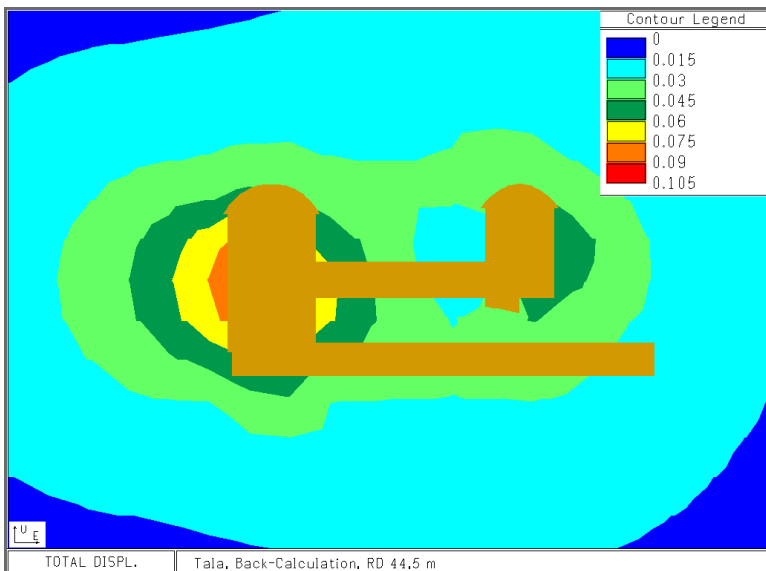


**Figure 4.35:** RD 44,5 m at Tala powerhouse complex, depicting contours of equal total displacement, using Young's modulus of 4250 MPa

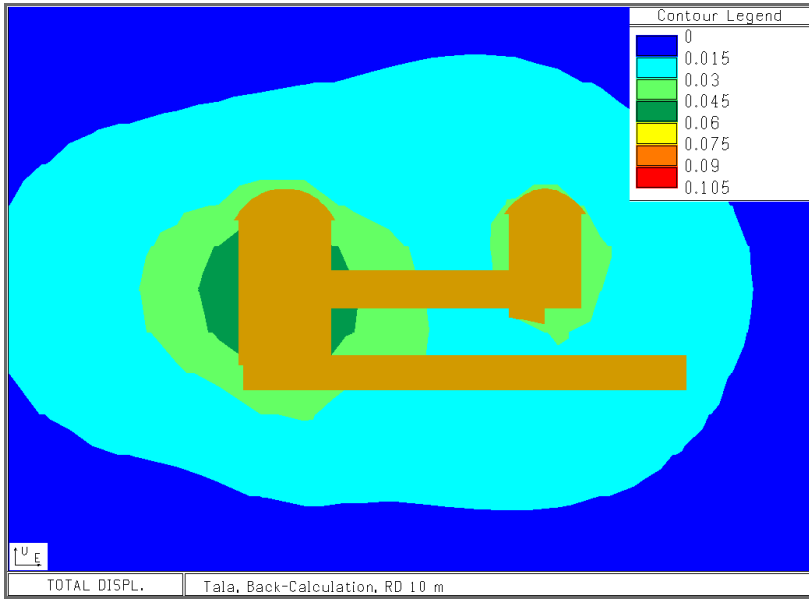


**Figure 4.36:** RD 10 m at Tala powerhouse complex, depicting contours of equal total displacement, using Young's modulus of 4250 MPa

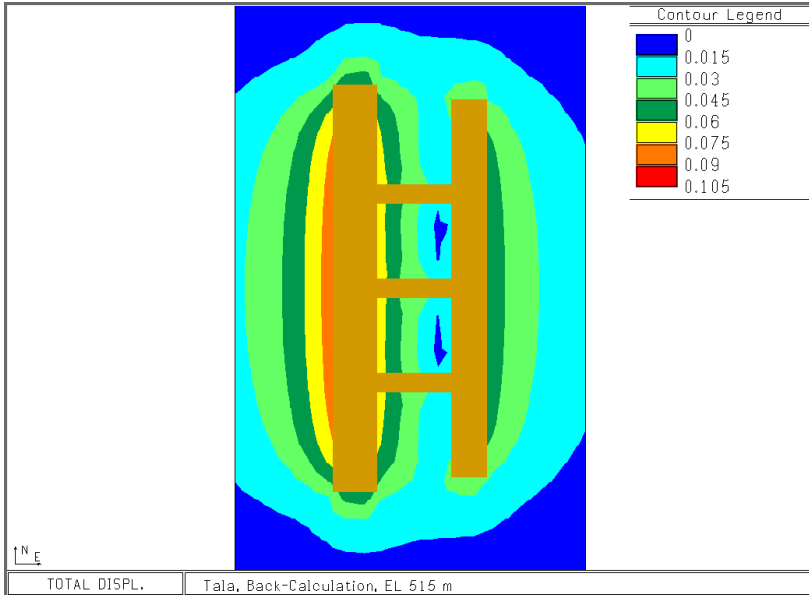


**Figure 4.37:** EL 515 m at Tala powerhouse complex, depicting contours of equal total displacement, using Young's modulus of 4250 MPa

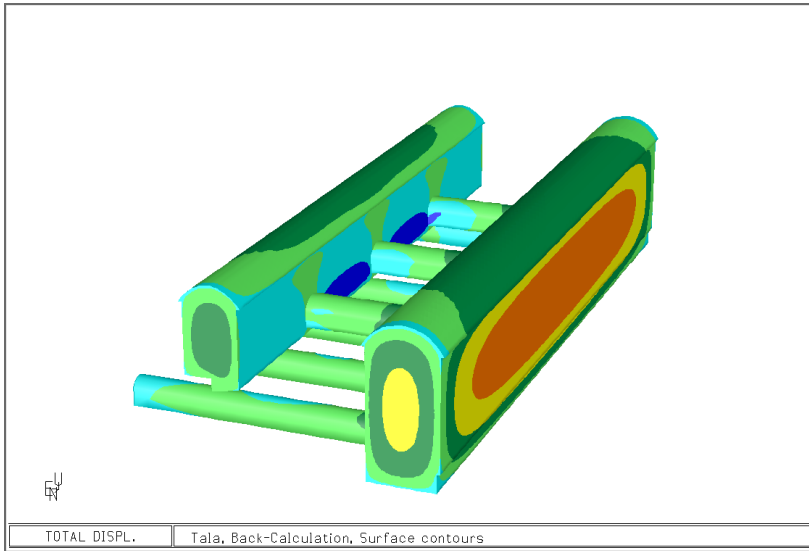


**Figure 4.38:** Perspective of the Tala powerhouse complex depicting the total displacement as it appears on the surface of excavation, using Young's modulus of 4250 MPa

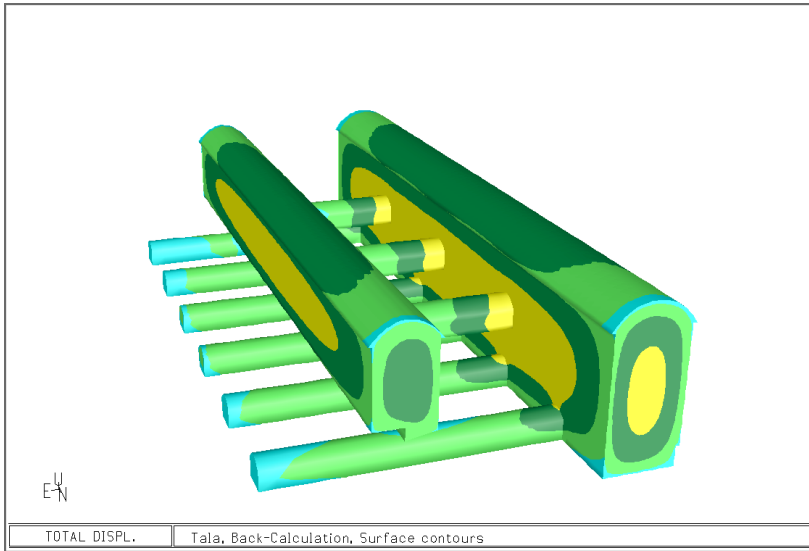


**Figure 4.39:** Perspective of the Tala powerhouse complex depicting the total displacement as it appears on the surface of excavation, using Young's modulus of 4250 MPa

---

## 4.4.2 Examine<sup>2D</sup>, back-calculation

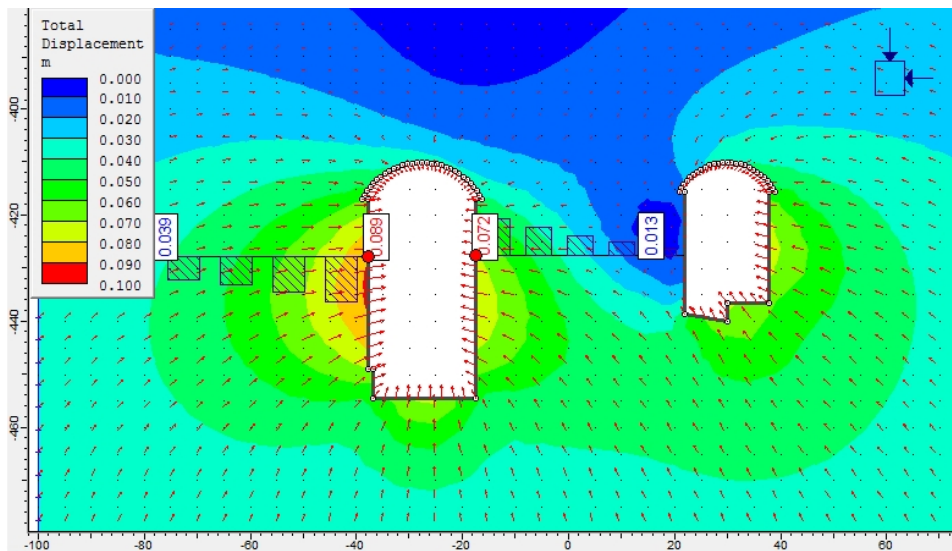


**Figure 4.40:** Examine<sup>2D</sup> model of the Tala powerhouse complex, depicting contours of equal total displacement, using Young's modulus of 4250 MPa



### 4.4.3 Phase<sup>2</sup>, back-calculation

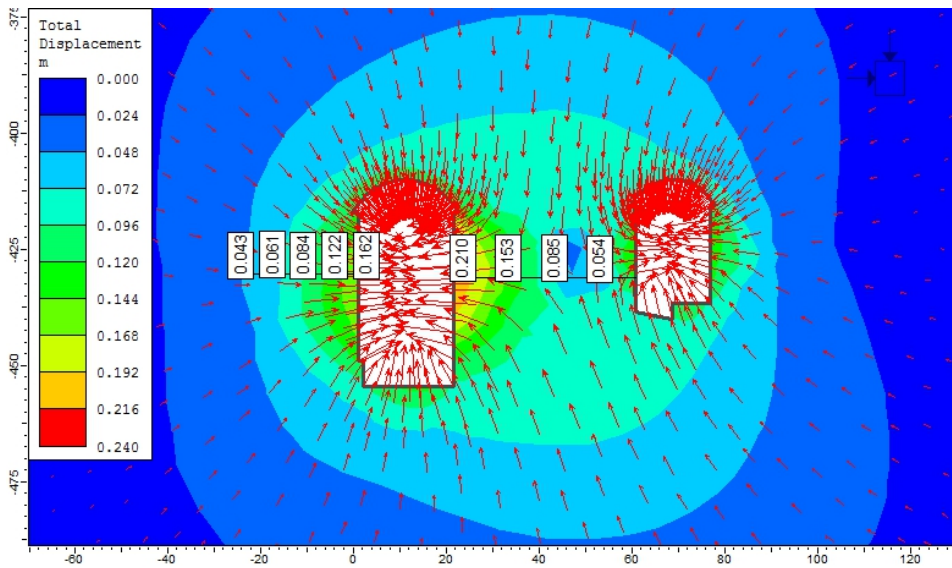


**Figure 4.41:** Phase<sup>2</sup> model of the Tala powerhouse complex, depicting contours of equal total displacement, using Young's modulus of 4250 MPa

---

## 4.5 Examine<sup>3D</sup>, Chhukha

The nearby powerhouse at Chhukha was modelled for comparison. The input parameters and the model properties are listed in tables 4.1, 4.2 and 4.4. The cutting planes are located in the middle of the cavern lengthwise at RD 70,6, at RD corresponding the height at RD 37,5 m, at RD 5 m and in the middle of it height-wise at EL 1385 m. Figure 4.42 shows the layout of the cutting planes.

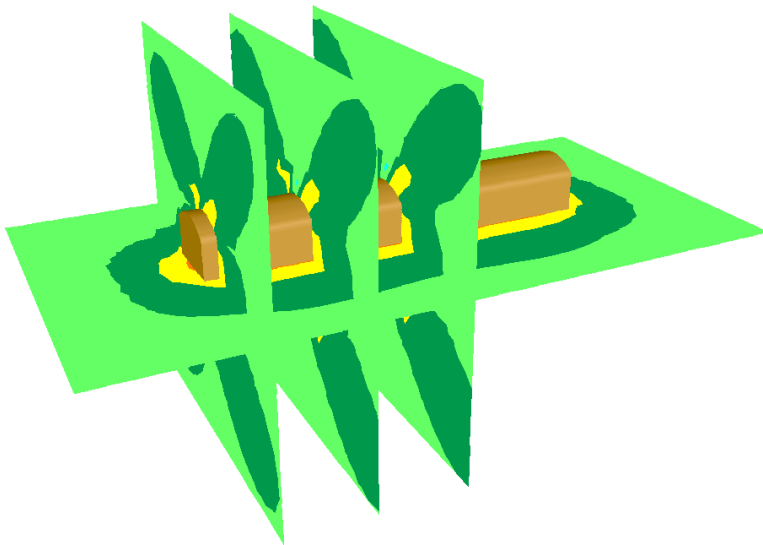


**Figure 4.42:** Perspective of the cutting planes in the 3D model of Chhukha

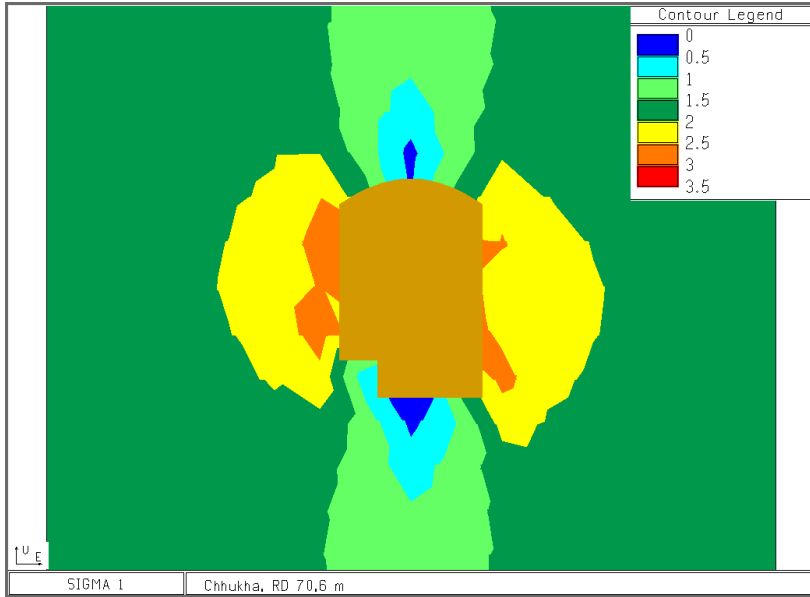


**Figure 4.43:** RD 70,6 m at Chhukha powerhouse cavern, depicting contours of equal  $\sigma_1$

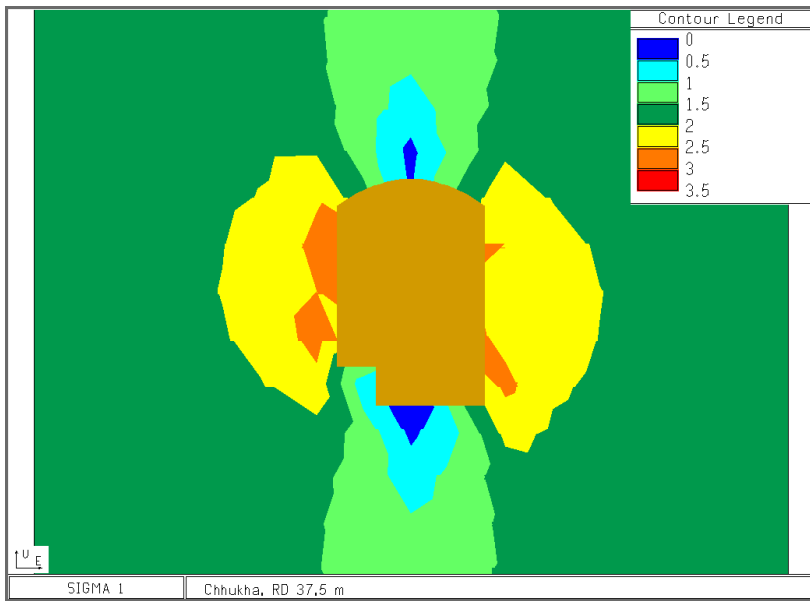


**Figure 4.44:** RD 37,5 m at Chhukha powerhouse cavern, depicting contours of equal  $\sigma_1$

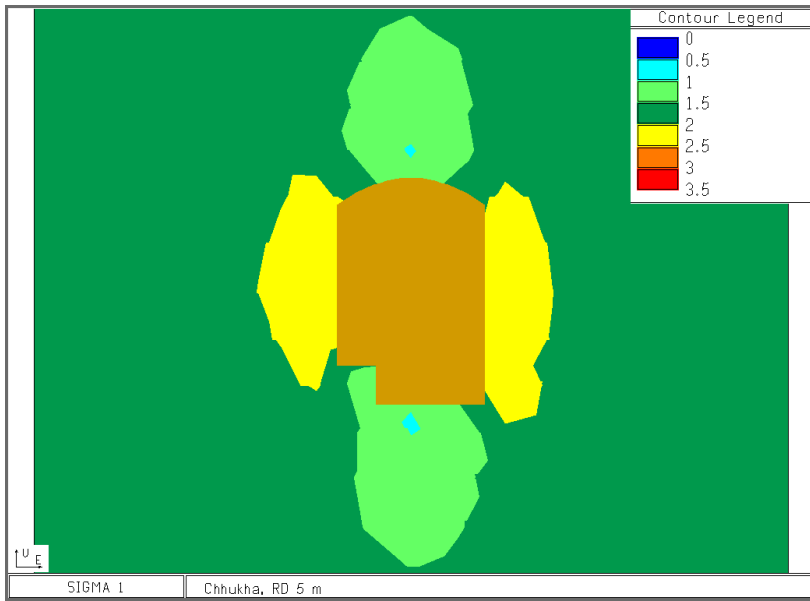


**Figure 4.45:** RD 5 m at Chhukha powerhouse cavern, depicting contours of equal  $\sigma_1$

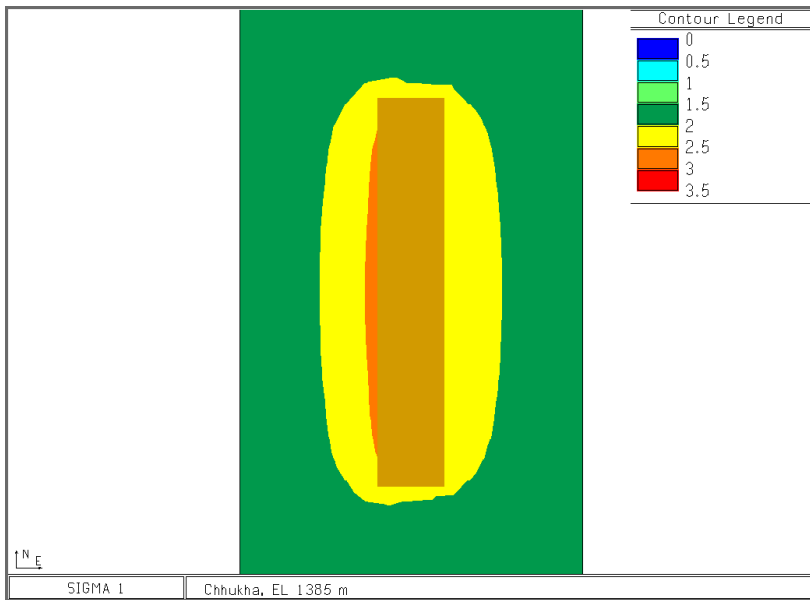


**Figure 4.46:** EL 1385 m at Chhukha powerhouse cavern, depicting contours of equal  $\sigma_1$

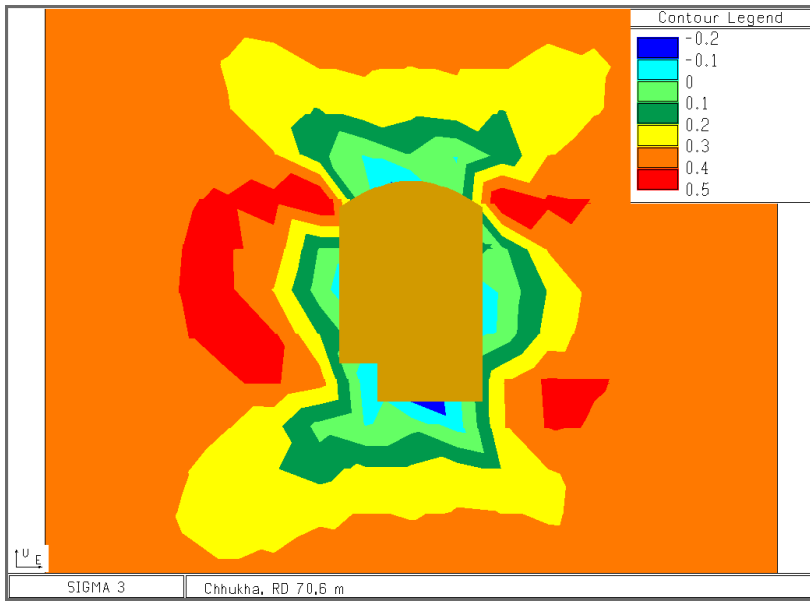


**Figure 4.47:** RD 70,6 m at Chhukha powerhouse cavern, depicting contours of equal  $\sigma_3$

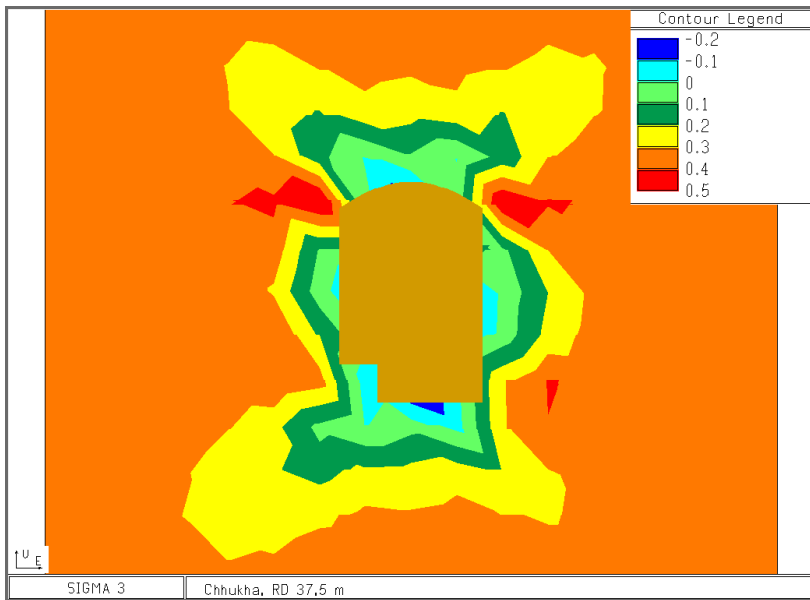


**Figure 4.48:** RD 37,5 m at Chhukha powerhouse cavern, depicting contours of equal  $\sigma_3$

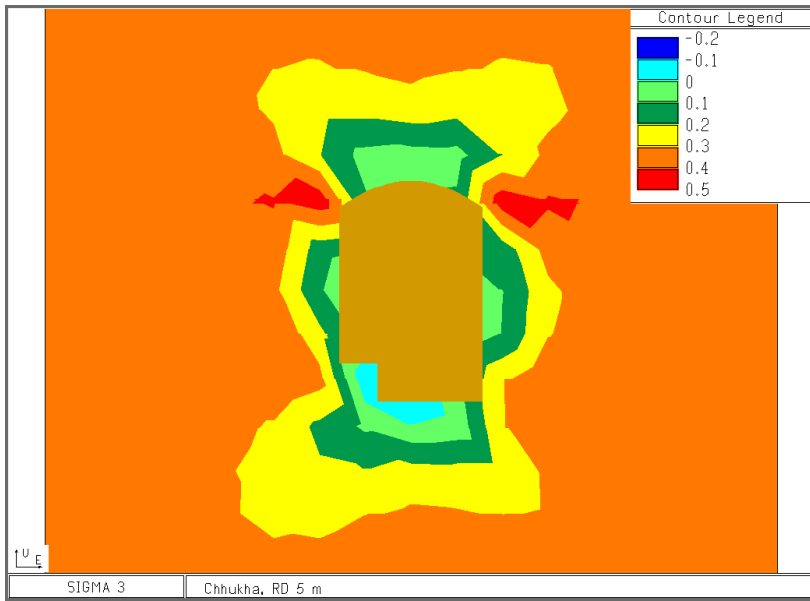


**Figure 4.49:** RD 5 m at Chhukha powerhouse cavern, depicting contours of equal  $\sigma_3$

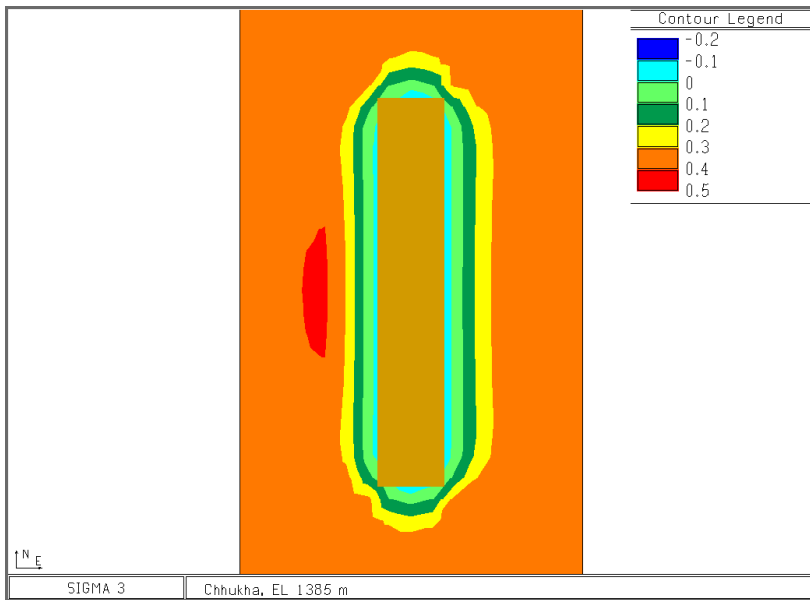


**Figure 4.50:** EL 1385 m at Chhukha powerhouse cavern, depicting contours of equal  $\sigma_3$

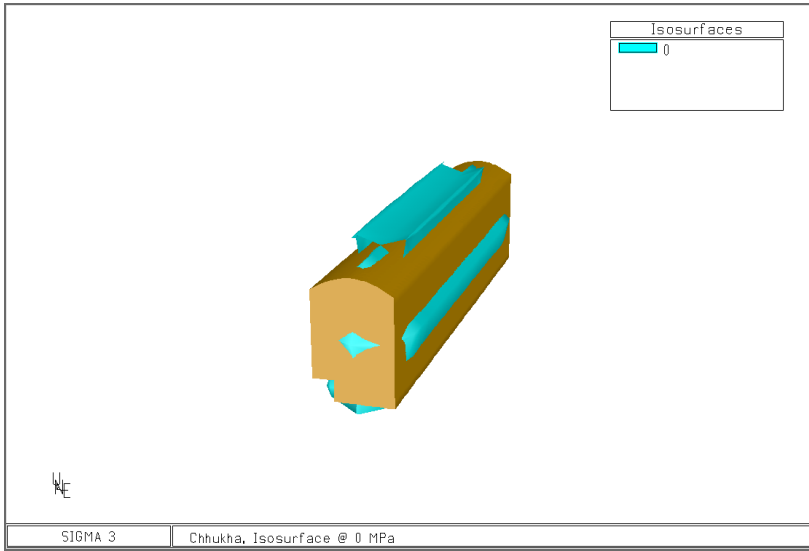


**Figure 4.51:** Perspective of the Tala powerhouse complex, depicting isosurface at  $\sigma_3 = 0$

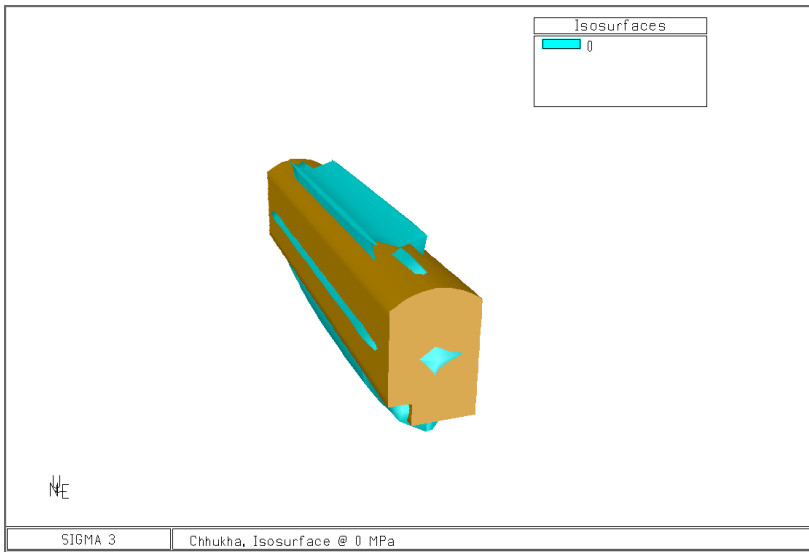


**Figure 4.52:** Perspective of the Tala powerhouse complex, depicting isosurface at  $\sigma_3 = 0$

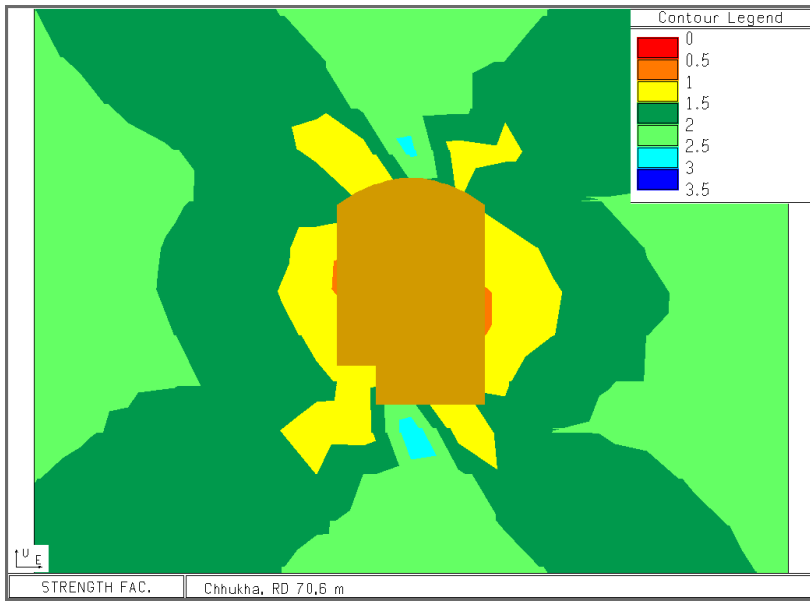


**Figure 4.53:** RD 70,6 m at Chhukha powerhouse cavern, depicting contours of equal strength factor

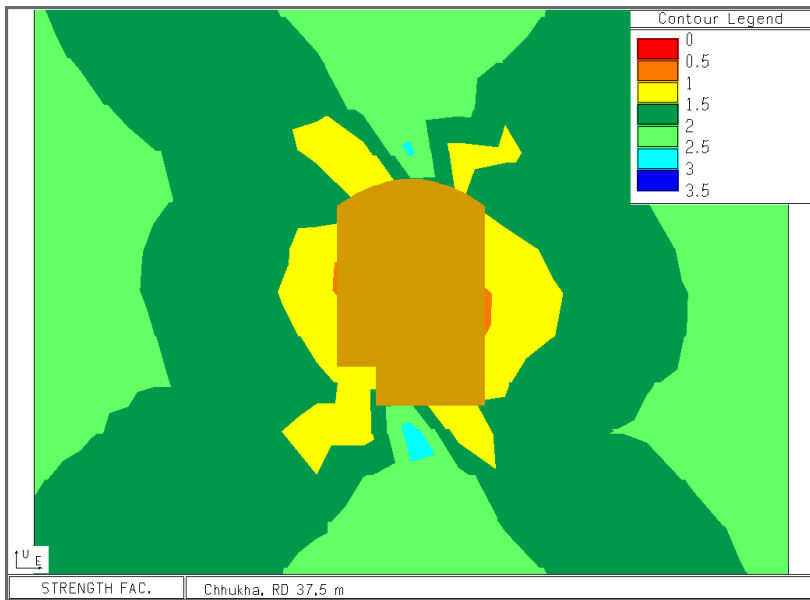


**Figure 4.54:** RD 37,5 m at Chhukha powerhouse cavern, depicting contours of equal strength factor



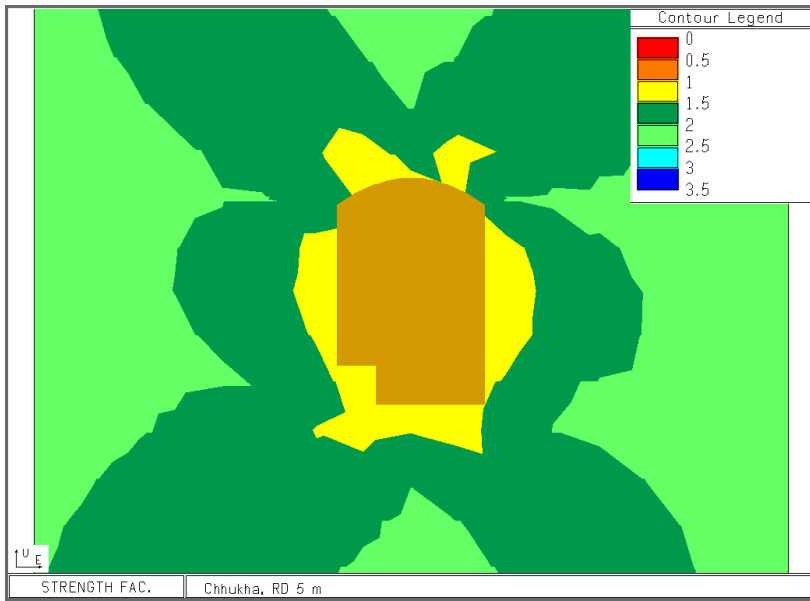


**Figure 4.55:** RD 5 m at Chhukha powerhouse cavern, depicting contours of equal strength factor

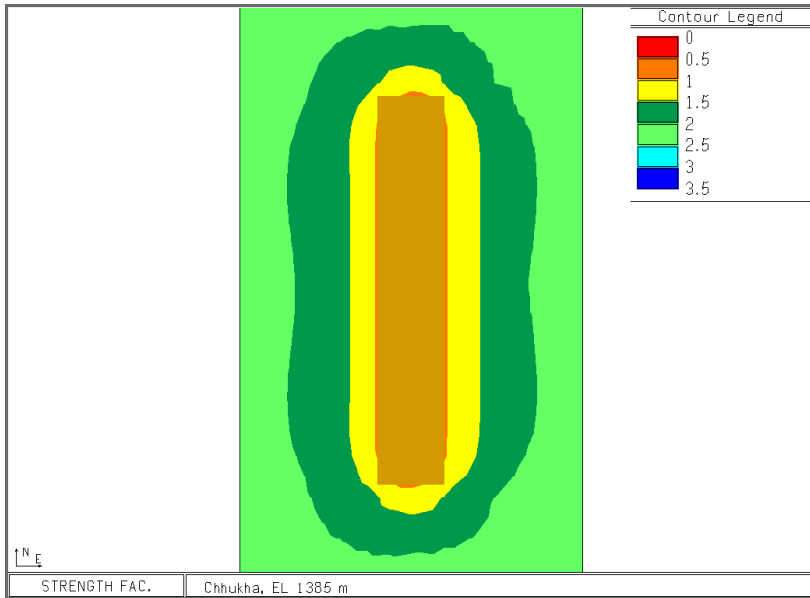


**Figure 4.56:** EL 1385 m at Chhukha powerhouse cavern, depicting contours of equal strength factor

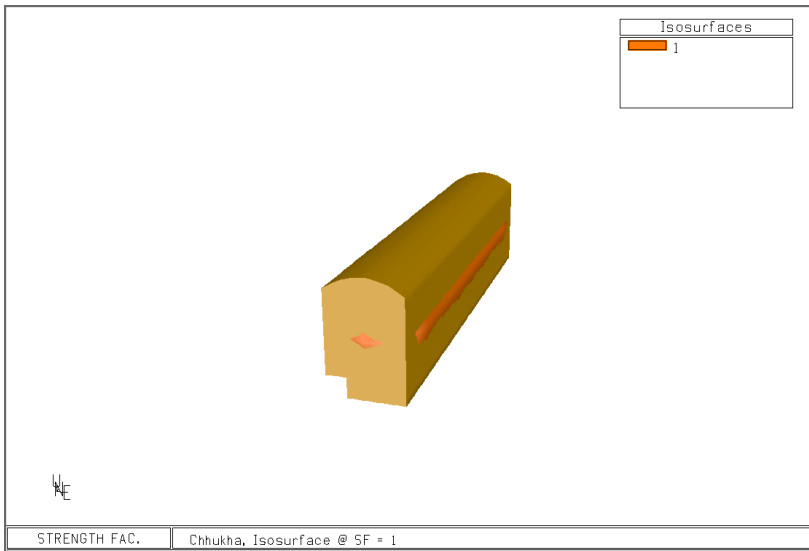


**Figure 4.57:** Perspective of the Chukha powerhouse cavern, depicting isosurface at strength factor = 1

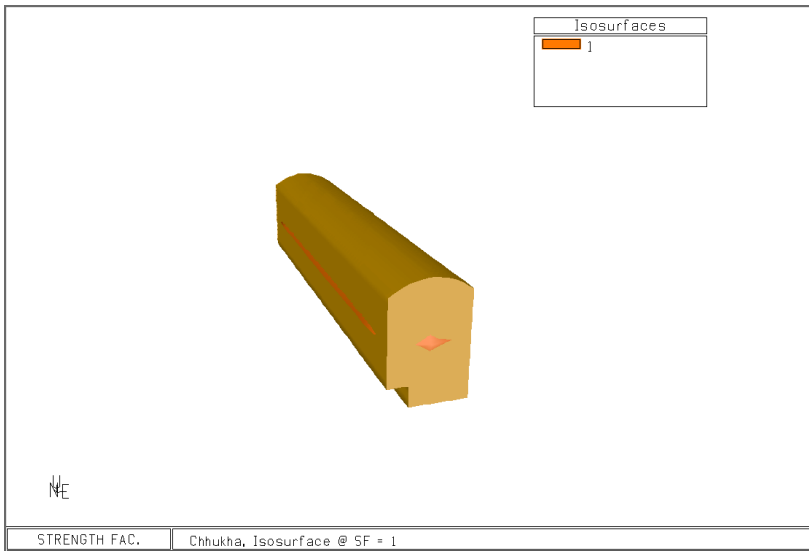


**Figure 4.58:** Perspective of the Chukha powerhouse cavern, depicting isosurface at strength factor = 1

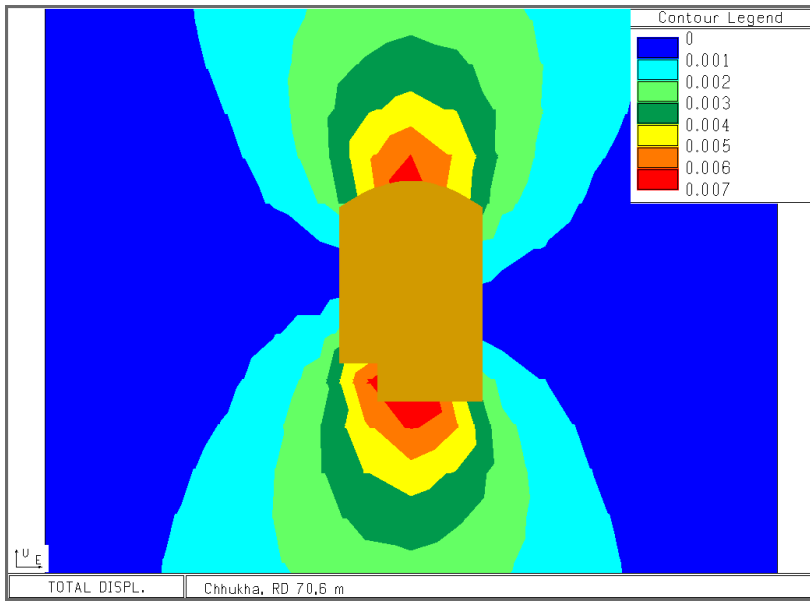


**Figure 4.59:** RD 70,6 m at Chhukha powerhouse cavern, depicting contours of equal total displacement

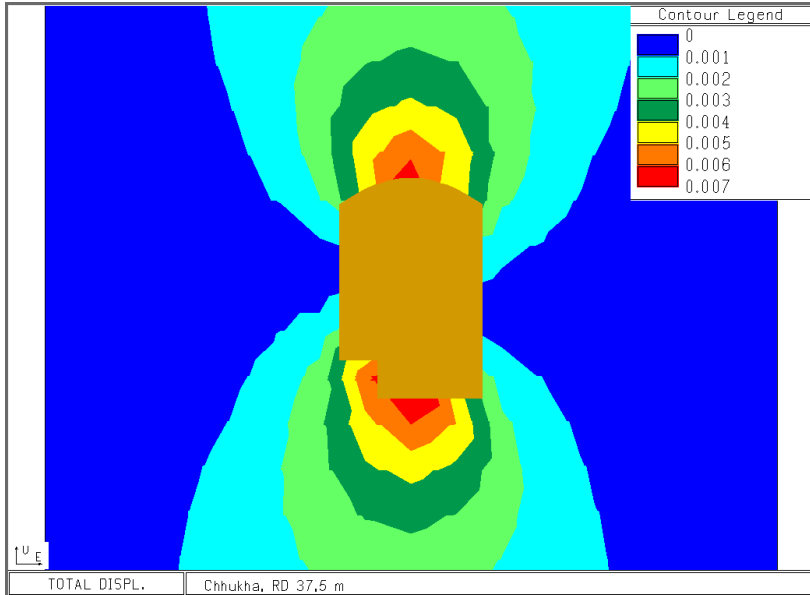


**Figure 4.60:** RD 37,5 m at Chhukha powerhouse cavern, depicting contours of equal total displacement

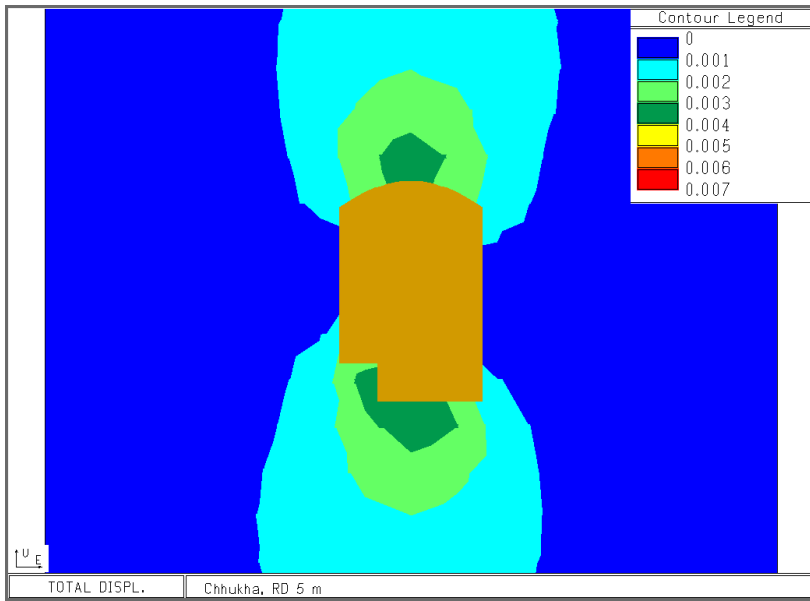


**Figure 4.61:** RD 5 m at Chhukha powerhouse cavern, depicting contours of equal total displacement

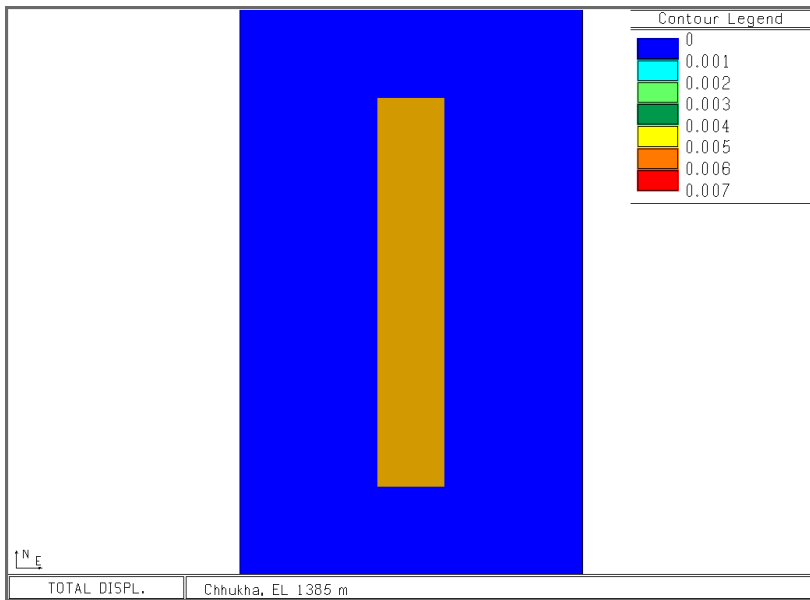


**Figure 4.62:** EL 1385 m at Chhukha powerhouse cavern, depicting contours of equal total displacement

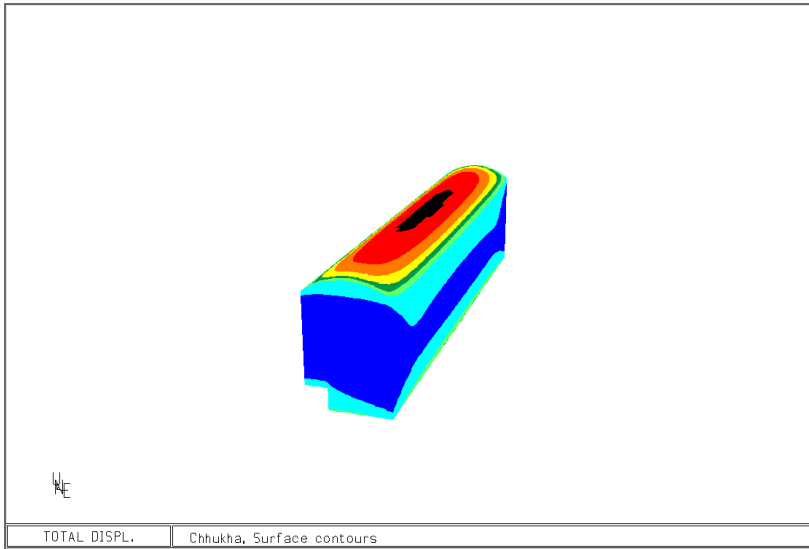


**Figure 4.63:** Perspective of the Chhukha powerhouse cavern, depicting the total displacement as it appears on the surface of excavation

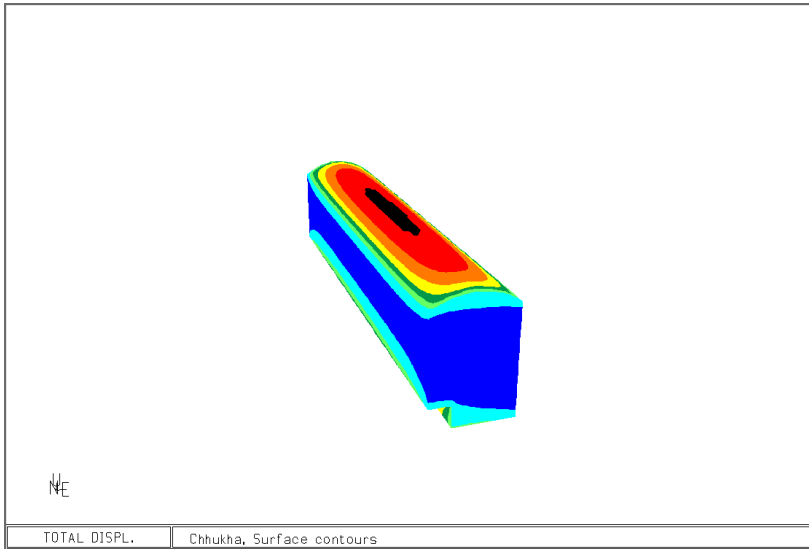


**Figure 4.64:** Perspective of the Chhukha powerhouse cavern, depicting the total displacement as it appears on the surface of excavation

---

---

## Discussion

### 5.1 Tala powerhouse complex: Literature input parameters

#### 5.1.1 Examine<sup>3D</sup>

The major principal stress,  $\sigma_1$ , is generally parallel to the long axis of the caverns. Where the stress is concentrated near the excavation boundary it tends to follow the boundary. At RD 103 m the major induced principal stress ranges from 9 - 19 MPa, and is largest where the bus duct meets the transformer hall. There it reaches 19 MPa and is oriented along the length axis of the caverns. The upstream wall of the powerhouse cavern seems de-stressed, where the major principal stress is vertical and within the range of 9 - 13 MPa in the mid-section of the wall. De-stressed zone appears between the tailrace tunnels under the transformer cavern. In the lower corner of the upstream wall of the powerhouse cavern the stress reaches 17 - 19 MPa. The induced major principal stress follows the same trend in other cutting planes, although the magnitude decreases at RD 10 m. There the major principal stress is generally of magnitude 15 - 17 MPa parallel to the caverns. Small zone of concentrated stress forms in the upper corner of the downstream wall of the powerhouse cavern, where the stress reaches 17 - 19 MPa.

The minor principal stress  $\sigma_2$ , tends to be towards the excavation. Low tensile stress, in the lower range of 0 - 2,5 MPa, can be observed in the walls of the powerhouse cavern along the whole length of it, although it decreases in towards the ends. Where the bus ducts meet the powerhouse cavern, higher tensile stress forms, drawing near 2,5 MPa.

The failure zone surrounding the caverns is defined where the strength factor, according to the Hoek-Brown failure criterion, is less than 1. As can be seen in the contour plots of the strength factor the failure zone is extensive, reaching depth of 19,3 m in the upstream wall of the powerhouse cavern. Additionally, the isosurface plots show how the complex is almost completely encapsulated in the failure zone. The whole pillar between the two

---

caverns is by that definition likely to experience failure.

The displacement shown here is only the elastic part of the actual total displacement of the rockmass. As the rockmass is considered fully elastic, plastic deformation and fracturing can not be represented. Due to this the deformation calculation is very conservative. By combining the total displacement in the excavation surface in EL 515 / RD 103 of the powerhouse cavern, convergence of 0,082 m was measured. That is significantly lower than the actual measured value of 0,374 m in the powerhouse cavern. All displacement is towards the cavern and contours of total displacement used for more detailed scale. The distribution of the displacement is clearly seen in the plots portraying the surface contours. The displacement is at its most in the upstream wall of the powerhouse cavern, at 0,042 - 0,049 m.

### 5.1.2 Examine<sup>2D</sup>

The contours of the major principal stress at Tala powerhouse complex from the 2D BEM model Examine<sup>2D</sup> show concentrated stress in the roof and in around the corners of the caverns. The stress ranges from 15 - 20 MPa in the roof of both caverns and peaks at 25 MPa in the corners. The walls of both caverns are de-stressed, showing magnitude of  $\sigma_1$  to be between 9 and 10 MPa. The minor principal stress is in the range of -2 - 10 MPa in the near vicinity of the caverns, peaking at 14 MPa in the lower downstream corner of the powerhouse cavern. Minor tension stresses are induced in the walls of both caverns.

The extent of the failure zone, defined by strength factor being less than 1, is large. Upstream of the powerhouse cavern it reaches depth of 18 m and covers the whole pillar between the two caverns. Downstream of the transformer hall the depth is 12 m.

The displacement around the powerhouse is most notable in the walls, where convergence of 0,085 m can be observed. The total displacement in the upstream wall of the transformer cavern is low, where the displacement of the whole pillar is towards the larger powerhouse cavern. Closer to the transformer hall the effect of that opening starts to influence the rock mass and in the upstream wall the total displacement is as low as ~0,006 - 0,007 m. In the surface of the downstream wall on the other hand, the displacement towards the cavern is ~0,039 m.

### 5.1.3 Phase<sup>2</sup>

In the 2D FEM model the area near the excavation boundaries is de-stressed, where the major principal stress measures generally under 4 MPa. Around 20 m outside of the excavations the stress peaks at 12 - 14 MPa, more so downstream of the transformer hall. The major principal stress in the pillar peaks in the centre and decreases towards both caverns, at higher rate towards the larger powerhouse cavern. In the excavation boundaries  $\sigma_1$  is highest in the lower corners of both caverns at 7 - 8 MPa. The minor principal stress is close to 0 MPa in the contours. Minor tensile stress of 0,01 MPa forms in the downstream wall of the powerhouse cavern.



---

The plots showing the strength factor show that it never goes below 1, indicating that the strength of the rock mass exceeds the induced stresses working on it. The total displacement is generally towards the excavations. Displacement in the walls of the powerhouse caverns adds up to 0,198 m convergence, with larger displacement in the pillar wall. The displacement in the roof is 0,06 m in the powerhouse cavern and 0,05 m in the transformer hall. The floor shows displacement of 0,065 m in both caverns.

The yielded elements plots show that the rock mass is should be failing around the two caverns. The failure zone extends to depth of 11 m in the upstream wall of the powerhouse cavern. In the pillar the tensile failure zone reaches 8 m from the powerhouse cavern and 6 m from the transformer hall. Downstream of the transformer hall it reaches 5 m. In the roof of both caverns the yielded elements are dominating and dense up to depth of 2 m along both roof arches. The model also shows few yielded elements in the floor. All in all there are 993 yielded elements in the model, out of 3196 total.

## 5.2 Tala Powerhouse Complex: Back - Calculation

An attempt was made to match the actual values of extent of failure zone and convergence in the Tala powerhouse cavern. As the only input parameter changed was the Young's modulus, no changes in the stress field were observed in the 3D model, as can be seen in the contour plots in Appendix B. Same goes for failure zone defined by strength factor less than 1, as it is only based on the rock strength and the stresses working on it. However, the convergence increased from 0,084 m to 0,154 m at EL 515 m RD 103. At same elevation at RD 10 m the convergence increased from 0,058 m to 0,107 m.

As the model from Examine<sup>2D</sup> is based on the same principles, there are no notable changes in the stress field or the extent of failure zone. In the 2D BEM model the convergence can be obtained from the total displacement in the powerhouse walls as 0,161 m.

In the 2D FEM model made with Phase<sup>2</sup> the stress distribution is more or less the same, albeit higher values of  $\sigma_1$  are apparent closest to the excavation. No notable change was seen in the contour plots of  $\sigma_3$ , regardless of the change of the Young's modulus. Same applies when viewing the strength factor plots, where no significant change can be observed.

As the Young's modulus is the major contributing factor to the displacement in the model, it changes drastically by lowering it. The value of the modulus was chosen based on the convergence measured in the powerhouse cavern and matched to the actual measured convergence. The value of 4250 MPa used here comes up with convergence of 0,372 m in the powerhouse cavern, compared to the 0,374 m measured on site. The displacement is larger in the downstream wall, or 0,210 m, and 0,162 m in the upstream wall. Those values are obtained in the middle of the cavern height, at EL 515 m, where it is at its maximum.

No change is observed regarding yielded elements. The failure zone defined by the tension yielding elements is the same around the caverns and the number of yielded elements stays the same at 993.

---

### 5.3 Chhukha Powerhouse cavern

In the low magnitude in-situ stress field at Chhukha the roof and floor become de-stressed, showing the major principal stress of 0,5 - 1,75 MPa in both the roof and the floor. The orientation of the major principal stress is generally vertical but closest to the opening it tends to follow the contour of it for most of the length of the cavern. No notable difference is seen between RD 70,6 m and RD 37,5 m. At RD 5 m, where the effect of the undisturbed rock in the end is started to influence the stress field, the major principal stress is vertical in the roof and the floor. The major principal stress in the walls ranges from 2 - 2,5 MPa and from 1 - 2 MPa in the roof and the floor.

The minor principal stress around the opening is in the range of -0,3 - 0,3 MPa. At RD 70,6 m tensile stress forms in the walls and both the roof and the floor but in the junctions the minor principal stress is in the range between 0,12 - 0,30 MPa. The orientation is mostly towards the opening nearest to it, except for in the middle of the roof and the floor where it is along the long axis. No notable difference is seen between RD 70,6 m and RD 37,5 m. At RD 5 m the magnitude of the minor principal stress is generally lower, both tensile and compressive. The extent of the zone experiencing tensile stress is smaller. The orientation is mostly the same except that in the roof and the floor it is more towards the cavern.

Based on the strength factor plots the Chhukha powerhouse cavern seems rather stable. The only zones showing strength factor under 1 is in the mid section of the walls, and in the middle of the end walls, reaching depth of ~1 m in those places. RD 5 m is close enough to the end wall to benefit from the whole rock in the end wall, so the failure zone is no longer observed in the wall. It appears at RD ~7 m. Displacement is near non-existent in the cavern. The displacement is mainly in the roof and the floor, and is maximum of 0,007 m in the floor. The walls show displacement of only 0,001 m towards the opening, resulting in convergence of 0,002 m.

### 5.4 Summary of Stability Analyses

When comparing the two projects of Tala and Chhukha it is apparent that the powerhouse complex of Tala is more prone to stability problems than the cavern at Chhukha. The higher stress regime at Tala leads to time dependant deformation of the rock mass, like the continued rock support failure long after excavation indicates. The tensile stress in the walls of the powerhouse contributes to the failure scheme as well. Throughout the whole pillar width between the caverns at Tala the strength factor is  $< 1$ , indicating possible failure. The strength factor analysis of the Chhukha cavern show only minimal failure zones in the walls.

The two elastic models show good resemblance overall with regards to the cutting planes at RD 103 m and RD 44,5 m in the 3D model. However, the analysis at RD 10 m, where the end effect is starting to influence the rock mass, differs from the 2D analysis as the excavation is considered endless.

---

The elastic models both show higher compressive strength than the plastic model and the plastic model shows no signs of tensile stress in the points summarized in table 5.1. The higher stress regime in the elastic models is due to the stress release upon failure in the plastic model. No actual failure occurs in the elastic models. With same reasoning the displacement in the plastic model is larger. The amount of displacement from the elastic models is only about 40% of the displacement observed in the plastic model, both when using the literature values and the back - calculation values. By the nature of elastic modelling, no displacement in the form of openings forming in the rock mass can be accounted for, making the estimate very conservative. However, the trend of displacement is the same through all of the models, indicating where the displacement of various magnitude can be expected.

**Table 5.1:** Comparison between different modelling methods. Four points were measured precisely in all three modelling software and values obtained for the principal stresses, depth of failures zone defined by strength factor < 1 (FZ depth) and total displacement. The four points are the mid section of the upstream wall of the powerhouse cavern, the mid section of the transformer hall downstream cavern and the middle of the roofs of both caverns

Parameter	Powerhouse: US wall				Transformer hall: DS wall			
	Examine <sup>3D</sup>		Examine <sup>2D</sup>	Phase <sup>2</sup>	Examine <sup>3D</sup>		Examine <sup>2D</sup>	Phase <sup>2</sup>
	RD 103 m	RD 10 m			RD 103 m	RD 10 m		
$\sigma_1$ [MPa]	11,0	15,3	9,24	1,81	15,0	14,5	10,9	2,77
$\sigma_3$ [MPa]	-1,5	-0,7	-0,8	0,01	0,5	3,4	-0,8	0,2
FZ depth [m]	19,2	14,5	12,5	0	11,3	2,0	8,2	0
Displacement [m]	0,047	0,031	0,048	0,086	0,032	0,021	0,039	0,073

Parameter	Powerhouse: Roof				Transformer hall: Roof			
	Examine <sup>3D</sup>		Examine <sup>2D</sup>	Phase <sup>2</sup>	Examine <sup>3D</sup>		Examine <sup>2D</sup>	Phase <sup>2</sup>
	RD 103 m	RD 10 m			RD 103 m	RD 10 m		
$\sigma_1$ [MPa]	15,5	16,5	22,0	3,13	15,0	15,0	17,4	2,63
$\sigma_3$ [MPa]	4,5	4,5	0,1	0,38	4,5	5,0	0,8	0,15
FZ depth [m]	3,2	3,8	2,9	0	1,0	0	2,0	0
Displacement [m]	0,022	0,017	0,021	0,061	0,025	0,016	0,021	0,051

## Conclusion and Recommendations

The models reviewed here are in accordance with assumptions made in chapter 3.4, that the conditions for large scale underground excavation is much more favourable at the location of Chhukha. The higher stress regime at Tala leads to more instability issues due to high induced stresses, in addition to more favourable design in regards to discontinuities and orientation of the caverns. The model of the Chhukha powerhouse cavern shows that the rock mass quality and the stress field is unlikely to have induced the failure in the rock mass. The rock fall in the crown during excavation was most likely due to unfavourably aligned discontinuities, resulting in wedge formation.

The post-construction failure that the Tala powerhouse complex has experienced can be partly explained by the high stress field in and the resulting time dependant deformation. As deformation continues bolts take on more load and eventually fail or the anchoring fails. That in addition to poor rock quality and suboptimal alignment of the caverns with respect to jointing and foliation in the rock mass makes the construction unstable. As for the pillar width, the strength factor observed in both of the elastic models showed values below 1 throughout the whole pillar width, indicating that the structural stability would benefit from wider pillar. However, increased cost of wider pillar in form of extended excavation of bus ducts and increased length of all connections between the two caverns need to be taken into account. Long term structural stability should though be considered to weigh more in the design.

The overall comparison between the two elastic BEM methods shows good resemblance for all but the ends of the 3D model where the non-excavated ends provide structural stability to the sections nearest to them. However, the plastic FEM model differed highly to the elastic models, as expected. By the nature of plastic modelling failure in the rock mass is accounted for, resulting in de-stressed environment. The plastic model showed minimal tensile stress and lower compressive stress in the host rock. The strength factor calculations based on the Hoek-Brown failure criterion did not show any areas around the caverns but analysis of yielded element showed failure in the rock mass to depth of 11 m

---

in the upstream wall of the powerhouse cavern. The elastic models showed only 40% of the displacement observed in the plastic model as displacement as result of brittle failure being considered as well as the elastic deformation of the rock.

The back - calculation, or matching of plastic model with the actual convergence, showed that the Young's modulus needed to be dropped from the 7950 MPa value, measured and used in the constructions phase, to 4250 MPa. That way the convergence measured in the model rose to 0,372 m compared to the actual maximum value of 0,374 m and used here for the comparison. The change of the Young's modulus did not have any notable effect on other analytical parameters in any of the models. When the elastic models were run with same value they gave similar result between themselves. Just like when using the input parameters from the literature the convergence was about 40% of the convergence observed in the plastic model

The Examine<sup>3D</sup> code can prove useful in the design stage of any underground excavation. The actual results regarding the magnitude of stresses, failure and deformation may not be exact, but the advantage of being able to see the distribution, orientation and trends of diverse parameters in the medium is apparent. Being able to visualize the condition regarding the stress field and the rock mass response in a 3D space can be used to optimize the design. The orientation of the long axis of excavations, with respect to the stress field, can be optimized by running multiple versions of the model where the alignment is changed. In the same way input parameters for the rock mass quality and strength can be studied for sensitivity by iterating different values systematically and observe the change in the entirety of the excavation.

The challenges of underground excavation in the complex geology of the Himalayas are apparent. As reviewed in chapter 3.2.2, the initial values assigned to the rock mass properties differed from the values actually measured in the cavern in investigations carried out after the rock fall in the crown portion of Tala. The models, using parameters obtained in these investigations, yet again show different reality. Although the shortcomings of the models, when dealing with discontinuities and various material, are kept in mind, both the elastic models and the plastic model show much less deformation then encountered in the Powerhouse of Tala, eventually leading to failure in rock support and unstable structure.

It is highly unlikely that the numerical modelling approach to design and stability estimation of structural weaknesses will ever replace other conventional methods that have been and are still in use. However, as technology progresses it comes ever more fundamental part as supplement to other geological investigations. In fact, today's methods for numerical modelling is highly dependant on thorough investigations to estimate the conditions the model can be based on. The model will never be more accurate than the input data that is fed into it. One of the major obstacles in the geological investigation process is quantifying qualitative data like all of the rock mass quality systems attempt to overcome, but are still somewhat based on. Erroneous input data will never result in anything other than inaccurate output.

---

## References

- ADB. (2008, October). *Bhutan: Green Power Development Project*. Asian Development Bank.
- ADB. (2010, August). *Bhutan: Energy Sector*. Asian Development Bank.
- Barton, N., Lien, R., & Lunde, J. (1974). Engineering classification of rock masses for the design of tunnel support. *Rock Mechanics*, 6(4), 189–236.
- Beer, G. (2000). Modeling in geomechanics. In M. Zaman, G. Gioda, & J. Booker (Eds.), (chap. Boundary Element and Coupled Methods in Geomechanics). Chichester, England: John Wiley & sons Ltd.
- Beer, G., Smith, I. M., & Dunser, C. (2008). *The boundary element method with programming: For engineers and scientists*. Wien, Austria: Springer.
- Bieniawski, Z. T. (1976). Exploration for rock engineering, proc. of the symp. In Z. T. Bieniawski (Ed.), (chap. Rock mass classification in rock engineering). Cape Town, South Africa: Balkema.
- Bieniawski, Z. T. (1989). *Engineering rock mass classification*. New York, State of New York, USA: John Wiley & sons Ltd.
- Broch, E., & Palmstrom, A. (2006). Use and misuse of rock mass classification systems with particular reference to the Q-system. *Tunnels and Underground Space Technology*, 21, 575-593.
- Char, S. A., Menon, K. K., & Sood, P. K. (1988). Rock mechanics and power plants. In Romana (Ed.), (chap. Geotechnical aspects affecting the design and construction of underground structures for Chukha hydroelectric project). Rotterdam, Netherlands: Balkema.
- Chopra, V., & Gupta, A. (2003). Roof arch failure of machine hall cavern – Tala hydroelectric project, Bhutan. In *International conference on engineering of dams and appurtence works including powerhouse and transmission systems*. New Delhi, India.
- Chowdhry, A. K. (2007, June). Crown failure in the machine hall cavern of Tala hydroelectric project, Bhutan Himalaya. In *International workshop experiences gained in design and construction of Tala hydroelectric project* (p. 93-105). New Delhi, India.
- Chukha Hydel Project, Bhutan* (Geological report). (1984, January). New Delhi, India: Wapcos.
- Dorji, G. (2012). *Stability analysis of underground power house at Tala hydroelectric power project, Bhutan* (Unpublished master's thesis). NTNU.
- Gansser, A. (1983). *Geology of the Bhutan Himalaya*. Basel, Switzerland: Birkhäuser Verlag.
- Gnilsen, R. (1989). Underground structures: Design and instrumentation. In R. S. Sinha (Ed.), (chap. Numerical Methods). Amsterdam, Netherlands: Elsevier Science Publishers.

- 
- Goyal, D., & Khazanchi, R. (2003). Excavation problems in shafts of 1020 MW Tala hydroelectric project in Bhutan Himalayas. In *Water Power XIII*. Buffalo, USA.
- Grujic, D., Hollister, L. S., & Parrish, R. R. (2002). Himalayan metamorphic sequence as an orogenic channel: Insight from Bhutan. *Earth and Planetary Science Letters*, 198(1), 177–191.
- Hammah, R. E., & Curran, J. H. (2009). It is better to be approximately right than precisely wrong: Why simple models work in mining geomechanics. In *The 43rd US rock mechanics symposium and 4th U.S.-Canada rock mechanics symposium*. Asheville, North Carolina, USA.
- Harrison, J. P., & Hudson, J. A. (1997). *Engineering rock mechanics - An introduction to the principles*. Elsevier.
- Hoek, E., & Brown, E. T. (1980). Empirical strength criterion for rock masses. *Journal of Geotechnical and Geoenvironmental Engineering*, 106(ASCE 15715).
- Hoek, E., & Brown, E. T. (1997). Practical estimates of rock mass strength. *International Journal of Rock Mechanics and Mining Sciences*, 34(8), 1165–1186.
- Hoek, E., Carranza-Torres, C., & Corkum, B. (2002). Hoek-Brown failure criterion - 2002 edition. *Proceedings of NARMS-Tac*, 267–273.
- Hoek, E., Kaiser, P. K., & Bawden, W. F. (1995). *Support of underground excavations in hard rock*. Rotterdam, Netherlands: Balkema.
- Hoek, E., Marinos, P., & Benissi, M. (1998). Applicability of the geological strength index (GSI) classification for very weak and sheared rock masses. The case of the Athens Schist Formation. *Bull Eng Geol Environ*, 57, 151-160.
- ISRM. (1975). *Commission on terminology, symbols and graphic representation*. International Society for Rock Mechanics (ISRM).
- Jing, L., & Hudson, J. (2002). Numerical methods in rock mechanics. *International Journal of Rock Mechanics & Mining Sciences*, 39, 409-427.
- Labuz, J. F., & Zang, A. (2012). Mohr–Coulomb failure criterion. *Rock mechanics and rock engineering*, 1–5.
- Madhavan, K., Parasuraman, M. P., & Sood, P. K. (1987). Rock failure near face IV of Chukha power tunnel. In *6th ISRM Congress, 30 August-3 September, Montreal, Canada*.
- Maps of World*. (2013). Retrieved from [www.mapsofworld.com](http://www.mapsofworld.com)
- Marinos, V., Marinos, P., & Hoek, E. (2005). The geological strength index: applications and limitations. *Bull Eng Geol Environ*, 64, 55-65.
- McQuarrie, N., Robinson, D., Long, S., Tobgay, T., Grujic, D., Gehrels, G., & Ducea, M. (2008). Preliminary stratigraphic and structural architecture of Bhutan: Implications for the along strike architecture of the Himalayan system. *Earth and Planetary Science Letters*, 272(1), 105–117.
- Myrvang, A. (2001). *Bergmekanikk (in Norwegian)*. Trondheim, Norway: Institutt for Geology og Bergteknikk, NTNU.



- 
- Naik, S. R., Nair, R., Sudhakar, K., & Nawani, P. C. (2011, June). *Back analysis using numerical modelling of powerhouse complex of Tala hydroelectric project, Bhutan* (Final report No. NM1003C/01). NIRM.
- Naik, S. R., Sudhakar, K., Nair, R., & Nawani, P. C. (2011, June). *Instrumentation, monitoring and data analysis at powerhouse complex, Tala hydropower plant, Bhutan* (Final report No. NM1001C/02). NIRM.
- Palmström, A., & Singh, R. (2001). The deformation modulus of rock masses - Comparisons between in situ tests and indirect estimates. *Tunnelling and Underground Space Technology*, 16(2), 115–131.
- Panthi, K. K., & Nilsen, B. (2007). Predicted versus actual rock mass conditions: A review of four tunnel projects in Nepal Himalaya. *Tunnelling and Underground Space Technology*, 22, 173–184.
- Report on quality control measures adopted for construction of powerhouse complex at 1020 MW Tala hydroelectric project in Bhutan* (Tech. Rep.). (2006, December). NA.
- Singh, R., Chowdhry, A. K., Sharma, B. N., Goyal, D. P., & Khazanchi, R. N. (2002). Wall support system for powerhouse cavern of Tala hydroelectric project in Bhutan Himalayas. In *INDOROCK – Indian Rock Conference, ISRMIT at CSMRSM*. New Delhi, India.
- Tobgay, T., Long, S., McQuarrie, N., Ducea, M., & Gehrels, G. (2010). Using isotopic and chronologic data to fingerprint strata: Challenges and benefits of variable sources to tectonic interpretations, the Paro Formation, Bhutan Himalaya. *Tectonics*, 29(6).
- Tripathi, S., & Yadava, V. (2007, June). Some fundamental geotechnical aspects related to the behavior of large caverns, Tala hydroelectric project, Bhutan. In *International workshop experiences gained in design and construction of Tala hydroelectric project* (p. 86-92). New Delhi, India.

---

---

# Appendices

## Appendix A: Rock Mass Qualities

**Table A1:** Guidelines for assigning values for the Q parameters. From Hoek et al., 1995, after Barton et al., 1974

DESCRIPTION	VALUE	NOTES
<b>1. ROCK QUALITY DESIGNATION</b>	<b>RQD</b>	
A. Very poor	0 - 25	1. Where RQD is reported or measured as $\leq 10$ (including 0), a nominal value of 10 is used to evaluate Q.
B. Poor	25 - 50	
C. Fair	50 - 75	2. RQD intervals of 5, i.e. 100, 95, 90 etc. are sufficiently accurate.
D. Good	75 - 90	
E. Excellent	90 - 100	
<b>2. JOINT SET NUMBER</b>	<b><math>J_n</math></b>	
A. Massive, no or few joints	0.5 - 1.0	
B. One joint set	2	
C. One joint set plus random	3	
D. Two joint sets	4	
E. Two joint sets plus random	6	1. For intersections use $(3.0 \times J_n)$
F. Three joint sets	9	
G. Three joint sets plus random	12	2. For portals use $(2.0 \times J_n)$
H. Four or more joint sets, random, heavily jointed, 'sugar cube', etc.	15	
J. Crushed rock, earthlike	20	
<b>3. JOINT ROUGHNESS NUMBER</b>	<b><math>J_r</math></b>	
<b>a. Rock wall contact</b>		
<b>b. Rock wall contact before 10 cm shear</b>		
A. Discontinuous joints	4	
B. Rough and irregular, undulating	3	
C. Smooth undulating	2	1. Add 1.0 if the mean spacing of the relevant joint set is greater than 3 m.
D. Slickensided undulating	1.5	
E. Rough or irregular, planar	1.5	2. $J_r = 0.5$ can be used for planar, slickensided joints having lineations, provided that the lineations are oriented for minimum strength.
F. Smooth, planar	1.0	
G. Slickensided, planar	0.5	
<b>c. No rock wall contact when sheared</b>		
H. Zones containing clay minerals thick enough to prevent rock wall contact	1.0 (nominal)	
J. Sandy, gravely or crushed zone thick enough to prevent rock wall contact	1.0 (nominal)	
<b>4. JOINT ALTERATION NUMBER</b>	<b><math>J_a</math></b>	$\phi_r$ degrees (approx.)
<b>a. Rock wall contact</b>		
A. Tightly healed, hard, non-softening, impermeable filling	0.75	1. Values of $\phi_r$ , the residual friction angle, are intended as an approximate guide to the mineralogical properties of the alteration products, if present.
B. Unaltered joint walls, surface staining only	1.0	
C. Slightly altered joint walls, non-softening mineral coatings, sandy particles, clay-free disintegrated rock, etc.	2.0	25 - 30
D. Silty-, or sandy-clay coatings, small clay-fraction (non-softening)	3.0	20 - 25
E. Softening or low-friction clay mineral coatings, i.e. kaolinite, mica. Also chlorite, talc, gypsum and graphite etc., and small quantities of swelling clays. (Discontinuous coatings, 1 - 2 mm or less in thickness)	4.0	8 - 16

**Table A2:** Guidelines for assigning values for the Q parameters(continued). From Hoek et al., 1995, after Barton et al., 1974

DESCRIPTION	VALUE	NOTES
<b>4. JOINT ALTERATION NUMBER</b>	$J_a$	$\phi$ r degrees (approx.)
<b>b. Rock wall contact before 10 cm shear</b>		
F. Sandy particles, clay-free, disintegrating rock etc.	4.0	25 - 30
G. Strongly over-consolidated, non-softening clay mineral fillings (continuous < 5 mm thick)	6.0	16 - 24
H. Medium or low over-consolidation, softening clay mineral fillings (continuous < 5 mm thick)	8.0	12 - 16
J. Swelling clay fillings, i.e. montmorillonite, (continuous < 5 mm thick). Values of $J_a$ depend on percent of swelling clay-size particles, and access to water.	8.0 - 12.0	6 - 12
<b>c. No rock wall contact when sheared</b>		
K. Zones or bands of disintegrated or crushed rock and clay (see G, H and J for clay conditions)	6.0	
L. Zones or bands of silty- or sandy-clay, small clay fraction, non-softening	8.0	
M. Thick continuous zones or bands of clay	8.0 - 12.0	6 - 24
N. & R. (see G.H and J for clay conditions)	5.0	
O. Thick continuous zones or bands of clay	10.0 - 13.0	
P. & R. (see G.H and J for clay conditions)	6.0 - 24.0	
<b>5. JOINT WATER REDUCTION</b>	$J_w$	approx. water pressure (kgf/cm <sup>2</sup> )
A. Dry excavation or minor inflow i.e. < 5 l/m locally	1.0	< 1.0
B. Medium inflow or pressure, occasional outwash of joint fillings	0.66	1.0 - 2.5
C. Large inflow or high pressure in competent rock with unfilled joints	0.5	2.5 - 10.0
D. Large inflow or high pressure	0.33	2.5 - 10.0
E. Exceptionally high inflow or pressure at blasting, decaying with time	0.2 - 0.1	> 10
F. Exceptionally high inflow or pressure	0.1 - 0.05	> 10
<b>6. STRESS REDUCTION FACTOR</b>		<b>SRF</b>
<b>a. Weakness zones intersecting excavation, which may cause loosening of rock mass when tunnel is excavated</b>		
A. Multiple occurrences of weakness zones containing clay or chemically disintegrated rock, very loose surrounding rock any depth)	10.0	1. Reduce these values on the relevant shear zones only influence but f SRF by 25 - 50% if do not intersect the excavation
B. Single weakness zones containing clay, or chemically disintegrated rock (excavation depth < 50 m)	5.0	
C. Single weakness zones containing clay, or chemically disintegrated rock (excavation depth > 50 m)	2.5	
D. Multiple shear zones in competent rock (clay free), loose surrounding rock (any depth)	7.5	
E. Single shear zone in competent rock (clay free). (depth of excavation < 50 m)	5.0	
F. Single shear zone in competent rock (clay free). (depth of excavation > 50 m)	2.5	
G. Loose open joints, heavily jointed or 'sugar cube', (any depth)	5.0	

**Table A3:** Guidelines for assigning values for the Q parameters(continued). From Hoek et al., 1995, after Barton et al., 1974

DESCRIPTION	VALUE	NOTES
<b>6. STRESS REDUCTION FACTOR</b>		
<b>SRF</b>		
<b>b. Competent rock, rock stress problems</b>		
	$\sigma_c/\sigma_1$	$\sigma_t/\sigma_1$
H. Low stress, near surface	> 200	> 13
J. Medium stress	200 - 10	13 - 0.66
K. High stress, very tight structure (usually favourable to stability, may be unfavourable to wall stability)	10 - 5	0.66 - 0.33
L. Mild rockburst (massive rock)	5 - 2.5	0.33 - 0.16
M. Heavy rockburst (massive rock)	< 2.5	< 0.16
<b>c. Squeezing rock, plastic flow of incompetent rock under influence of high rock pressure</b>		
N. Mild squeezing rock pressure		5 - 10
O. Heavy squeezing rock pressure		10 - 20
<b>d. Swelling rock, chemical swelling activity depending on presence of water</b>		
P. Mild swelling rock pressure		5 - 10
R. Heavy swelling rock pressure		10 - 15
<b>ADDITIONAL NOTES ON THE USE OF THESE TABLES</b>		
When making estimates of the rock mass Quality (Q), the following guidelines should be followed in addition to the notes listed in the tables:		
1. When borehole core is unavailable, RQD can be estimated from the number of joints per unit volume, in which the number of joints per metre for each joint set are added. A simple relationship can be used to convert this number to RQD for the case of clay free rock masses: $RQD = 115 - 3.3 J_v$ (approx.), where $J_v$ = total number of joints per $m^3$ ( $0 < RQD < 100$ for $35 > J_v > 4.5$ ).		
2. The parameter $J_n$ representing the number of joint sets will often be affected by foliation, schistosity, slaty cleavage or bedding etc. If strongly developed, these parallel 'joints' should obviously be counted as a complete joint set. However, if there are few 'joints' visible, or if only occasional breaks in the core are due to these features, then it will be more appropriate to count them as 'random' joints when evaluating $J_n$ .		
3. The parameters $J_r$ and $J_a$ (representing shear strength) should be relevant to the weakest significant joint set or clay filled discontinuity in the given zone. However, if the joint set or discontinuity with the minimum value of $J_r/J_a$ is favourably oriented for stability, then a second, less favourably oriented joint set or discontinuity may sometimes be more significant, and its higher value of $J_r/J_a$ should be used when evaluating Q. The value of $J_r/J_a$ should in fact relate to the surface most likely to allow failure to initiate.		
4. When a rock mass contains clay, the factor SRF appropriate to loosening loads should be evaluated. In such cases the strength of the intact rock is of little interest. However, when jointing is minimal and clay is completely absent, the strength of the intact rock may become the weakest link, and the stability will then depend on the ratio rock-stress/rock-strength. A strongly anisotropic stress field is unfavourable for stability and is roughly accounted for as in note 2 in the table for stress reduction factor evaluation.		
5. The compressive and tensile strengths ( $\sigma_c$ and $\sigma_t$ ) of the intact rock should be evaluated in the saturated condition if this is appropriate to the present and future in situ conditions. A very conservative estimate of the strength should be made for those rocks that deteriorate when exposed to moist or saturated conditions.		

**Table A4:** Guidelines for assigning values for the RMR parameters. From Hoek et al., 1995, after Bieniawski, 1989

A. CLASSIFICATION –PARAMETERS AND THEIR RATINGS									
Parameter			Range of values						
1	Strength of intact rock material	Point-load strength index	>10 MPa	4 - 10 MPa	2 - 4 MPa	1 - 2 MPa	For this low range - uniaxial compressive test is preferred		
		Uniaxial comp. strength	>250 MPa	100 - 250 MPa	50 - 100 MPa	25 - 50 MPa	5 - 25 MPa	1 - 5 MPa	< 1 MPa
	Rating	15	12	7	4	2	1	0	
2	Drill core Quality RQD		90% - --100%	75% --90%	50% - 75%	25% - 50%	< 25%		
	Rating		20	17	13	8	3		
3	Spacing of discontinuities		> 2 m	0.6 - 2 . m	200 - 600 mm	60 - 200 mm	< 60 mm		
	Rating		20	15	10	8	5		
4	Condition of –discontinuities (See E)		Very rough –surfaces Not continuous No separation Unweathered wall rock	Slightly rough surfaces Separation < 1 mm Slightly weathered walls	Slightly rough surfaces Separation < 1 mm Highly weathered walls	Slickensided surfaces or Gouge < 5 mm thick or Separation 1-5 mm Continuous	Soft gouge >5 mm thick or Separation → 5 mm Continuous		
	Rating		30	25	20	10	0		
-5	Ground water	Inflow per 10 m tunnel length (l/m)	None	< 10	10 - 25	25 - 125	> 125		
		(Joint water press)/ (Major principal $\sigma$ )	0	< 0.1	0.1, - 0.2	0.2 - 0.5	> 0.5		
		General conditions	Completely dry	Damp	Wet	Dripping	Flowing		
	Rating		15	10	7	4	0		
B. RATING ADJUSTMENT FOR DISCONTINUITY ORIENTATIONS (See F)									
Strike –and dip orientations		Very favourable	Favourable	Fair	Unfavourable	Very Unfavourable			
Ratings	Tunnels & mines	0	-2	-5	-10	-12			
	Foundations	0	-2	-7	-15	-25			
	Slopes	0	-5	-25	-50				
C. ROCK MASS CLASSES DETERMINED FROM TOTAL RATINGS									
Rating	100 ← 81		80 ← 61	60 ← 41	40 ← 21	< 21			
Class number	I		II	III	IV	V			
Description	Very good rock		Good rock	Fair rock	Poor rock	Very poor rock			
D. MEANING OF ROCK CLASSES									
Class number	I		II	III	IV	V			
Average stand-up time	20 yrs for 15 m span		1 year for 10 m span	1 week for 5 m span	10 hrs for 2.5 m span	30 min for 1 m span			
Cohesion of rock mass (kPa)	> 400		300 - 400	200 - 300	100 - 200	< 100			
Friction angle of rock mass (deg)	> 45		35 - 45	25 - 35	15 - 25	< 15			
E. GUIDELINES FOR CLASSIFICATION OF DISCONTINUITY conditions									
Discontinuity length (persistence)	< 1 m		1 - 3 m	3 - 10 m	10 - 20 m	> 20 m			
Rating	6		4	2	1	0			
Separation (aperture)	None		< 0,1 mm	0.1 - 1.0 mm	1 - 5 mm	> 5 mm			
Rating	6		5	4	1	0			
Roughness	Very rough		Rough	Slightly rough	Smooth	Slickensided			
Rating	6		5	3	1	0			
Infilling (gouge)	None		Hard filling < 5 mm	Hard filling > 5 mm	Soft filling < 5 mm	Soft filling > 5 mm			
Rating	6		4	2	2	0			
Weathering	Unweathered		Slightly weathered	Moderately weathered	Highly weathered	Decomposed			
Ratings	6		5	3	1	0			
F. EFFECT OF DISCONTINUITY STRIKE AND DIP ORIENTATION IN TUNNELLING**									
Strike perpendicular to tunnel axis				Strike parallel to tunnel axis					
Drive with dip - Dip 45 - 90°			Drive with dip - Dip 20 - 45°		Dip 45 - 90°		Dip 20 - 45°		
Very favourable			Favourable		Very favourable		Fair		
Drive against –dip - Dip 45-90°			Drive against –dip - –Dip 20-45°		–Dip 0-20 - Irrespective of strike°				
Fair			Unfavourable		Fair				

\* Some conditions are mutually exclusive . –For example, if infilling is present, the roughness of the surface will be overshadowed by the influence of the gouge. –In such cases use A.4 directly.

\*\* Modified after Wickham et al (1972).






**Table A5:** Value of the  $m_i$  constant for various rock types (Hoek & Brown, 1997)

Rock type	Class	Group	Texture			
			Coarse	Medium	Fine	Very fine
SEDIMENTARY	Clastic		Conglomerate (22)	Sandstone 19 —— Greywacke —— (18)	Siltstone 9	Claystone 4
		Organic		—— Chalk —— 7 —— Coal —— (8-21)		
	Non-Clastic	Carbonate	Breccia (20)	Sparitic Limestone (10)	Micritic Limestone 8	
		Chemical		Gypstone 16	Anhydrite 13	
METAMORPHIC	Non Foliated		Marble 9	Hornfels (19)	Quartzite 24	
	Slightly foliated		Migmatite (30)	Amphibolite 25 - 31	Mylonites (6)	
	Foliated*		Gneiss 33	Schists 4 - 8	Phyllites (10)	Slate 9
IGNEOUS	Light		Granite 33		Rhyolite (16)	Obsidian (19)
			Granodiorite (30)		Dacite (17)	
	Dark		Diorite (28)		Andesite 19	
		Gabbro 27 Norite 22	Dolerite (19)	Basalt (17)		
	Extrusive pyroclastic type		Agglomerate (20)	Breccia (18)	Tuff (15)	

\* These values are for intact rock specimens tested normal to bedding or foliation. The value of  $m_i$  will be significantly different if failure occurs along a weakness plane.



**Table A6:** Guidelines for estimation of D factor(Hoek et al., 2002)

Appearance of rock mass	Description of rock mass	Suggested value of <i>D</i>
	Excellent quality controlled blasting or excavation by Tunnel Boring Machine results in minimal disturbance to the confined rock mass surrounding a tunnel.	$D = 0$
	Mechanical or hand excavation in poor quality rock masses (no blasting) results in minimal disturbance to the surrounding rock mass.  Where squeezing problems result in significant floor heave, disturbance can be severe unless a temporary invert, as shown in the photograph, is placed.	$D = 0$  $D = 0.5$ No invert
	Very poor quality blasting in a hard rock tunnel results in severe local damage, extending 2 or 3 m, in the surrounding rock mass.	$D = 0.8$
	Small scale blasting in civil engineering slopes results in modest rock mass damage, particularly if controlled blasting is used as shown on the left hand side of the photograph. However, stress relief results in some disturbance.	$D = 0.7$ Good blasting  $D = 1.0$ Poor blasting
	Very large open pit mine slopes suffer significant disturbance due to heavy production blasting and also due to stress relief from overburden removal.  In some softer rocks excavation can be carried out by ripping and dozing and the degree of damage to the slopes is less.	$D = 1.0$ Production blasting  $D = 0.7$ Mechanical excavation

---

---

---

## Appendix B: Numerical Analyses

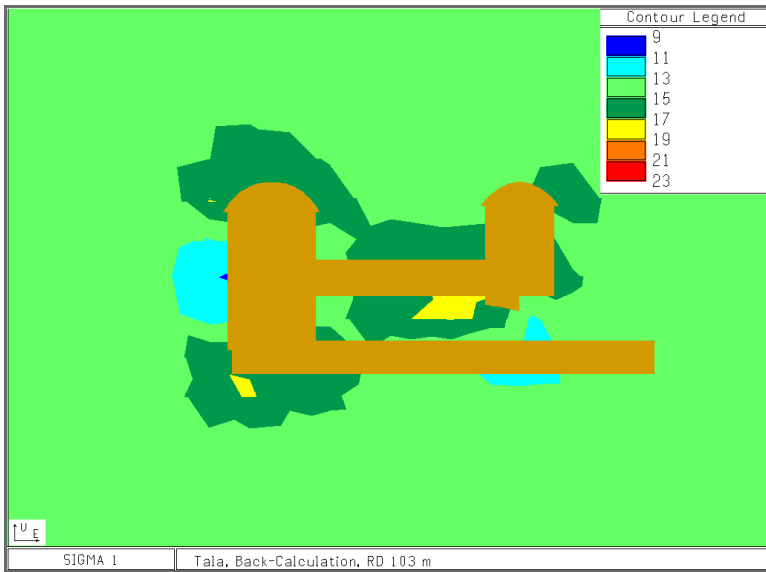


**Figure A1:** RD 103 m at Tala powerhouse complex, depicting contours of equal  $\sigma_1$ , using Young's modulus of 4250 MPa

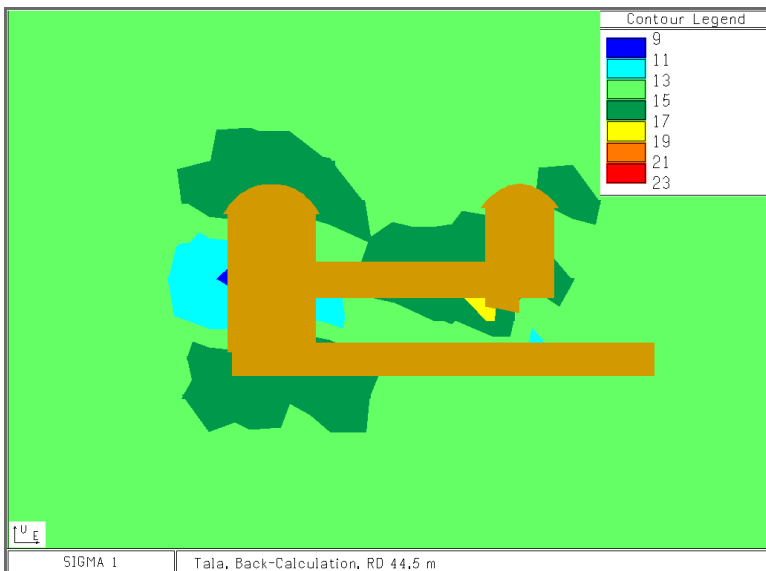


**Figure A2:** RD 44,5 m at Tala powerhouse complex, depicting contours of equal  $\sigma_1$ , using Young's modulus of 4250 MPa

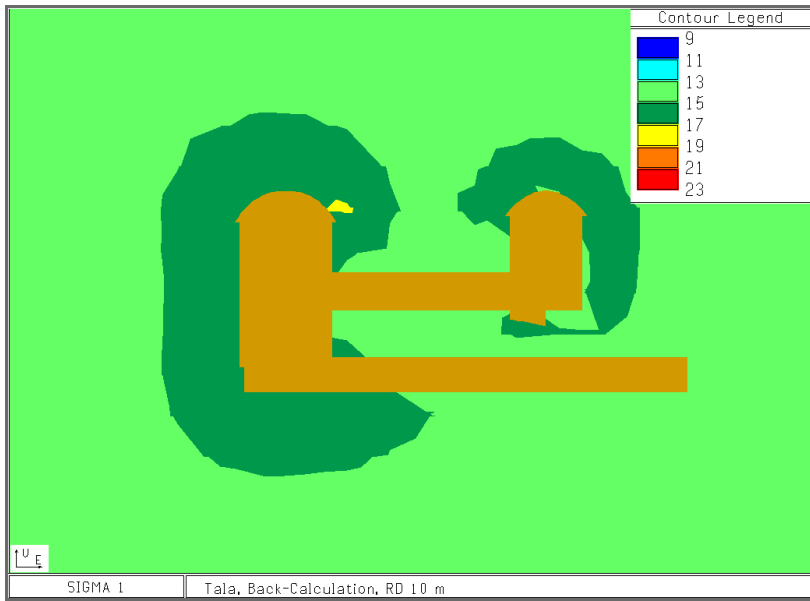


**Figure A3:** RD 10 m at Tala powerhouse complex, depicting contours of equal  $\sigma_1$ , using Young's modulus of 4250 MPa

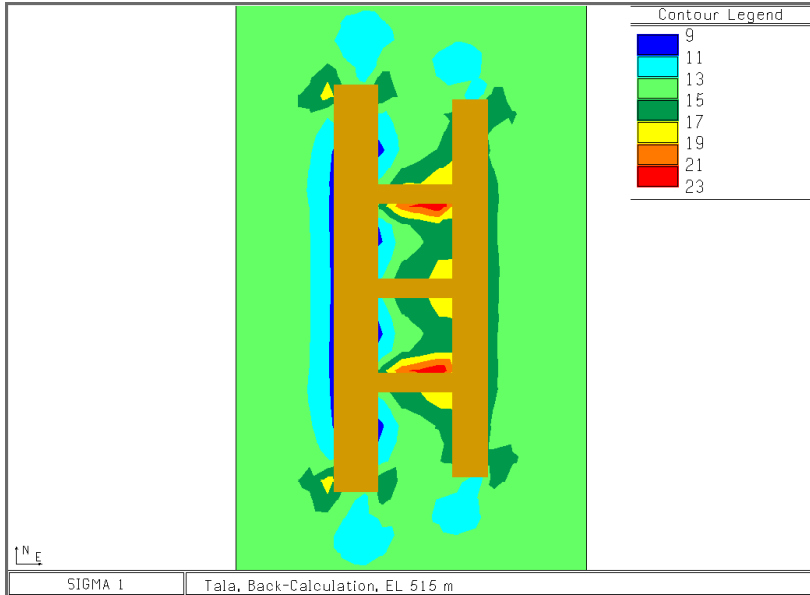


**Figure A4:** EL 515 m at Tala powerhouse complex, depicting contours of equal  $\sigma_1$ , using Young's modulus of 4250 MPa

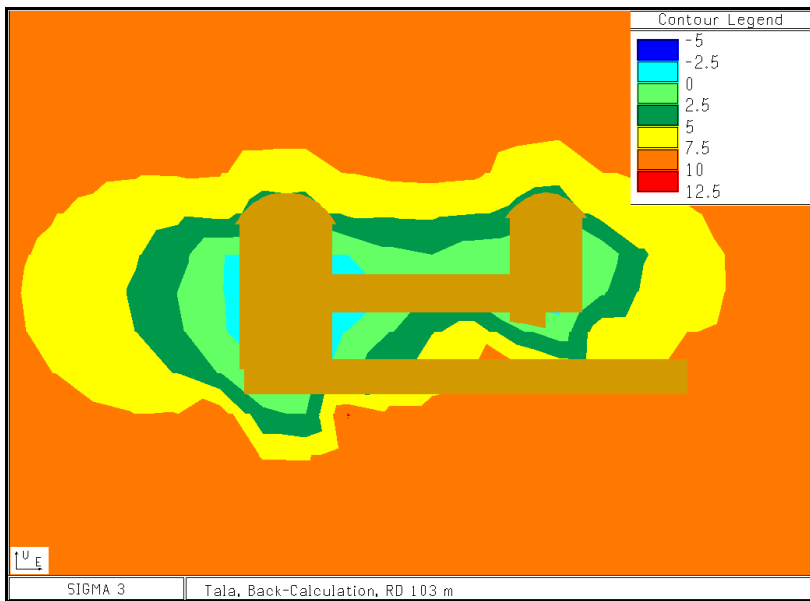


**Figure A5:** RD 103 m at Tala powerhouse complex, depicting contours of equal  $\sigma_3$ , using Young's modulus of 4250 MPa

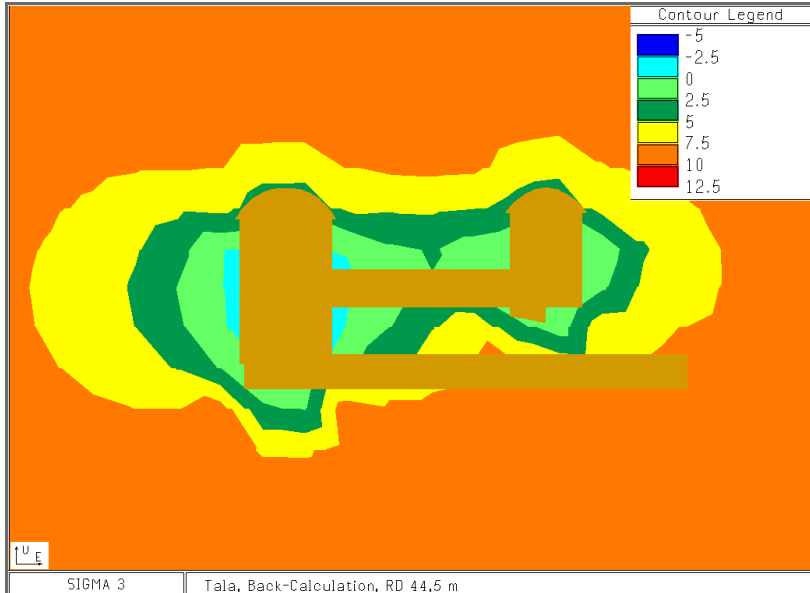


**Figure A6:** RD 44,5 m at Tala powerhouse complex, depicting contours of equal  $\sigma_3$ , using Young's modulus of 4250 MPa

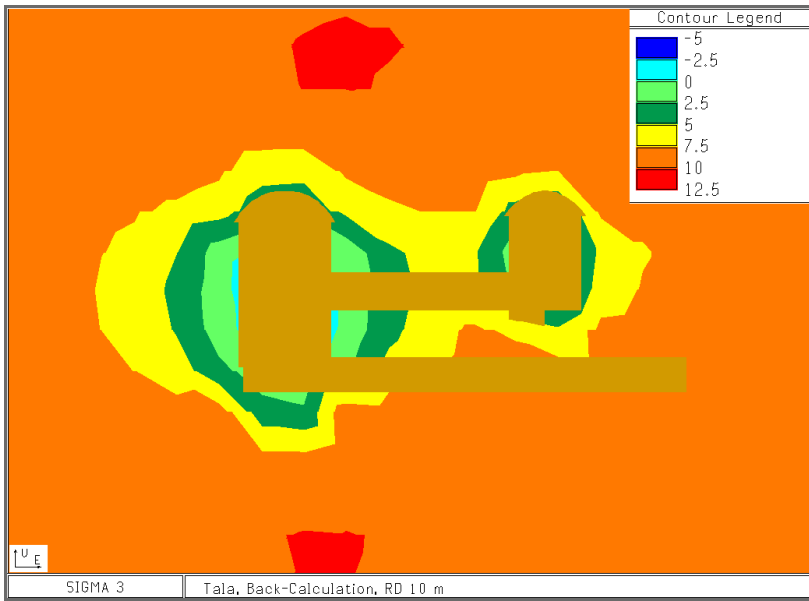


**Figure A7:** RD 10 m at Tala powerhouse complex, depicting contours of equal  $\sigma_3$ , using Young's modulus of 4250 MPa

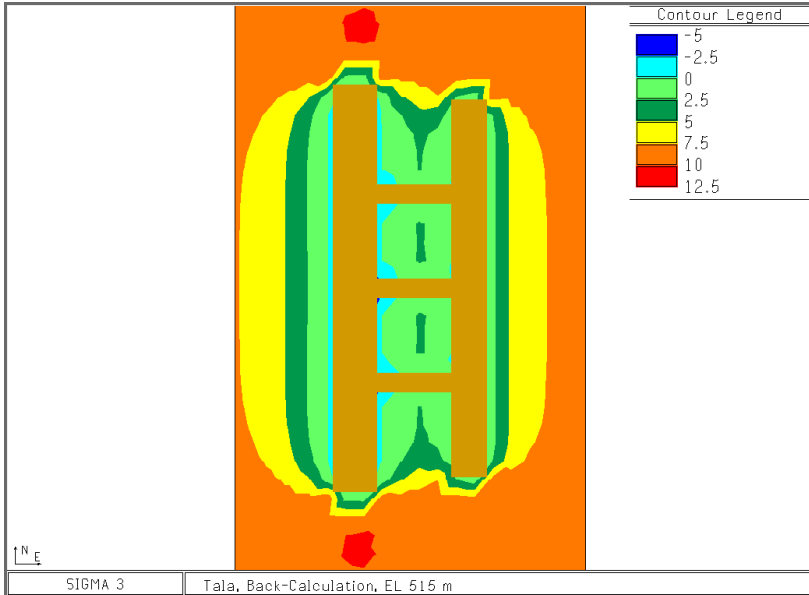


**Figure A8:** EL 515 m at Tala powerhouse complex, depicting contours of equal  $\sigma_3$ , using Young's modulus of 4250 MPa

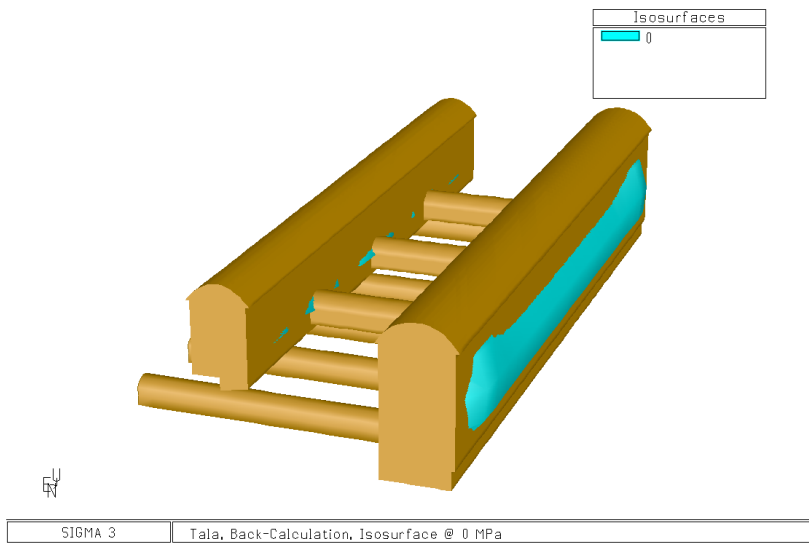


**Figure A9:** Perspective of the Tala powerhouse complex, depicting isosurface at  $\sigma_3 = 0$ , using Young's modulus of 4250 MPa

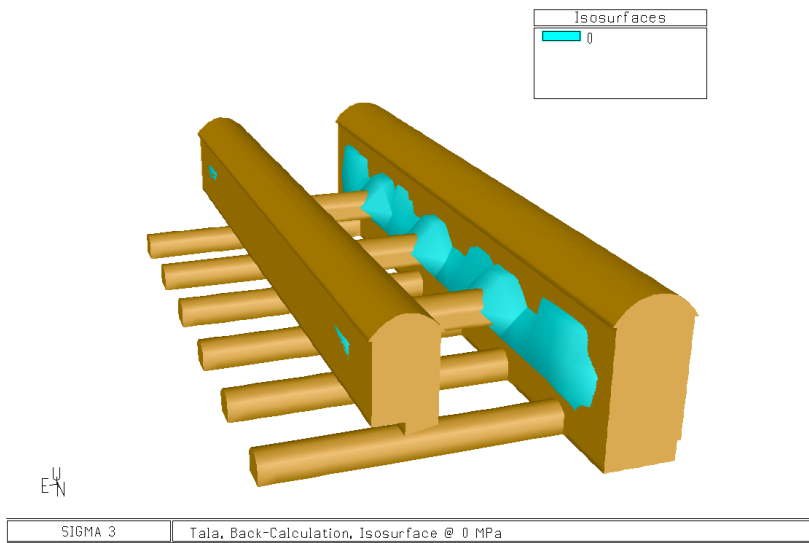


**Figure A10:** Perspective of the Tala powerhouse complex, depicting isosurface at  $\sigma_3 = 0$ , using Young's modulus of 4250 MPa

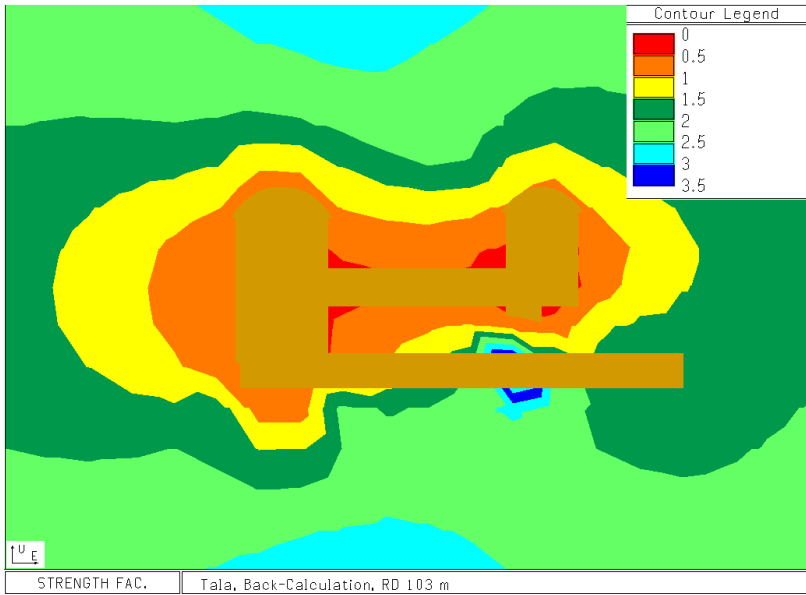


**Figure A11:** RD 103 m at Tala powerhouse complex, depicting contours of equal strength factor, using Young's modulus of 4250 MPa

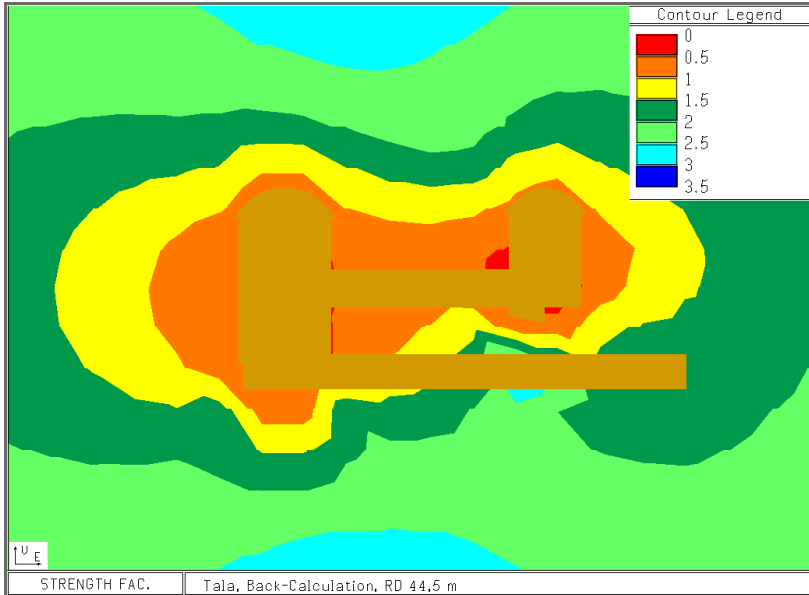


**Figure A12:** RD 44,5 m at Tala powerhouse complex, depicting contours of equal strength factor, using Young's modulus of 4250 MPa



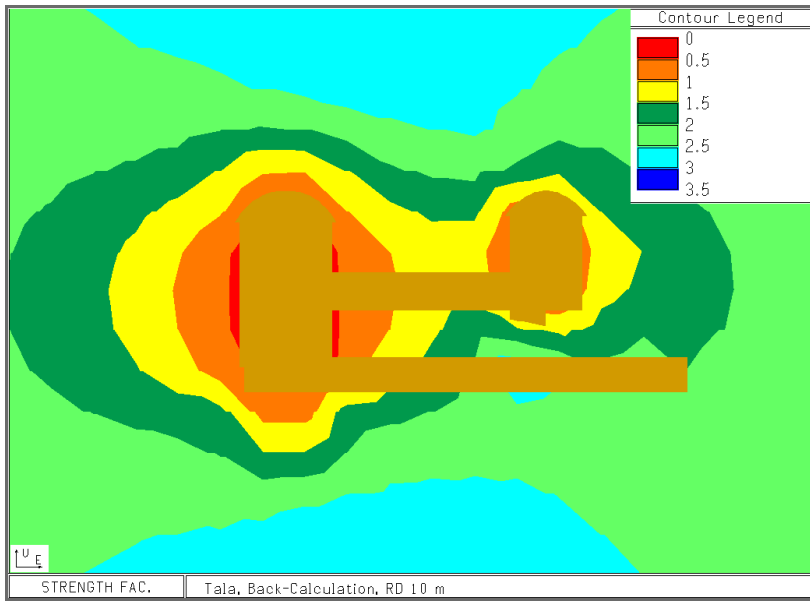


**Figure A13:** RD 10 m at Tala powerhouse complex, depicting contours of equal strength factor, using Young's modulus of 4250 MPa

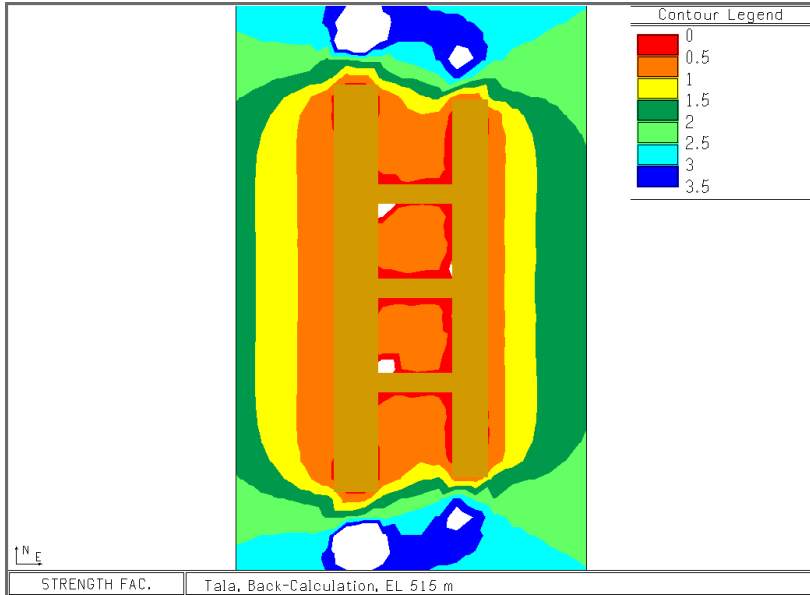


**Figure A14:** EL 515 m at Tala powerhouse complex, depicting contours of equal strength factor, using Young's modulus of 4250 MPa

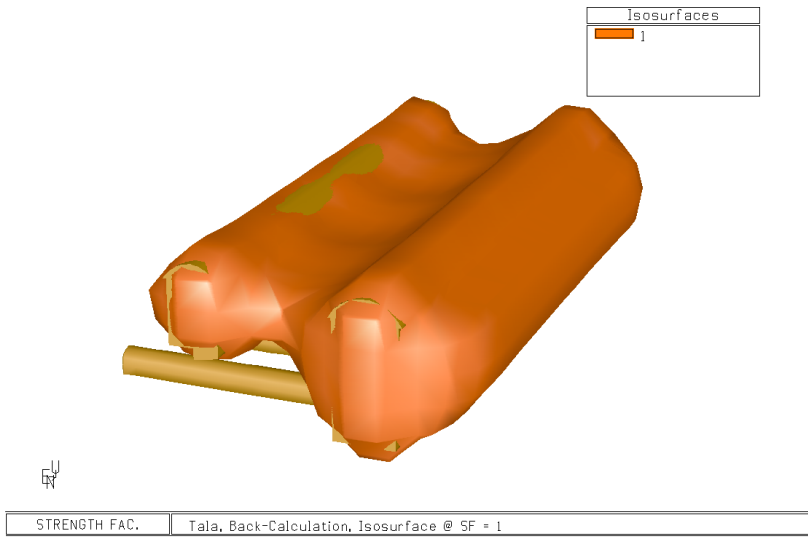


**Figure A15:** Perspective of the Tala powerhouse complex, depicting isosurface at strength factor = 1, using Young's modulus of 4250 MPa

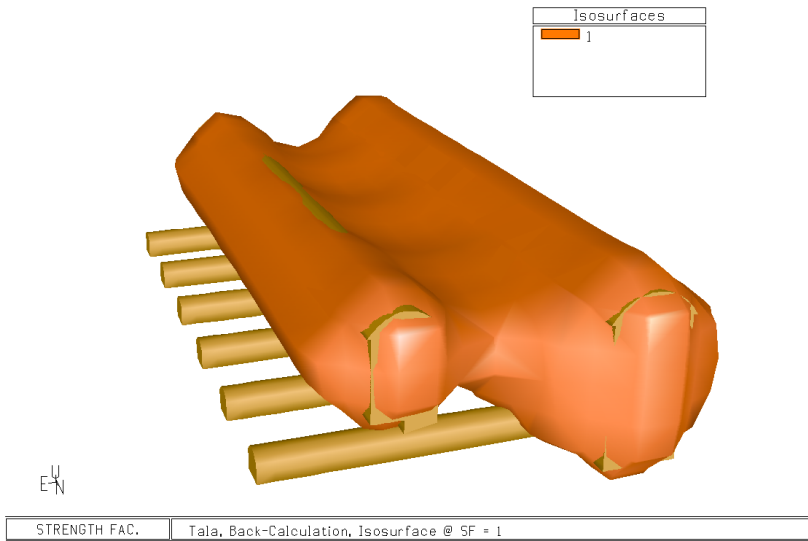


**Figure A16:** Perspective of the Tala powerhouse complex, depicting isosurface at strength factor = 1, using Young's modulus of 4250 MPa

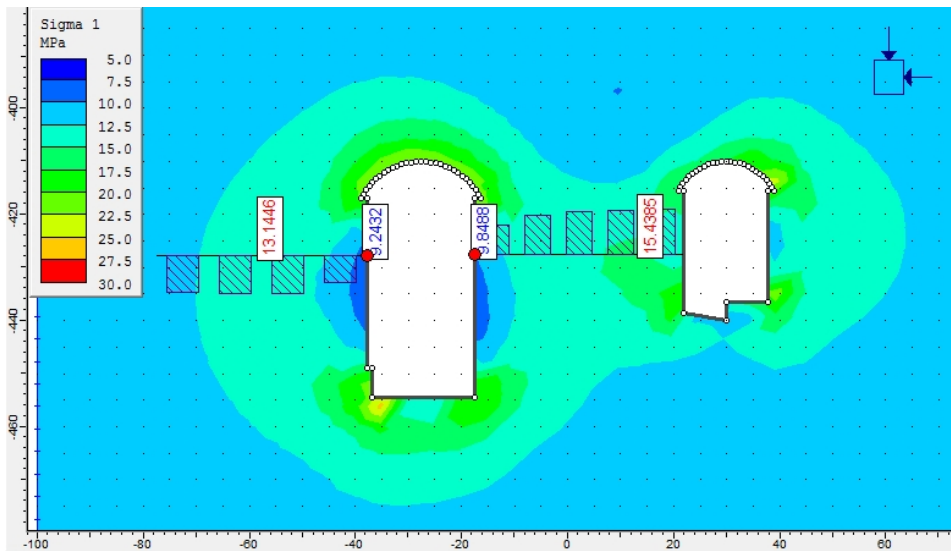


**Figure A17:** Examine<sup>2D</sup> model of the Tala powerhouse complex, depicting contours of equal  $\sigma_1$ , using Young's modulus of 4250 MPa

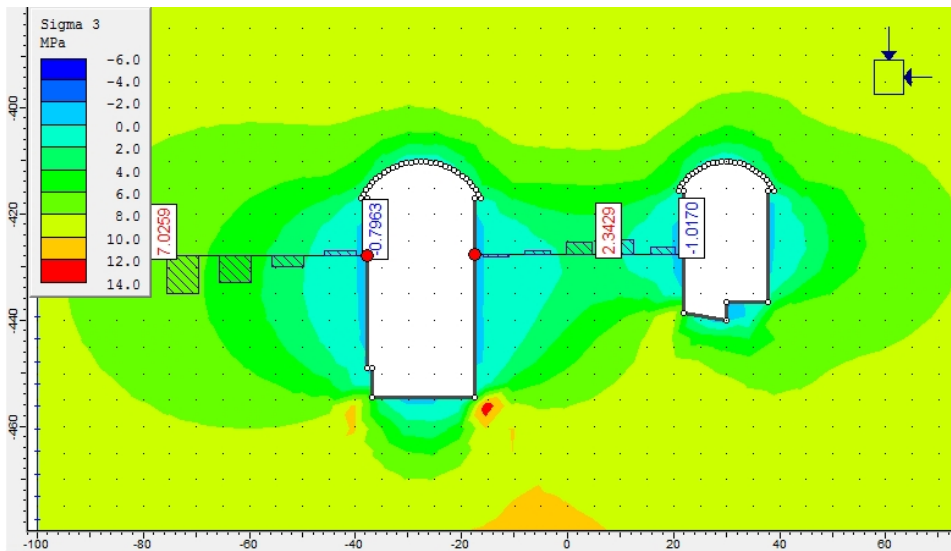


**Figure A18:** Examine<sup>2D</sup> model of the Tala powerhouse complex, depicting contours of equal  $\sigma_3$ , using Young's modulus of 4250 MPa

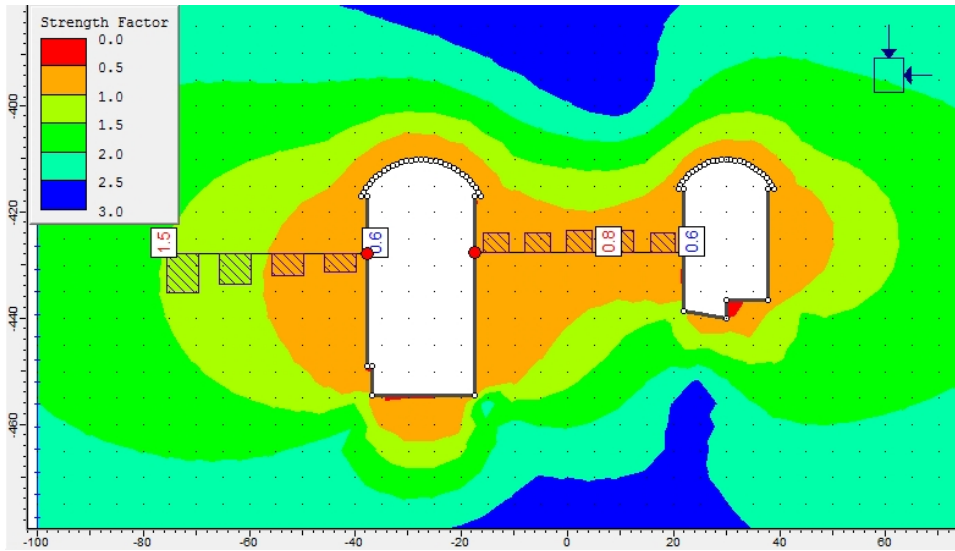


**Figure A19:** Examine<sup>2D</sup> model of the Tala powerhouse complex, depicting contours of equal strength factor, using Young's modulus of 4250 MPa

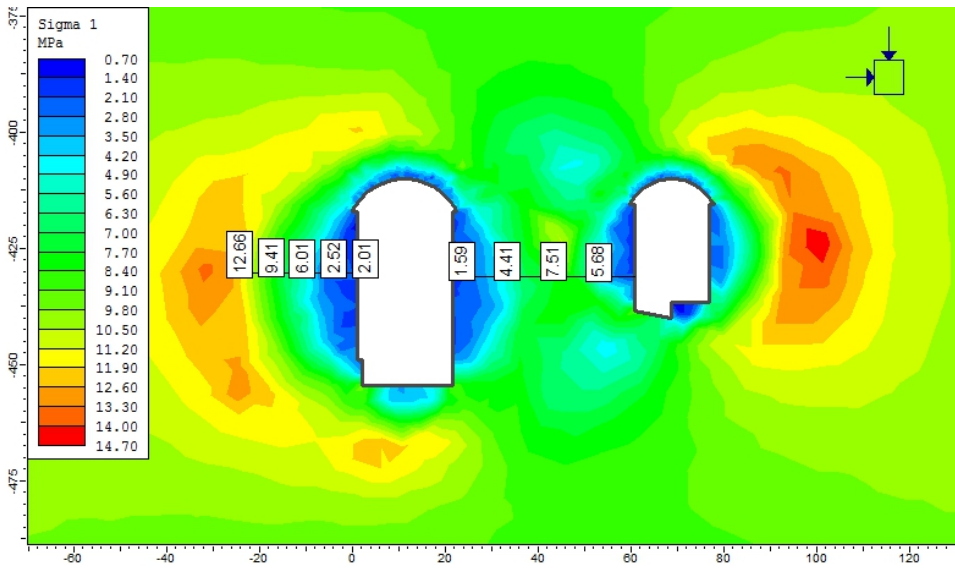


**Figure A20:** Phase<sup>2</sup> model of the Tala powerhouse complex, depicting contours of equal  $\sigma_1$ , using Young's modulus of 4250 MPa

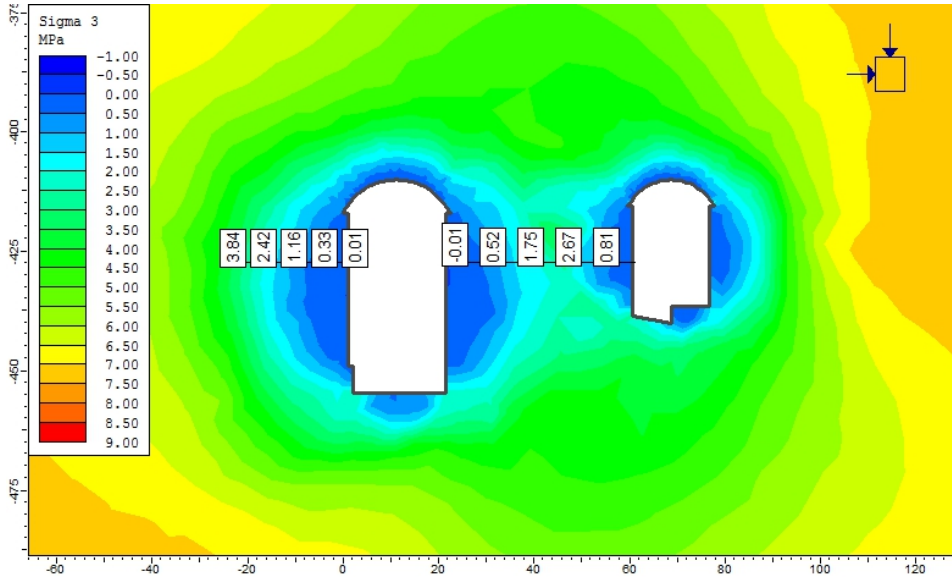


**Figure A21:** Phase<sup>2</sup> model of the Tala powerhouse complex, depicting contours of equal  $\sigma_3$ , using Young's modulus of 4250 MPa

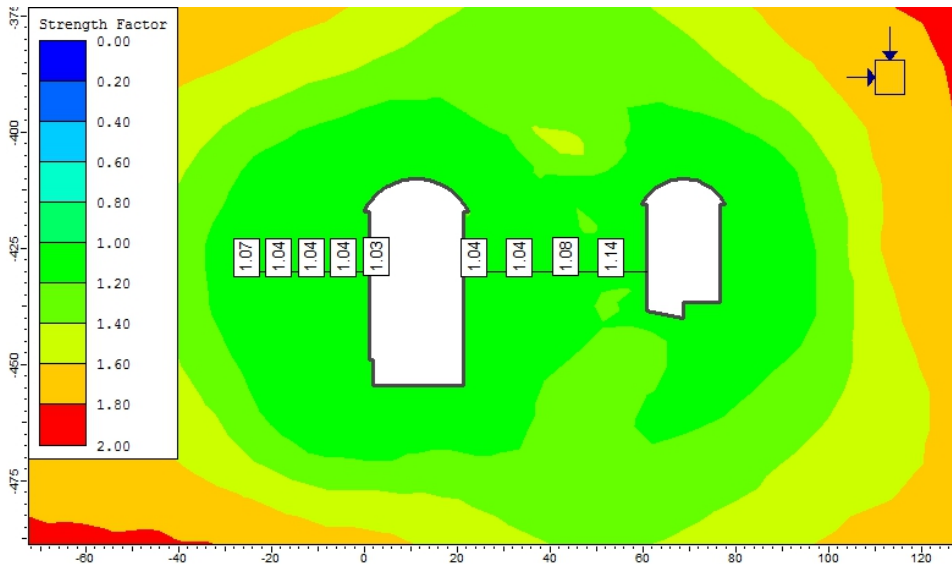


**Figure A22:** Phase<sup>2</sup> model of the Tala powerhouse complex, depicting contours of equal strength factor, using Young's modulus of 4250 MPa

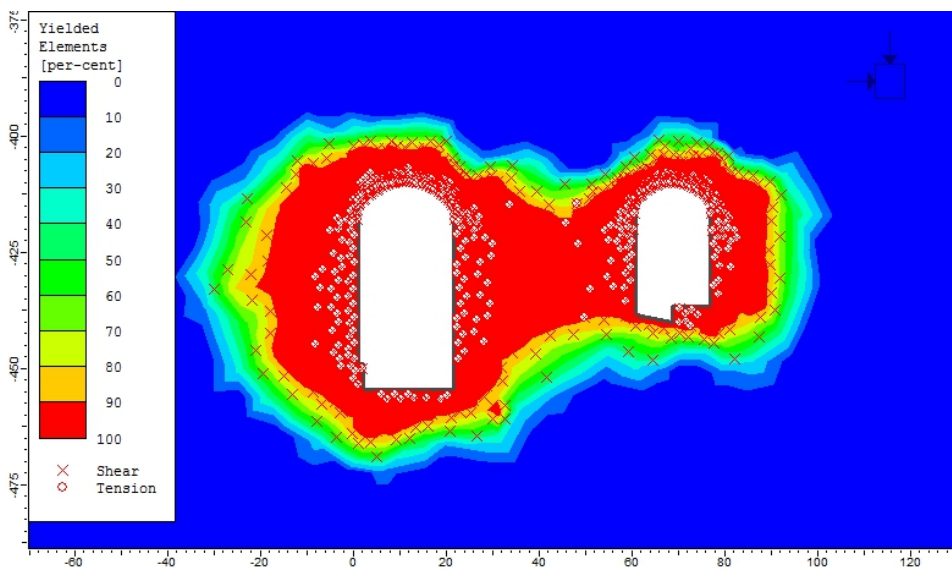


**Figure A23:** Phase<sup>2</sup> model of the Tala powerhouse complex, depicting yielded elements, using Young's modulus of 4250 MPa